

**2.1. Appendix C**

**Seismic Data Processing Report for USDOE-FOA-0000019 Grant**

**FINDING LARGE APERTURE FRACTURES IN GEOTHERMAL RESOURCE AREAS USING A THREE-COMPONENT LONG-OFFSET SURFACE SEISMIC SURVEY, SAN EMIDIO GEOTHERMAL RESOURCE, WASHOE COUNTY, NEVADA**

*Prepared for*

**U.S. Geothermal Inc.**

**1505 Tyrell Lane  
Boise, Idaho 83706**

*By*

**Optim, Inc.**

**200 South Virginia Street**

**Suite 560**

**Reno, NV 89501**

[www.optimsoftware.com](http://www.optimsoftware.com)

**February, 2011**

## Table of Contents

<b>1.0 Introduction</b> .....	<b>53</b>
<b>2.0 Data Acquisition Parameters</b> .....	<b>55</b>
<b>3.0 Technical Approach</b> .....	<b>57</b>
<b>4.0 Discussion of the Processed Seismic Data</b> .....	<b>60</b>
4.1 Line 1 (100) .....	60
4.2 Line 2 (200) .....	71
4.3 Line 3 (300) .....	81
4.4 Line 4 (400) .....	91
4.5 Line10 (101) .....	101
4.6 Line 5 (500) .....	108
4.7 Line 6 (600) .....	119
4.8 Line 7 (700) .....	130
4.9 Line 8 (800) .....	140
4.10 Line 9 (900) .....	150
<b>5.0 Preliminary Interpretations and Conclusions</b> .....	<b>161</b>
<b>6.0 References</b> .....	<b>163</b>

### 1 1.0 Introduction

20 miles of active source seismic data were acquired at the San Emidio Geothermal Project in Washoe County, Nevada, (Figure 1) as part of U.S. Geothermal Inc.'s DOE Recovery Act project. The objective of the survey was to test an innovative approach to locate large aperture fractures and faults that are distributed within the geothermal system. This is part of developing an exploration strategy that includes PSInSAR modeling and structural kinematic analysis to understand and locate these structures. The seismic data was analyzed using first arrival optimization to produce both P-wave and S-wave velocity models. In addition, the P-wave data was used to obtain depth migrated images of faults underlying each line. This will then be used to build a structural model for kinematic analysis.

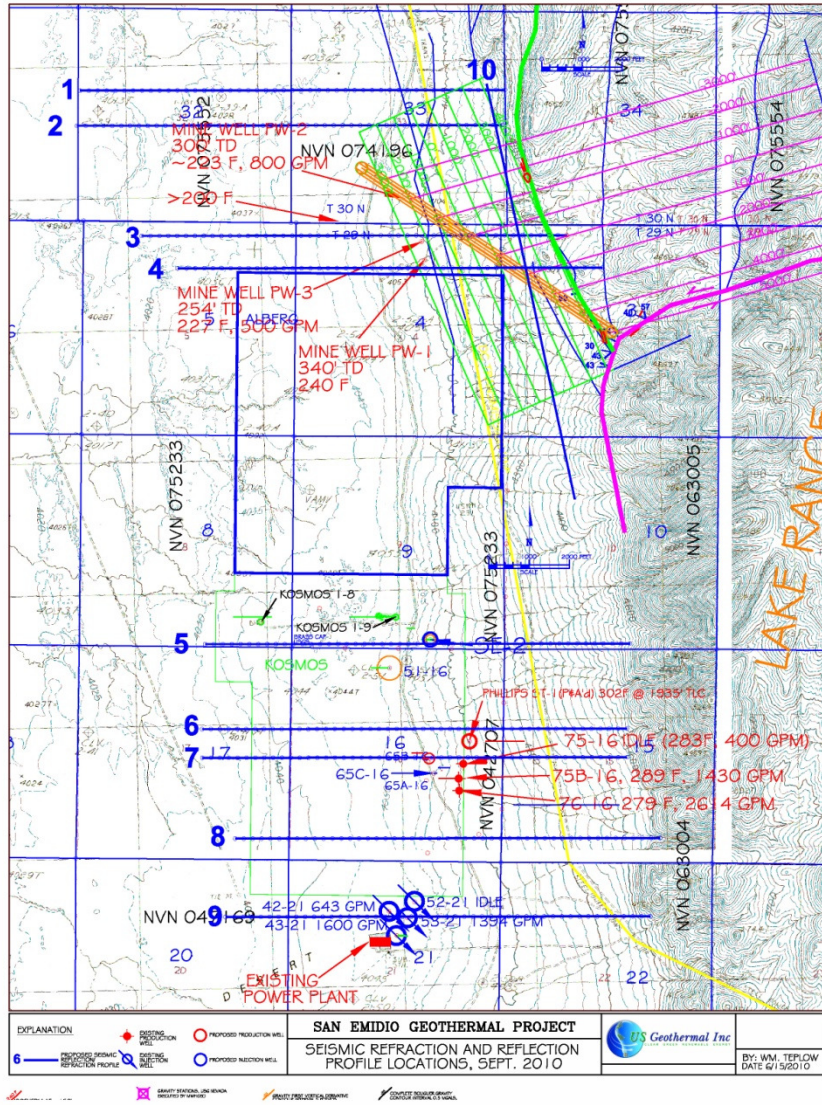


Figure 1. Map showing the orientation of the ten seismic lines acquired at San Emidio. The

The lines were located to maximize the subsurface area that can be mapped while at the same time address objectives of the study. The southern lines (5, 6, 7, 8 and 9) straddle boreholes that have intersected large aperture fracture zones and some that did not. It is hoped that the seismic signatures revealed by the 9-C survey will help explain this. Lines 1, 2, 3, 4 and 10 are in the northern portion of the geothermal field that is designated as exploration area. The knowledge gained from studying the results of the southern lines will be used to identifying potential drill targets in the northern area.

## 2 2.0 Data Acquisition Parameters

Each profile was approximately 10,000 ft long and had a geophone spacing of 55ft and shot (vibroseis) spacing of 220ft. Thus there were 49 shot points along each line. Data was recorded into each phone three times, one when the ground was shaken in the vertical direction, second in the horizontal inline direction and third along the horizontal crossline direction. So the maximum possible vibration points were 1470. Out of these 1447 points were recorded. 23 points were skipped due to archeological sites and site conditions which made it dangerous for the vibroseis trucks to get to the shaking locations. Three-component (3C) geophones (Figure 2) were used to record data at each geophone locations. Data was acquired for 6 seconds at 2 millisecond sample rate.

The survey called for three component sources. So two P-wave vibroseis trucks (Figure 3) operating in series were used to generate energy in the vertical direction (Figure 3) and two shear-wave vibroseis trucks operating in the inline direction (along the geophone array) and cross-line direction (perpendicular to the geophone) array were used to generate energy in the inline and crossline direction (Figure 4).



Figure 2: Three-component (3C) geophones were deployed at each geophone location at San Emidio.



Figure 3: P-wave vibroseis trucks imparted vertical energy into the ground that was recorded by the 3C geophones.



Figure 4: Shear-wave vibroseis trucks were used to shake the ground in the horizontal direction to produce shear wave energy. Shaking was done such that energy travelled along the array (inline) and also perpendicular to the array (cross line).

Prior to start of production, tests were done to ensure good data quality. For the P-wave vibroseis recording a sweep set that went from 8 to 100 Hz was used. 10 sweeps were stacked together at each location and data was recorded for 6 milliseconds. For the shear-wave recording a sweep range from 4 to 50 Hz was deemed appropriate with 4 sweeps at each location.

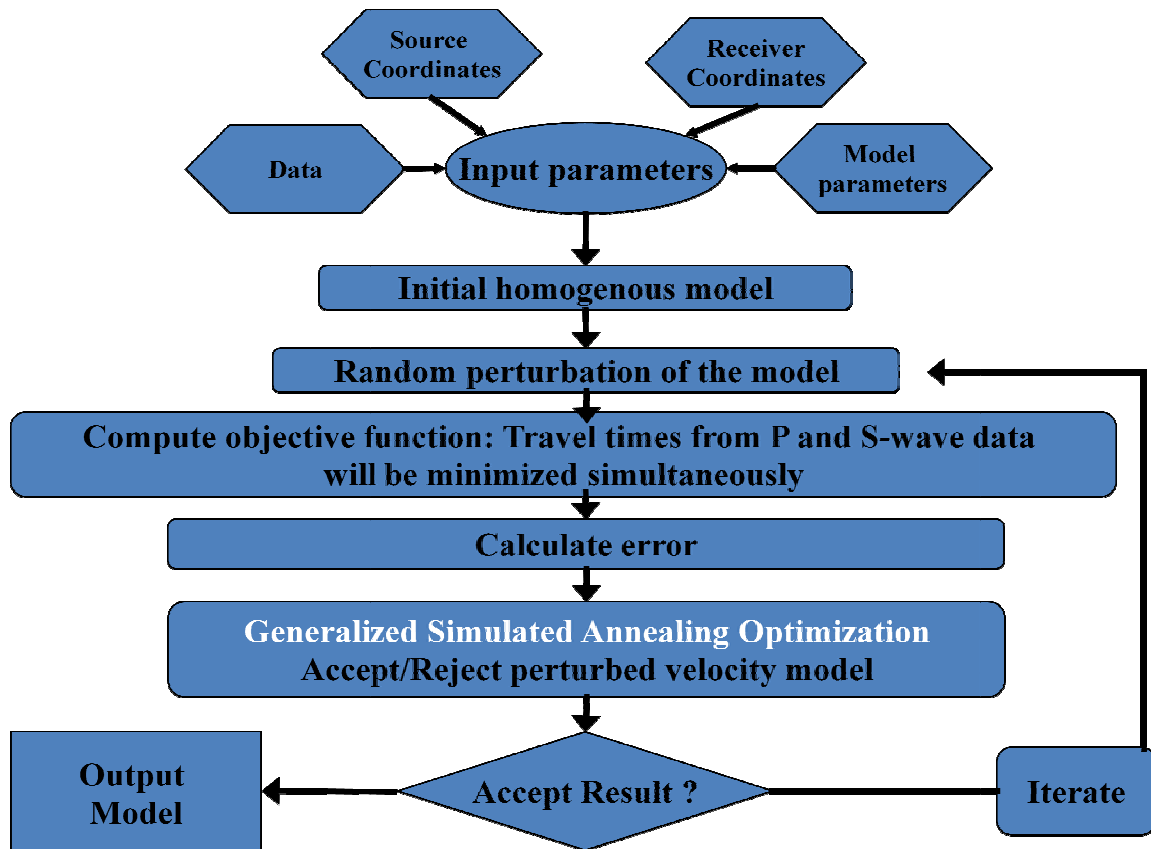
First arrival times picked off raw shot gathers were used to produce the velocity models using SeisOpt® 2D™ processing software. The velocity models derived from the first-arrival picks was then extended in depth and then used in a pre-stack migration algorithm to place the reflections at their correct depths. A dynamic signal to noise enhancement was also applied to the data to enhance reflectivity.

### 3 3.0 Technical Approach

Traditionally, surface seismic reflection has not been effective within geothermal anomalies because by nature either (a) there is a lack of acoustic impedance contrast or reflectivity, present to create strong, coherent reflectors or (b) the structure is so complex that it is impossible to place the reflectors in their proper subsurface position, thus revealing structure.

In our approach we derive velocities from first-arrivals picked off raw shot gathers (Pullammanappallil et al., 2001, Unruh et al., 2001). This is then extended in depth by performing iterative velocity optimization to maximize the reflection coherency. That is the model is adjusted so the reflectors at depth focus during a prestack depth migration.

First-arrival tomography obtaining both P- and S-wave velocities will be achieved using a simulated annealing optimization (Pullammanappallil and Louie, 1994). Simulated annealing is a Monte-Carlo estimation process that can match arrival times to a velocity model even where sophisticated non-linear inversion methods may fail (Pullammanappallil and Louie, 1997). The algorithm works by randomly perturbing an arbitrary starting model until the synthetic seismic wave travel times computed through it match the travel times picked from the new data. New models producing less travel time error are accepted for further enhancements, and models having increased error can be accepted conditionally based on their total error. As annealing proceeds, conditional acceptance becomes less and less likely. Unlike linear, iterative inversions, simulated annealing optimization will find the global velocity solution while avoiding local error minimums. It is also completely insensitive to the starting velocity model, removing the interpreter bias that may be involved in a prospect or project. This flexible nature of the optimization (Pullammanappallil and Louie, 1997) process allows it to be easily extended to obtain shear velocity images and perform simultaneous inversions for both P- and S-wave velocities. The flow chart illustrates the optimization schedule. The objective function will include both the S-wave and P-wave functions.



First arrival information from both P-wave and SH-wave data were used to derive P-wave and S-wave velocities under each line. This will allow tomographic estimation of compressional ( $V_p$ ) and shear ( $V_s$ ) wave velocities through the geothermal reservoir.

The resulting  $V_p/V_s$  sections is examined to determine if they reveal any characteristics that can help identify potential drill target zones. It is expected that there will be a decrease in  $V_p/V_s$  ratios within the fluid filled fracture zones (Bonner et al., 2006). The P-wave velocities will decrease with the opening of cracks and presence of fluids, while the S-waves being insensitive to presence of fluids may not show any decrease resulting in an overall decrease in the  $V_p/V_s$  ratios. The P-wave velocity model was then put through a Kirchhoff prestack depth migration to derive images of faults and fractures within the geothermal field. The pre-stack migration algorithm uses the velocity models for accurate calculation of travel times down to and up from every point within the reflection data volume. It produces images by summing the value of seismograms within the data volume at discrete points of time, based on travel-time calculations through the velocity model. Given a model that accurately characterizes the 2D-velocity structure a pre-stack depth migration can produce images from seismic data that has no visible signs of reflective coherency. Because pre-stack migration is free of assumptions about dip of bedding and structure, it will create images that reveal the true-depth location and geometry of permeable features in any orientation (Louie and Qin, 1991).

## 4 4.0 Discussion of the Processed Seismic Data

In this section we discuss the results of first-arrival picks optimization for  $V_p$  and  $V_s$  models. We then present and discuss the results of P-wave prestack depth migration (reflection image) for each profile.

While interpreting the reflection images, it is good practice to consider a series of package of reflections more reliable than a single reflection, unless the reflector in question is a relatively bright dipping feature. Also, like any surface geophysical method, resolution of the images decrease with depth. For our study the reliability of velocity model decreases below a depth of 5,000 feet and that of the reflection images below 7,000 – 8,000 feet. Lastly, the lack of reflectivity at the edges is a reflection of low fold (poor to no data coverage), rather than an effect of underlying structure. Faults and discontinuities are inferred both from the reflection image itself and also from the presence of lateral velocity change.

### 4.1 4.1 Line 1 (100)

Line 1, also called 100, is the northernmost line in the northern part of the project area and runs east-west from station number 101 in the west to 293 in the east (Figure 5a). It crosses line 10 (101) at station number 282. All of the figures represent true seismic depth sections with no vertical exaggeration.



Figure 5a: Line 1 (100) runs east-west from station number 101 in the west to station number 293 in the east.

Figures 5b and 5c show a typical shot gather acquired along Line 1 using P-wave and SH-wave source, respectively. The first arrivals (shown in red) are clearly visible. These were picked and used to obtain the velocity models shown in Figures 5d and 5e, respectively.

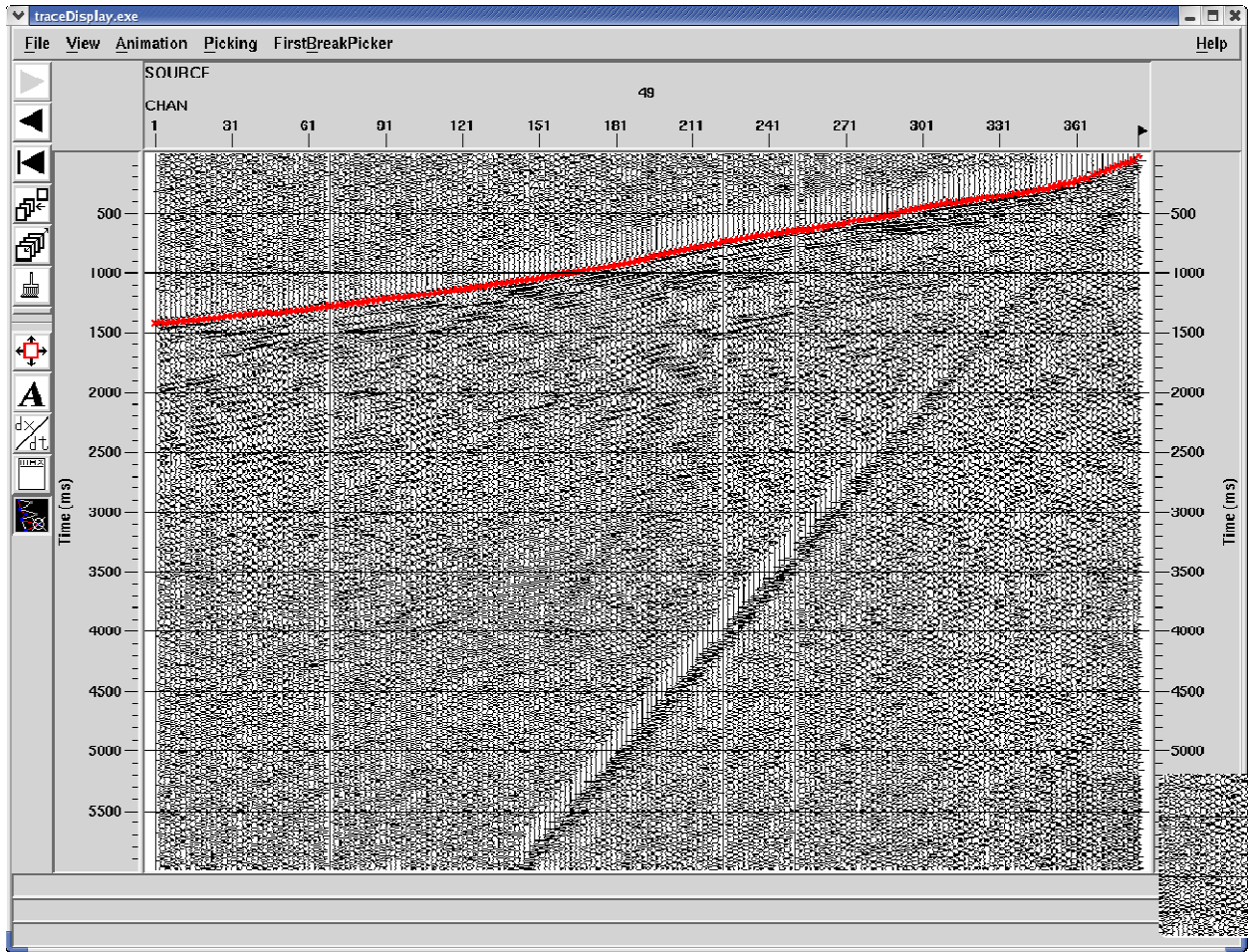


Figure 5b: Typical shot gathers from P-wave data collected along Line 1 (100). The first arrival picks, shown in red, was used to obtain the P-wave velocity model shown in Figure 5d.

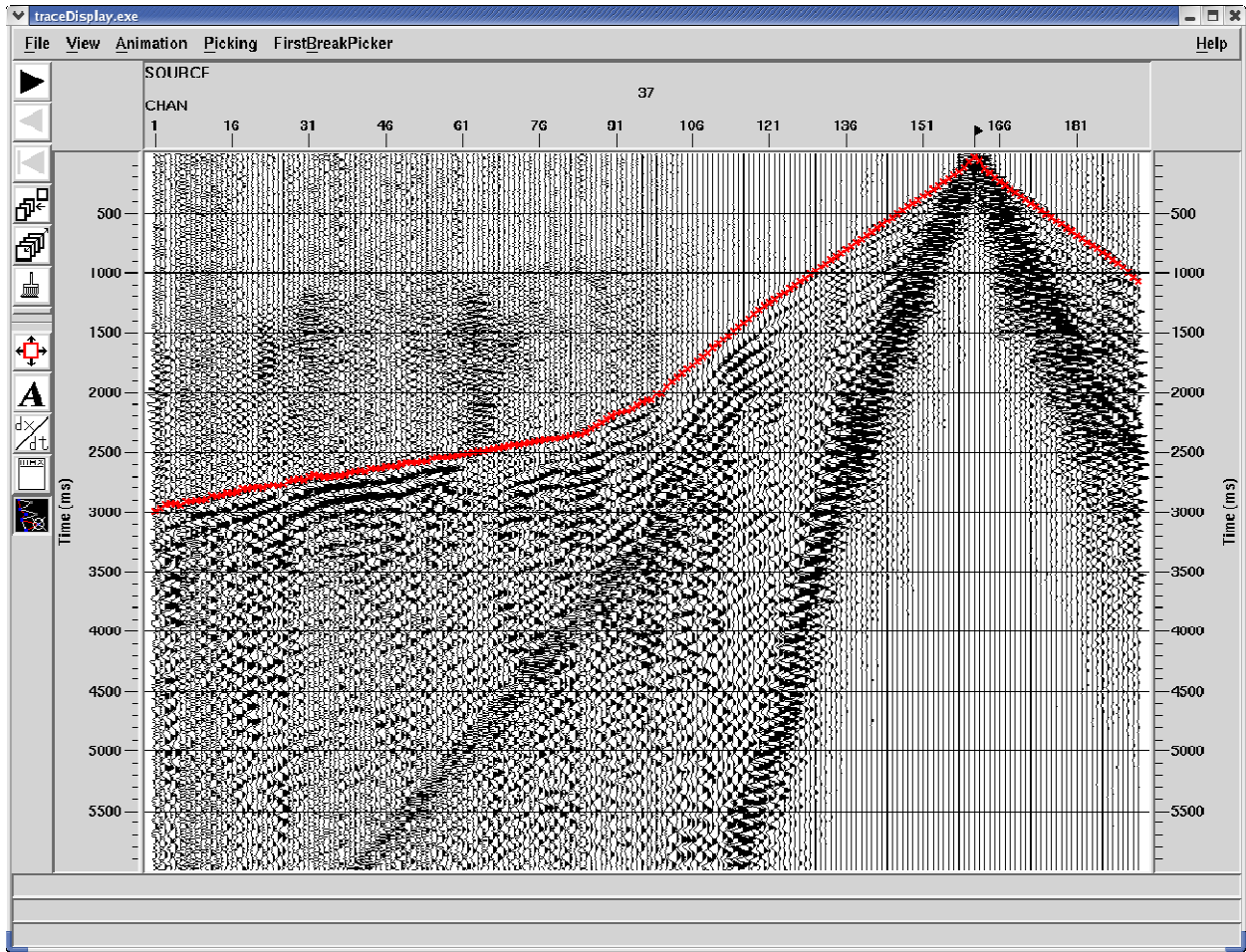


Figure 5c: Typical shot gathers from SH-wave data collected along Line 1 (100). The first arrival picks, shown in red, was used to obtain the S-wave velocity model shown in Figure 5e.

Figures 5d and 5e show the velocity model obtained from optimization of P-wave and SH-wave first arrival data (Pullammanappallil and Louie, 1994), respectively. P-wave velocities range from 1,500 ft/s to 15,000 ft/s at a depth of about 3,000 ft. High velocities in the range of 10,000 ft/s shallow towards the range front in the east. The S-wave velocities range from 500 ft/s to 10,000 ft/s. As with the P-wave velocities, the higher velocities shallow towards the east. The S-wave arrivals resolve velocities to deeper depth compared to the P-wave model. Both models show relatively low-velocity areas within the higher velocity horizon. There is a distinct lateral change in velocity around station 180.

This model is then extended in depth by interactive velocity modeling. It involved selecting an appropriate gradient that was consistent with the velocities observed along the other lines, including the intersecting Line 10 (101). Figure 5f shows results of a P-wave depth migration

(Louie and Qin, 1991) obtained using the P-wave velocity model shown in Figure 5d. Velocities are simply assumed to be a constant where there is no constraint. This model is then used for interpretation by the structural team led by Dr. Jim Faulds and Greg Rhodes. These are shown in Figures 5g, 5h and 5i. During the interpretation both the reflection images and the velocity model was used to identify faults and structures. Faults were inferred by direct reflections of them or by truncations of sub-horizontal reflections. The naming convention was developed by Greg Rhodes.

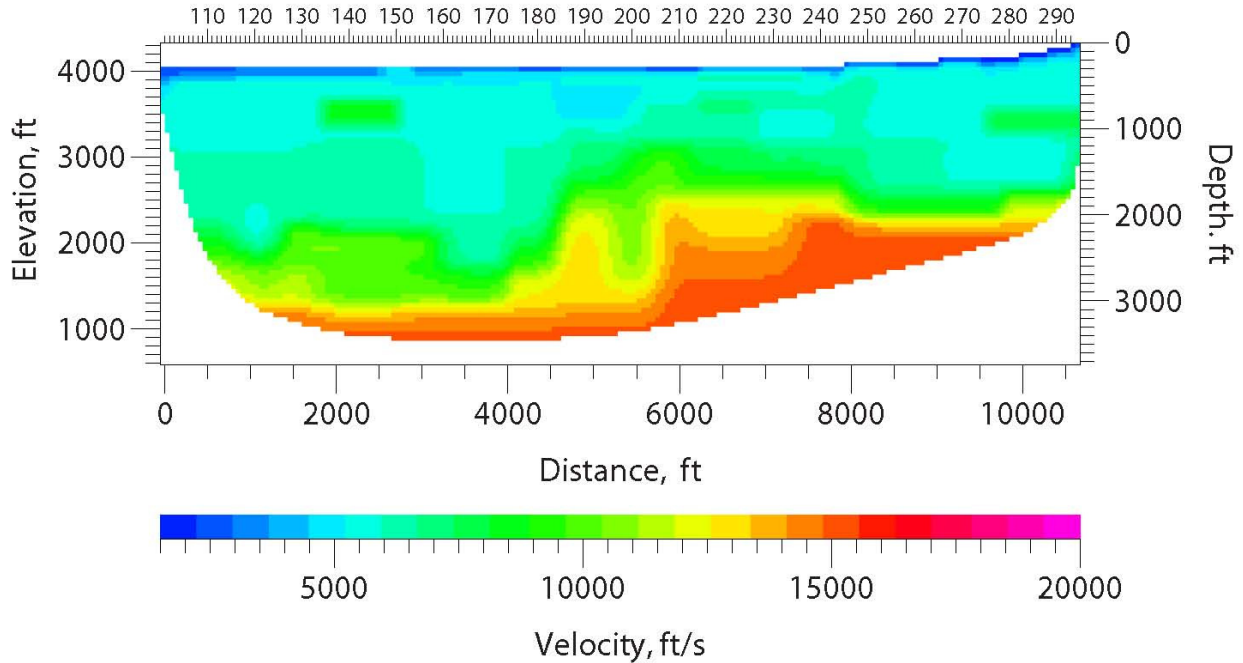


Figure 5d: P-wave velocity model along Line 1 (100) obtained from optimization of P-wave first-arrival travel times.

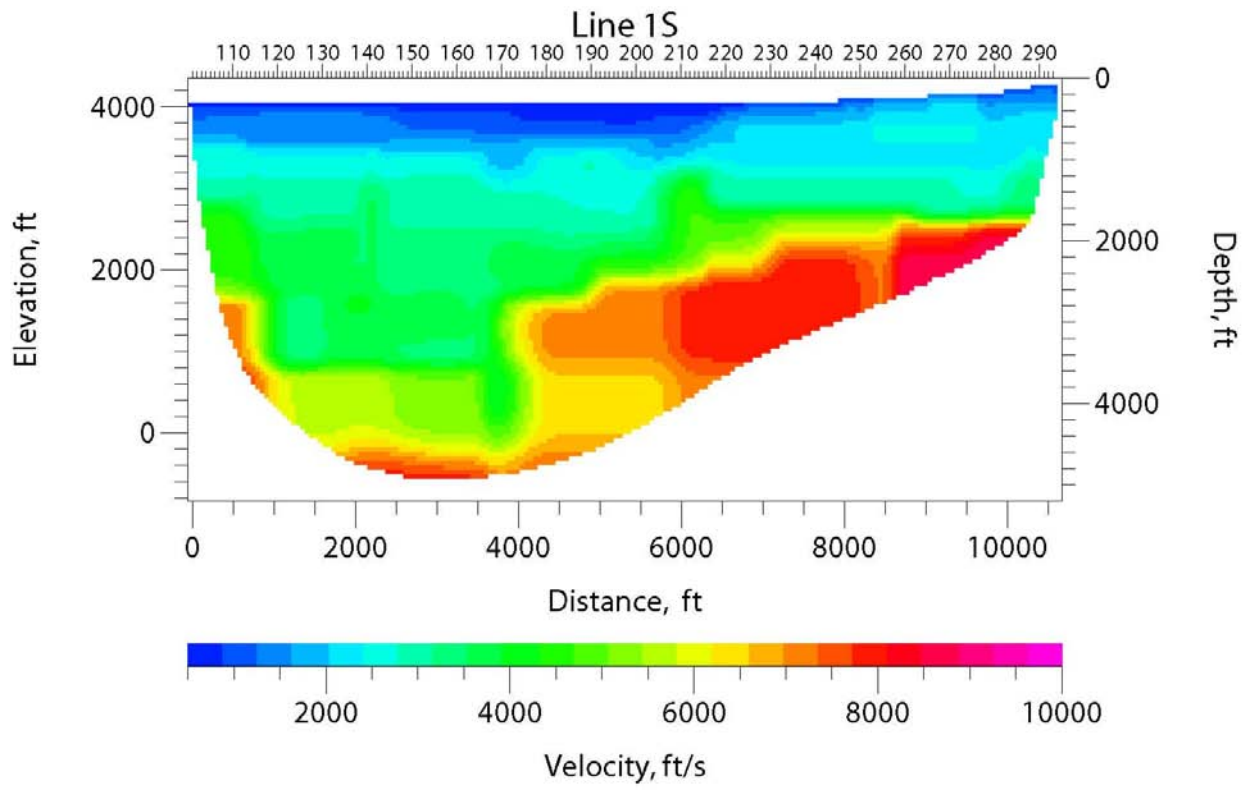


Figure 5e: S-wave velocity model along Line 1 (100) obtained from optimization of SH-wave first-arrival travel times.

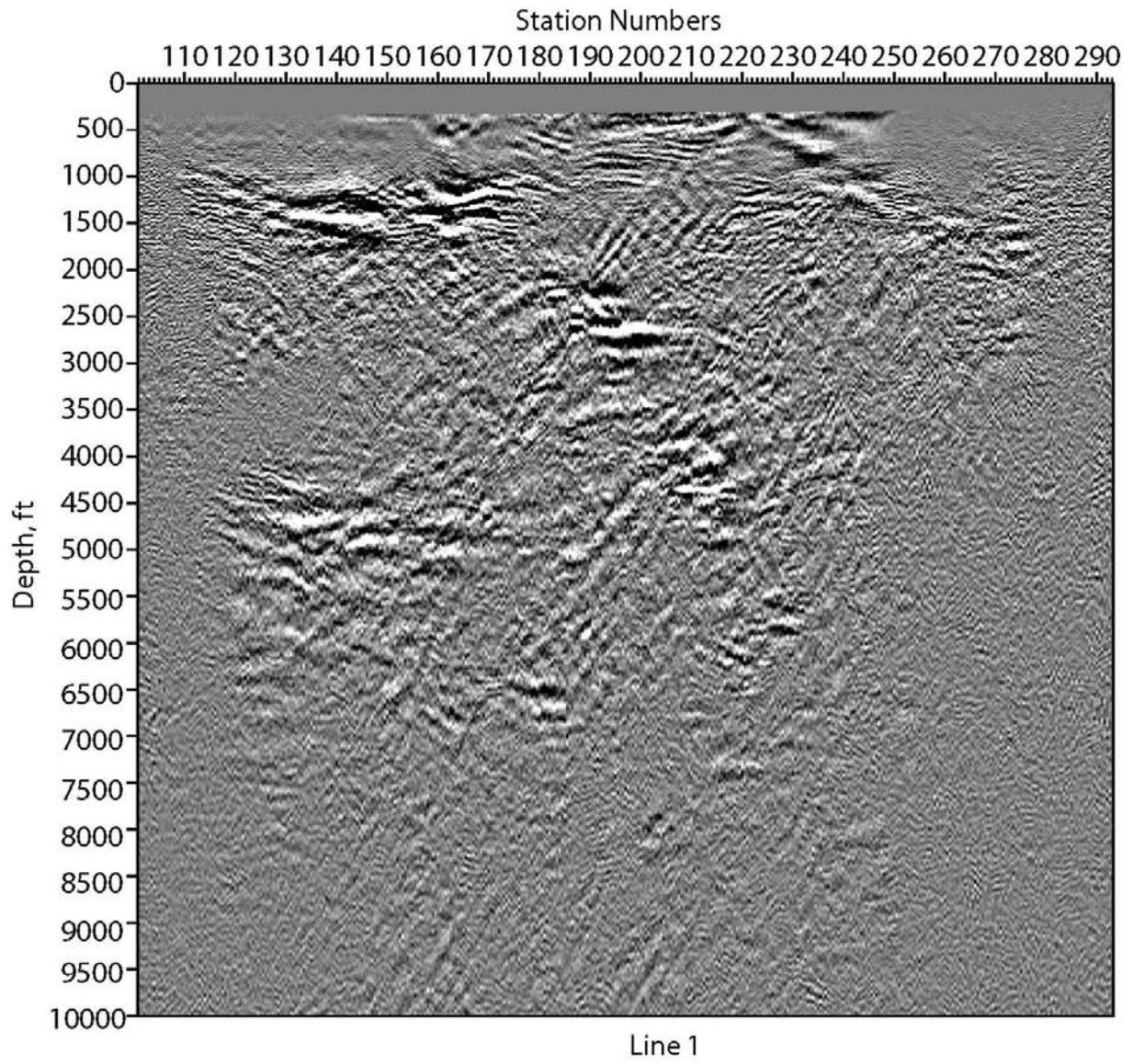


Figure 5f: Depth-migrated image along Line 1 (100) using the velocity model shown in Figure 5g.

### Line 100

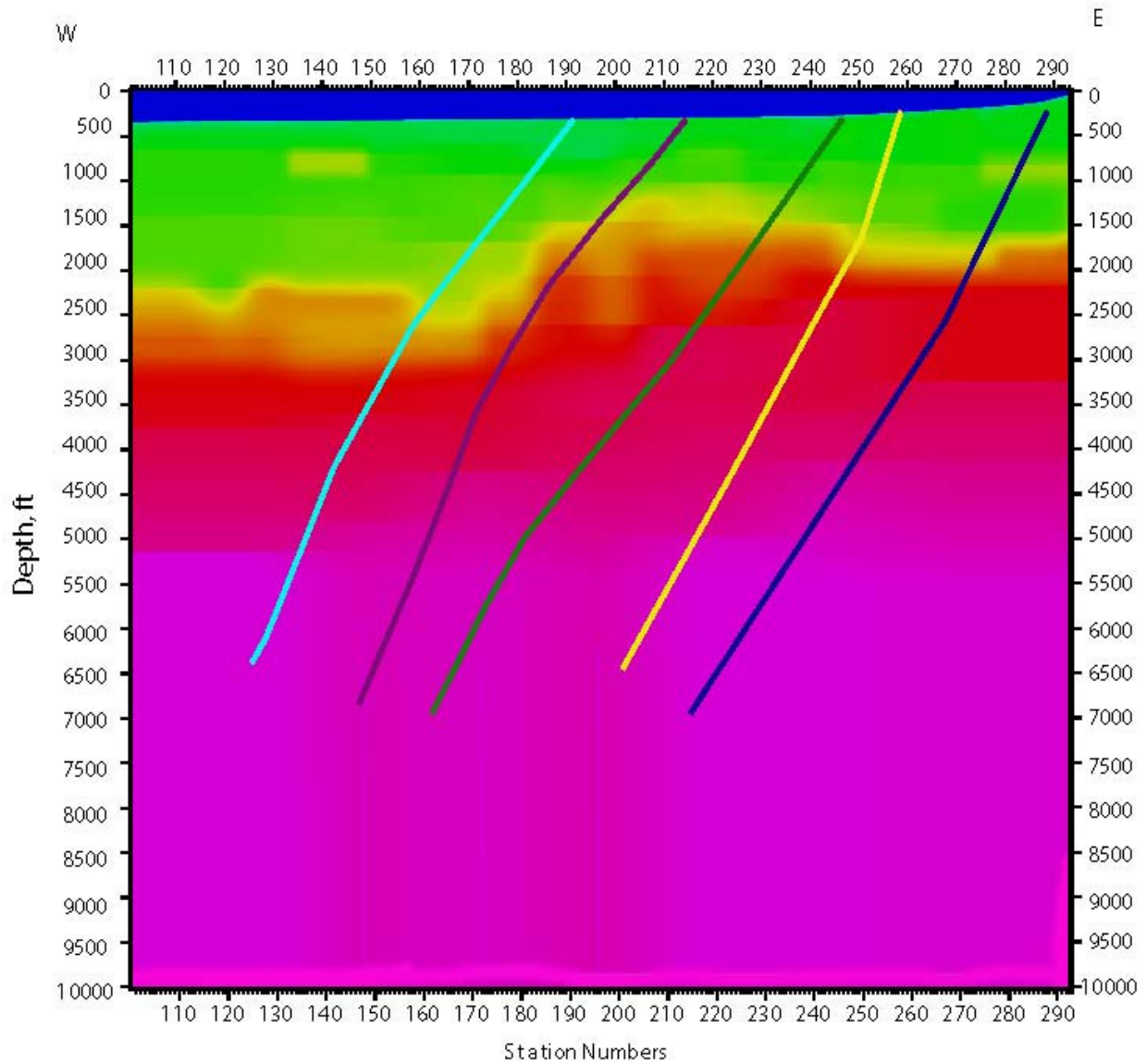


Figure 5g: P-wave velocity model along Line 1 (100) extended in depth. The interpretations were made in conjunction with the shear-wave velocity model (Figure 5h) and the reflection image (Figure 5i). Velocities go from 0 ft/s (blue) to 15,000 ft/s (purple).

# Line 100

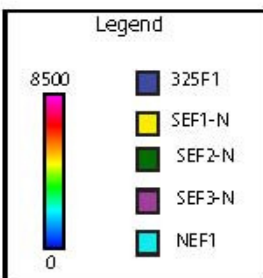
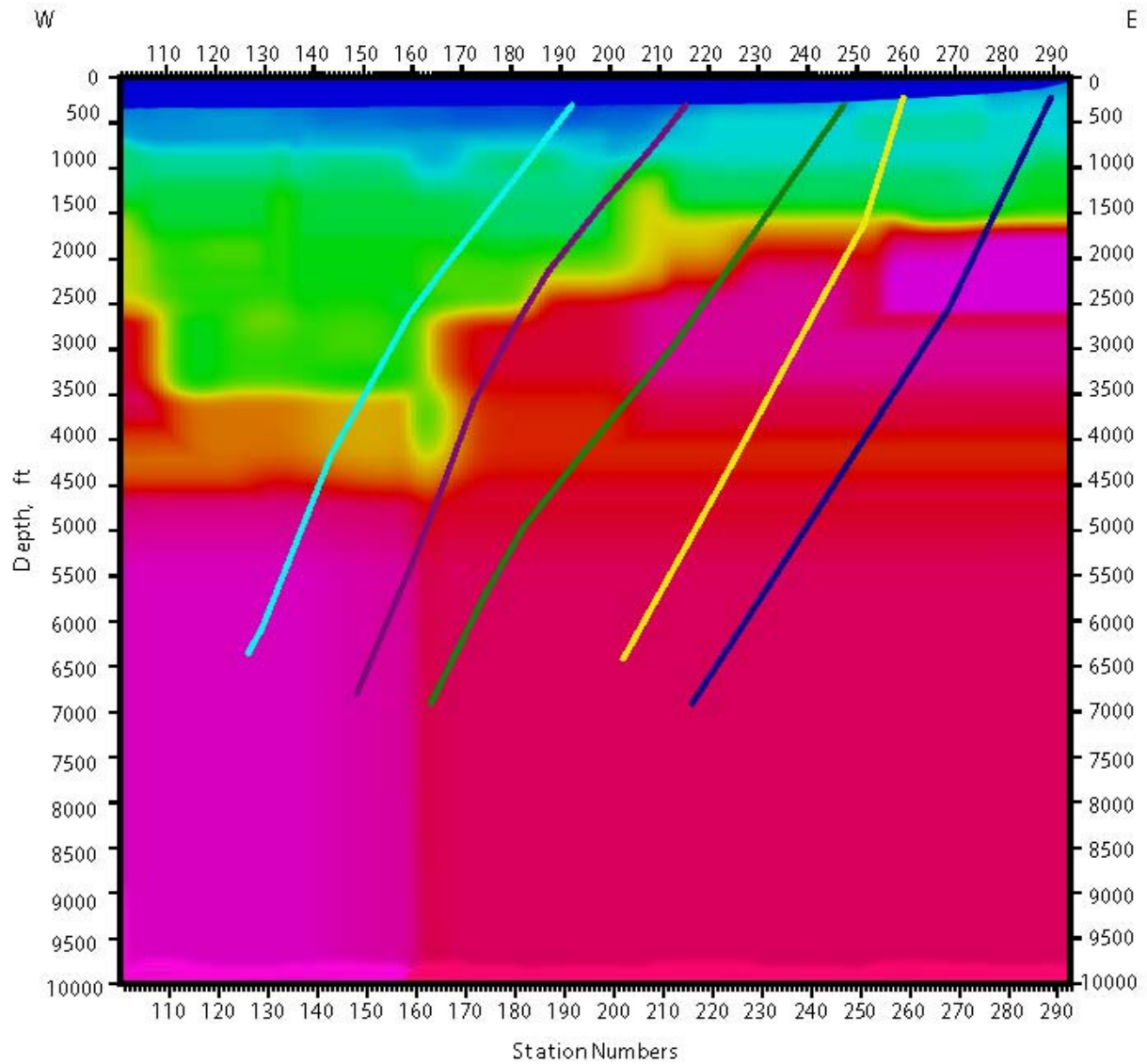


Figure 5h: S-wave velocity model along Line 1 (100) extended in depth showing the faults and discontinuities inferred by the structural team. The interpretations were made in conjunction with the P-wave velocity model (Figure 5g) and the reflection image (Figure 5i). Velocities go from 0 ft/s (blue) to 8,500 ft/s (purple).

# Line 100

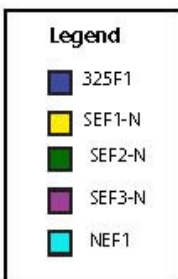
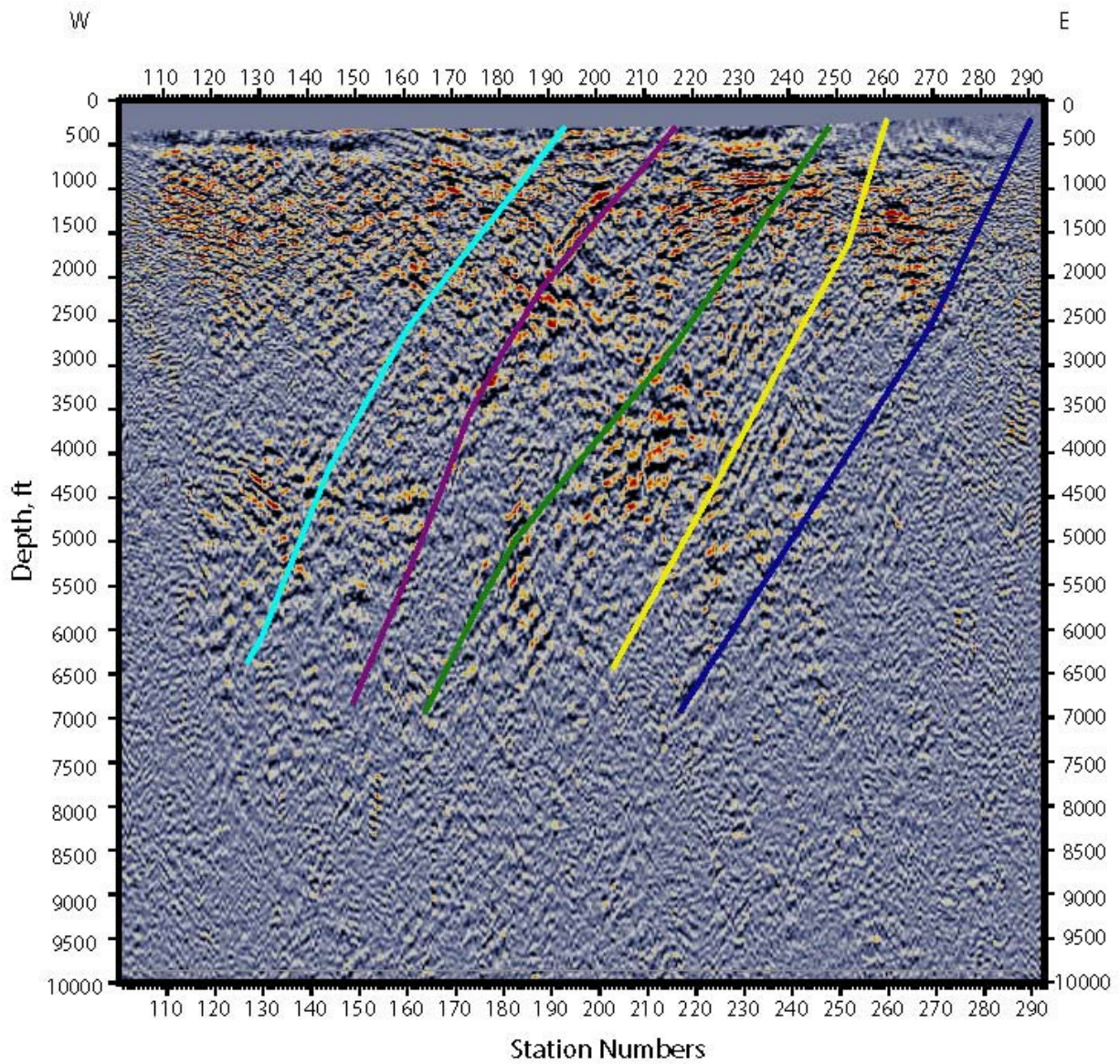


Figure 5i: P-wave depth migrated reflection image along Line 1 (100) showing the faults and discontinuities inferred by the structural team. The interpretations were made in conjunction with the P-wave velocity model (Figure 5g) and the shear-wave image (Figure 5h).

# Line 100

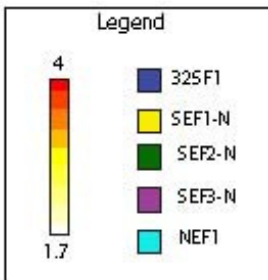
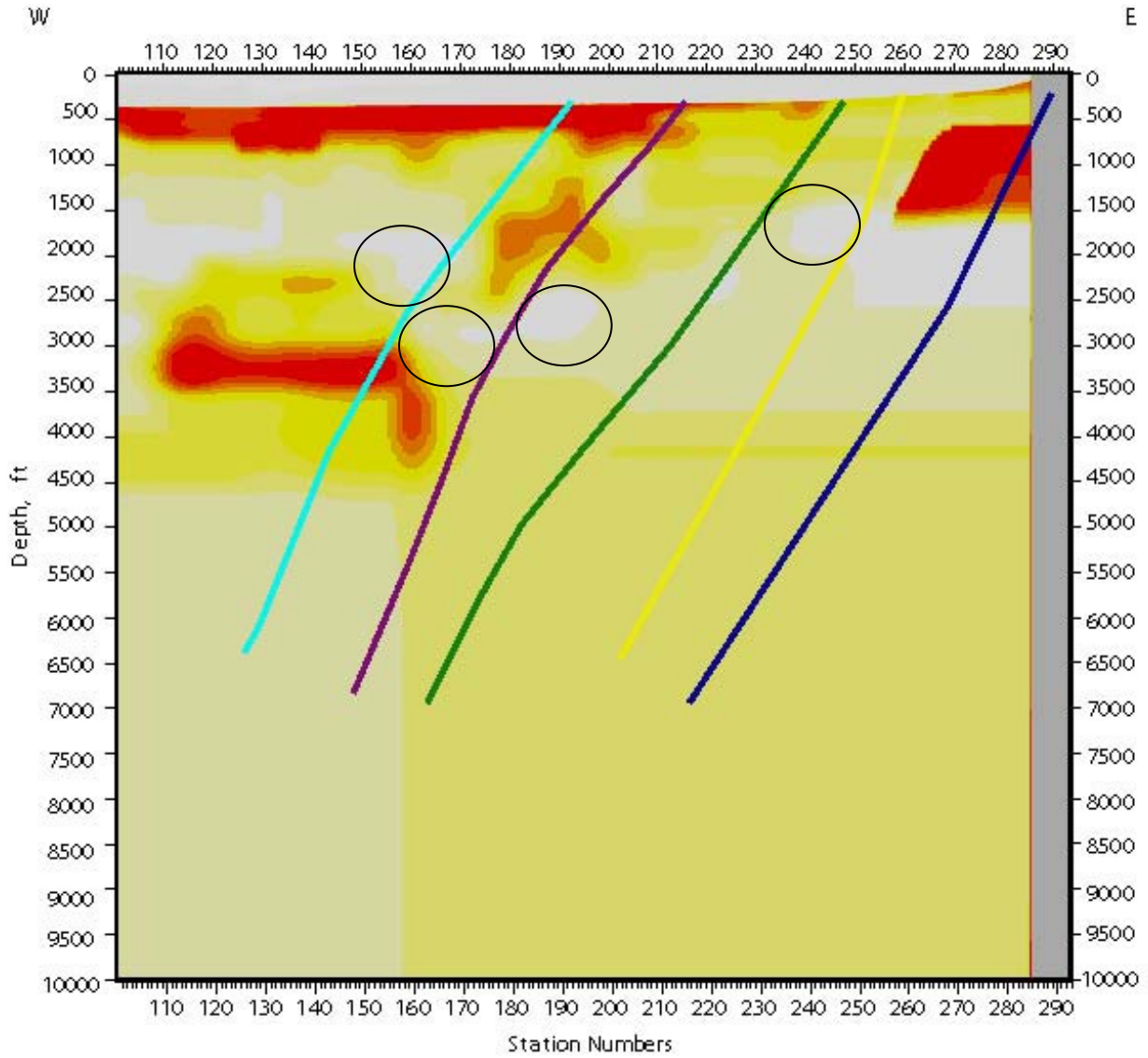


Figure 5j:  $V_p/V_s$  ratio calculated from P-wave and S-wave velocity models along Line 1 (100). The relatively lower  $V_p/V_s$  zones (circles) are potential fractured fluid filled zones.

We also calculate a  $V_p/V_s$  model from the P-wave and S-wave velocities and it is shown in Figure 5j. The relatively low  $V_p/V_s$  that fall along fault traces are shown as circles. These could be potential zones of fluid filled fractures.

#### 4.2 4.2 Line 2 (200)

Line 2, also called 200, is the in the northern part of the project area, just south of Line 1 (100), and runs east-west from station number 101 in the west to 293 in the east (Figure 6a). It crosses line 10 (101) at station number 290. All of the figures represent true seismic depth sections with no vertical exaggeration.

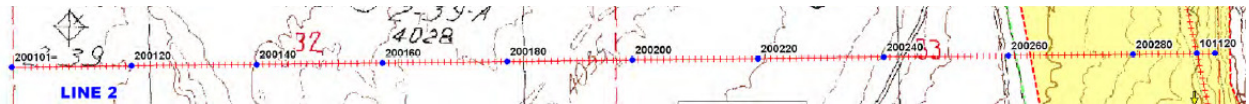


Figure 6a: Line 2 (200) runs east-west from station number 101 in the west to station number 293 in the east.

Figures 6b and 6c show a typical shot gather acquired along Line 2 using P-wave and SH-wave source, respectively. The first arrivals (shown in red) are clearly visible. These were picked and used to obtain the velocity models shown in Figures 6d and 6e, respectively.

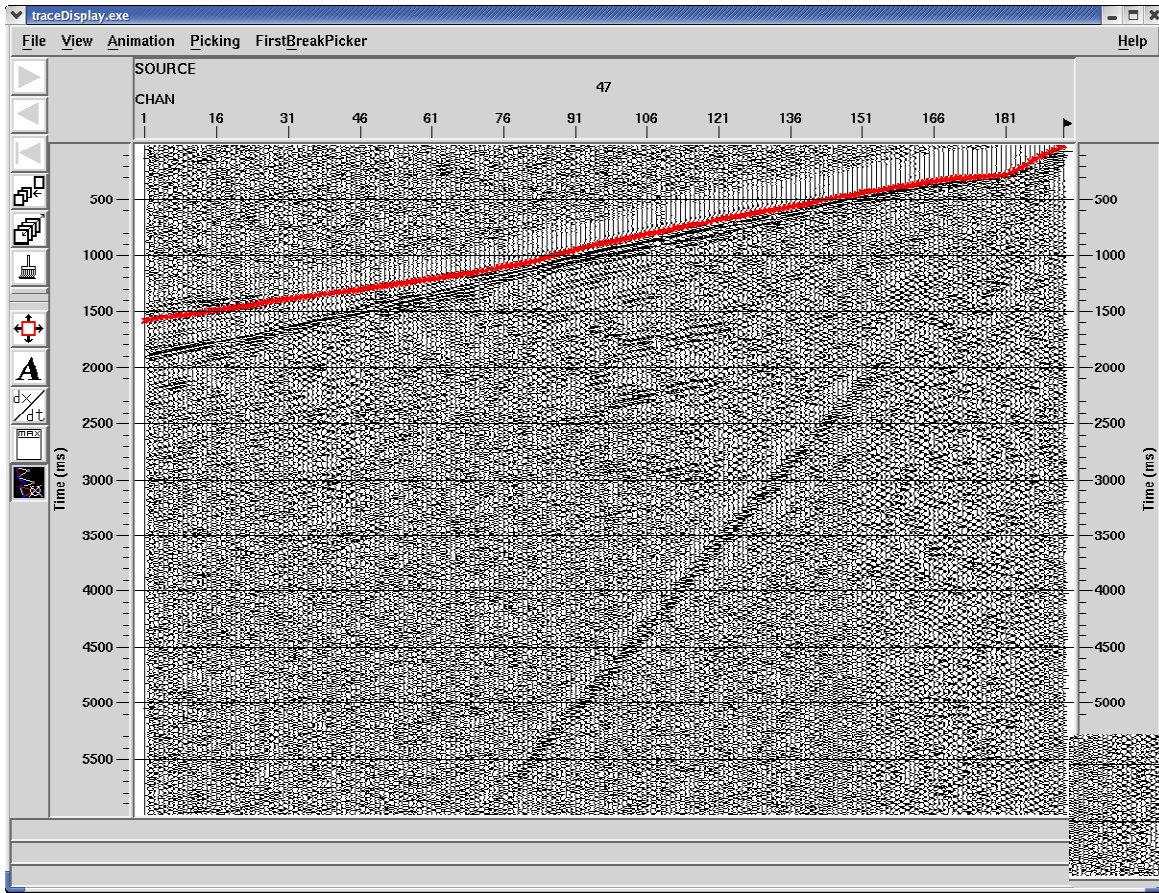


Figure 6b: Typical shot gathers from P-wave data collected along Line 2 (200). The first arrival picks, shown in red, was used to obtain the P-wave velocity model shown in Figure 6d.

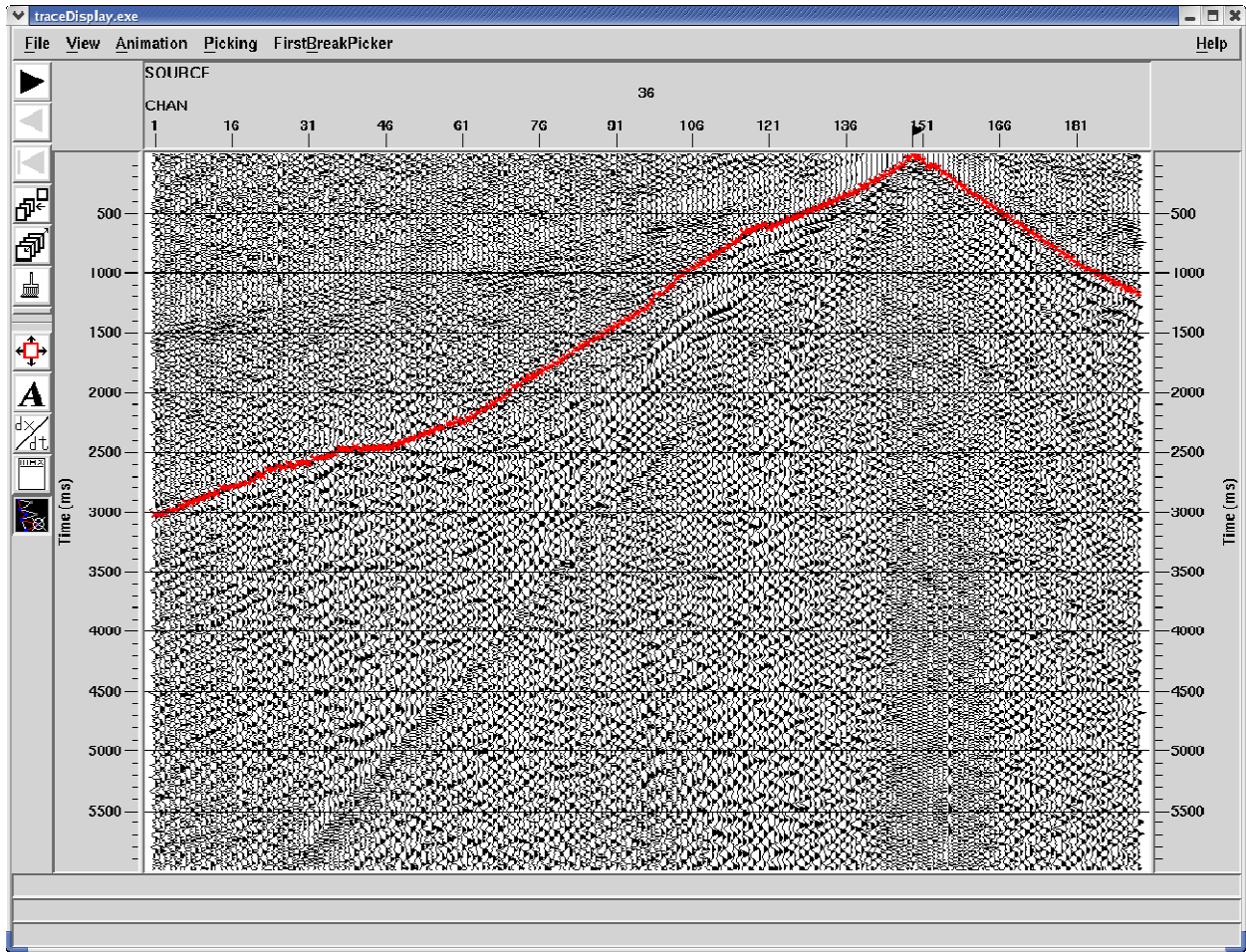


Figure 6c: Typical shot gathers from SH-wave data collected along Line 2 (200). The first arrival picks, shown in red, was used to obtain the S-wave velocity model shown in Figure 6e.

Figures 6d and 6e show the velocity model obtained from optimization of P-wave and SH-wave first arrival data (Pullammanappallil and Louie, 1994), respectively. P-wave velocities range from 1,500 ft/s to 15,000 ft/s at a depth of about 3,000 ft. High velocities in the range of 10,000 ft/s shallow towards the range front in the east. The S-wave velocities range from 500 ft/s to 10,000 ft/s. As with the P-wave velocities, the higher velocities shallow towards the east. The S-wave arrivals resolve velocities to deeper depth compared to the P-wave model. Both models show relatively low-velocity areas within the higher velocity horizon. There is a distinct lateral change in velocity around station 160.

This model is then extended in depth by interactive velocity modeling. It involved selecting an appropriate gradient that was consistent with the velocities observed along the other lines, including the intersecting Line 10 (101). Figure 6f shows results of a P-wave depth migration

(Louie and Qin, 1991) obtained using the P-wave velocity model shown in Figure 6d. Velocities are simply assumed to be a constant where there is no constraint. These are shown in Figures 6g, 6h and 6i. During the interpretation both the reflection images and the velocity model was used to identify faults and structures. Faults were inferred by direct reflections of them or by truncations of sub-horizontal reflections. The naming convention was developed by Greg Rhodes.

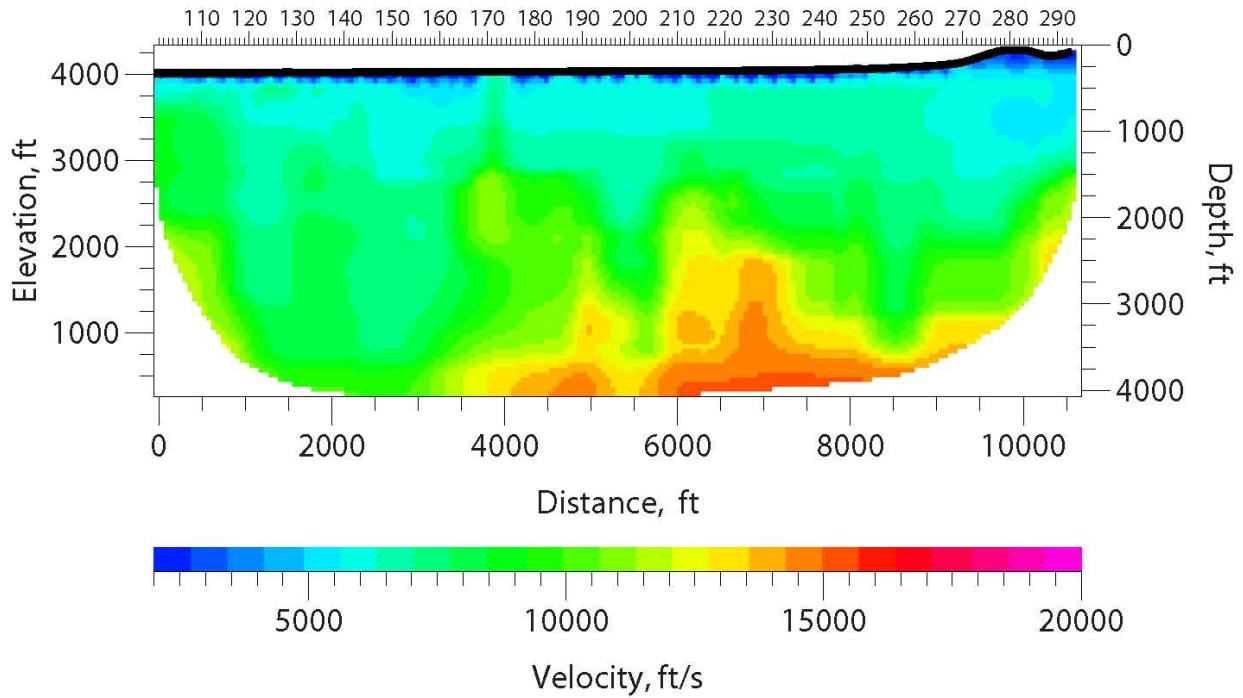


Figure 6d: P-wave velocity model along Line 2 (200) obtained from optimization of P-wave first-arrival travel times.

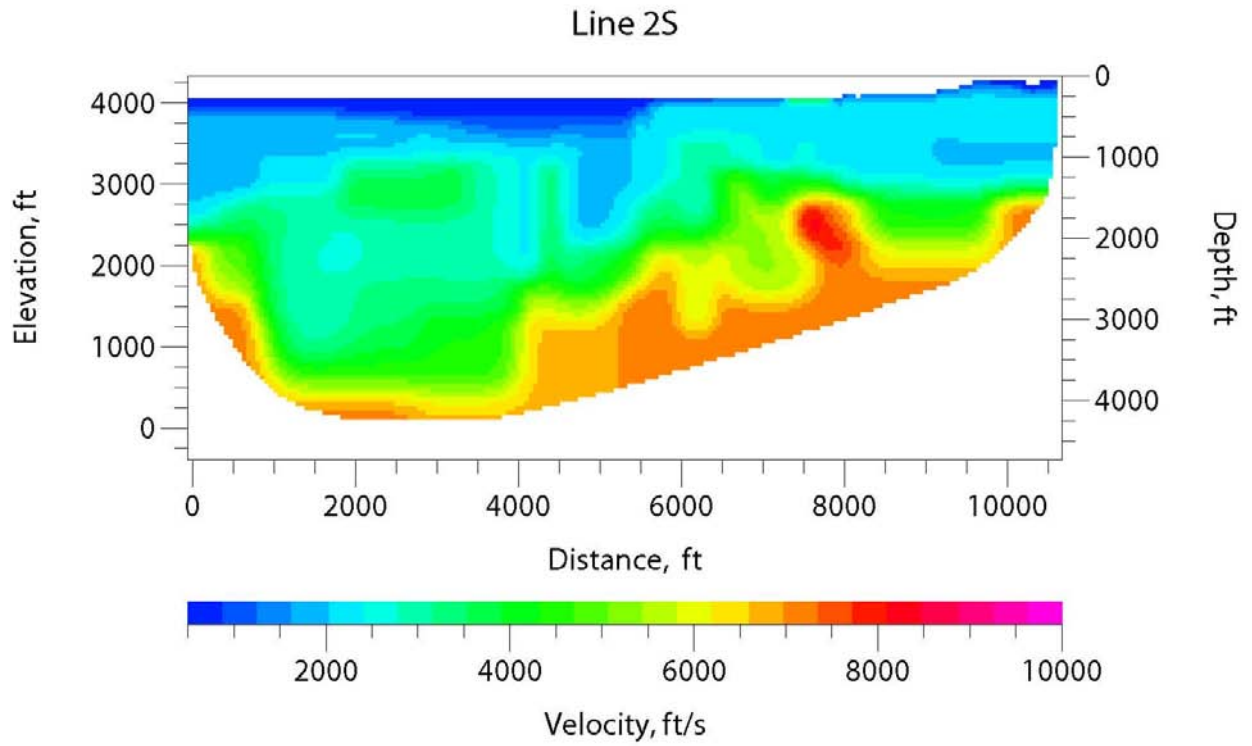


Figure 6e: S-wave velocity model along Line 2 (200) obtained from optimization of SH-wave first-arrival travel times.

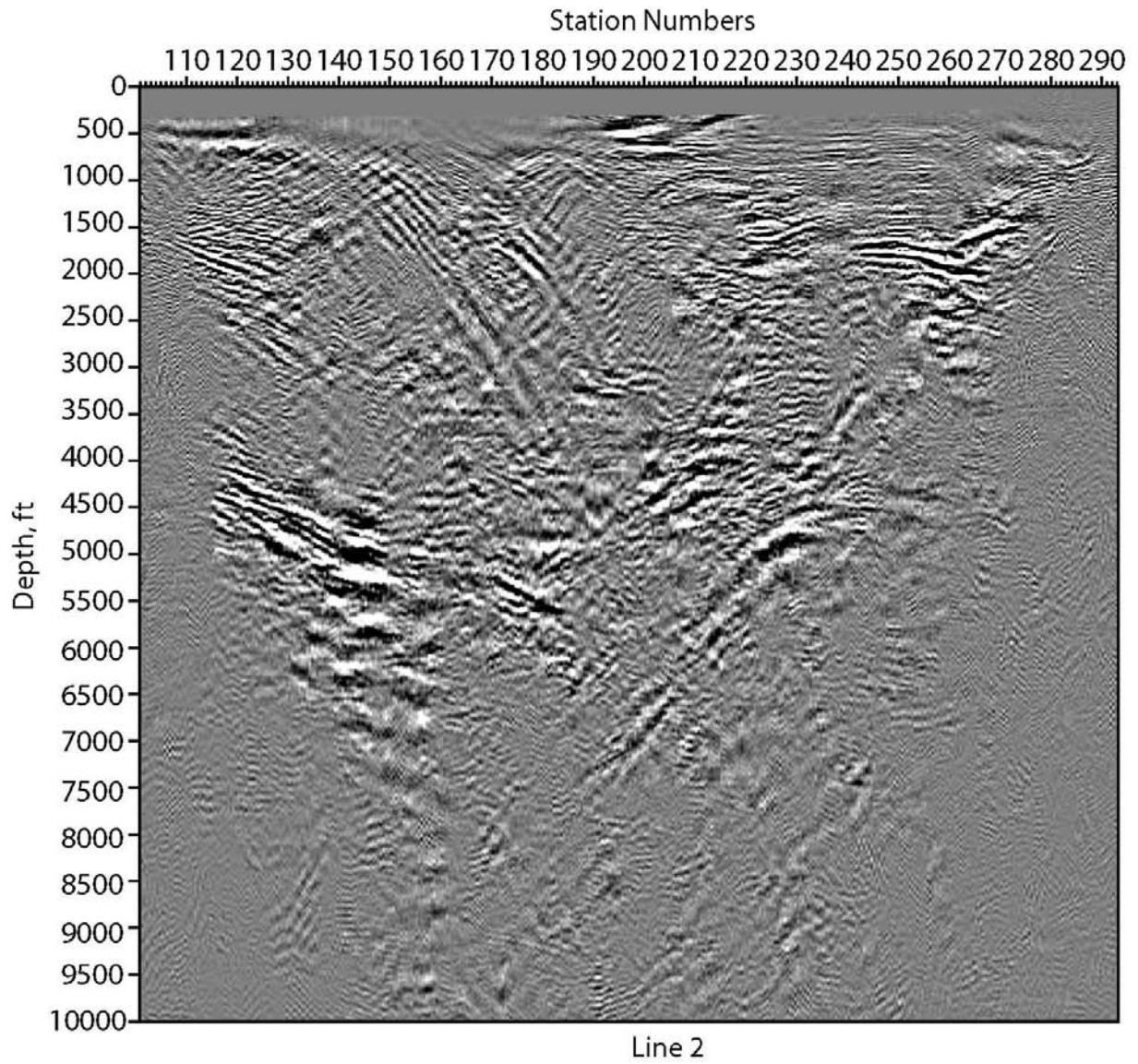


Figure 6f: Depth-migrated image along Line 2 (200) using the velocity model shown in Figure 6g.

### Line 200

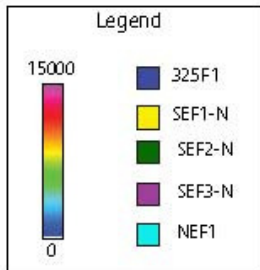
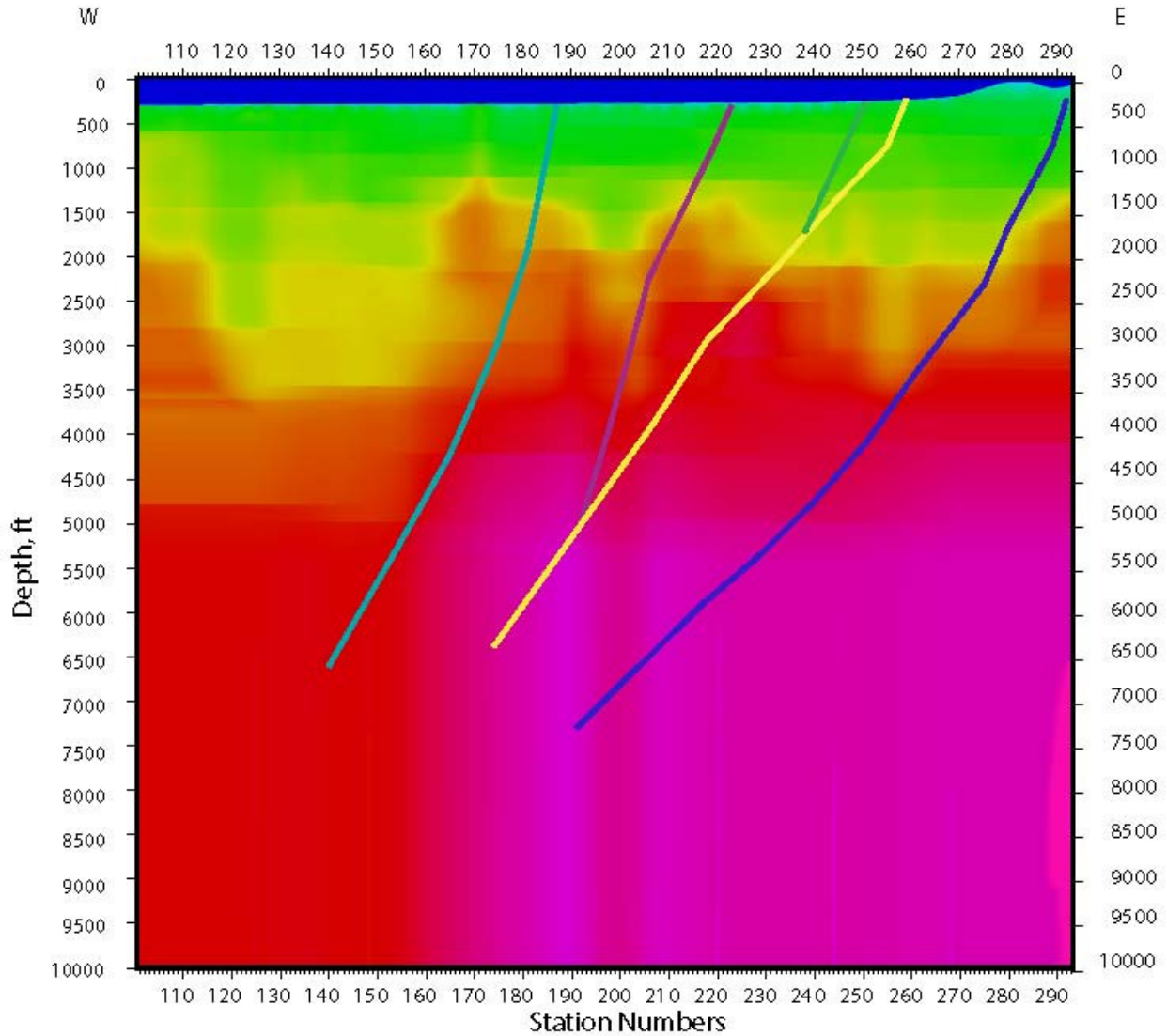


Figure 6g: P-wave velocity model along Line 2 (200) extended in depth. The interpretations were made in conjunction with the shear-wave velocity model (Figure 6h) and the reflection image (Figure 6i). Velocities go from 0 ft/s (blue) to 15,000 ft/s (purple).

# Line 200

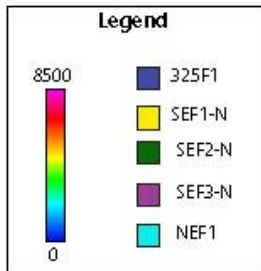
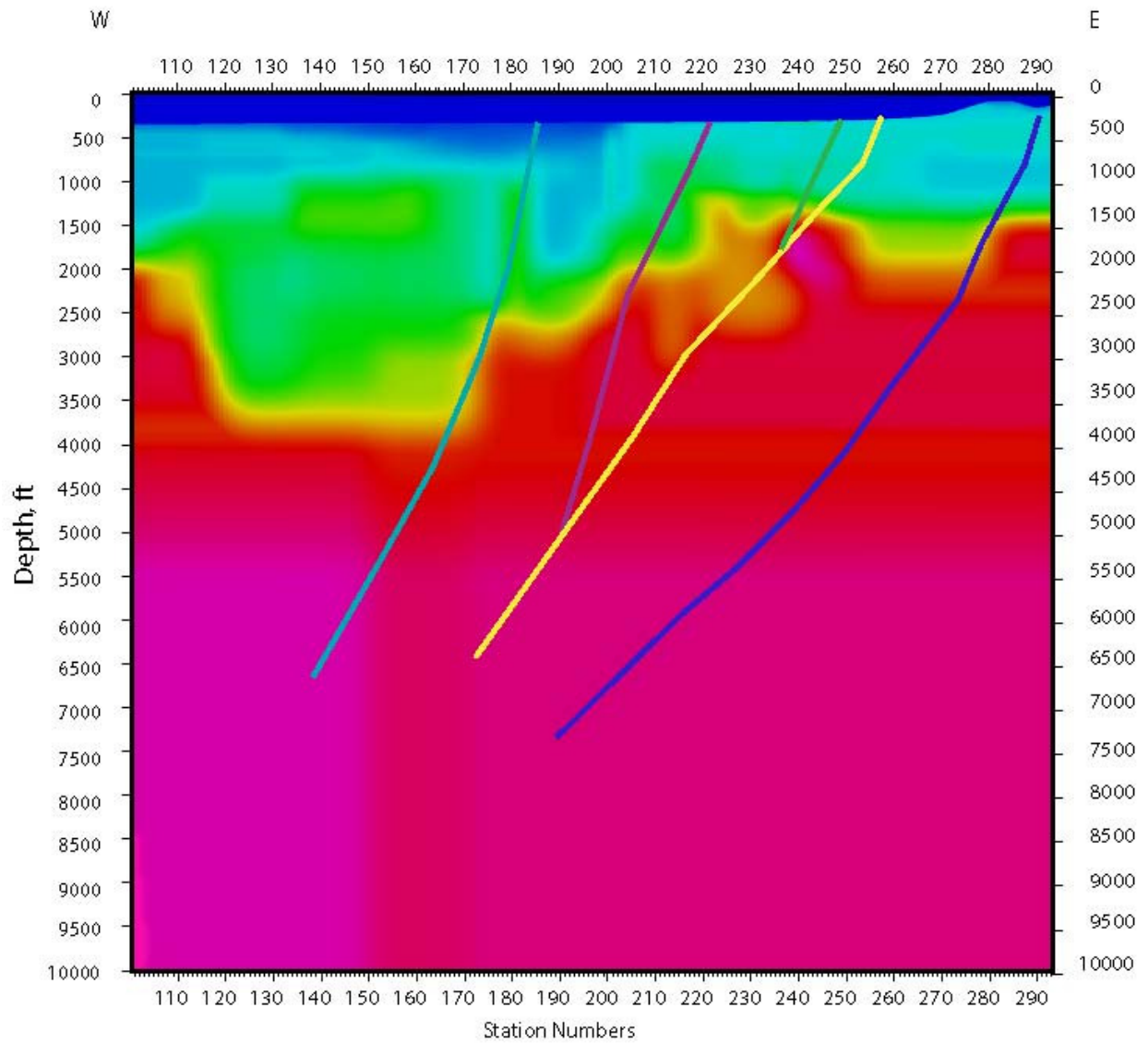


Figure 6h: S-wave velocity model along Line 2 (200) extended in depth showing the faults and discontinuities inferred by the structural team. The interpretations were made in conjunction with the P-wave velocity model (Figure 6g) and the reflection image (Figure 6i). Velocities go from 0 ft/s (blue) to 8,500 ft/s (purple).

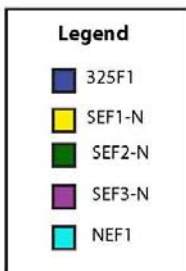
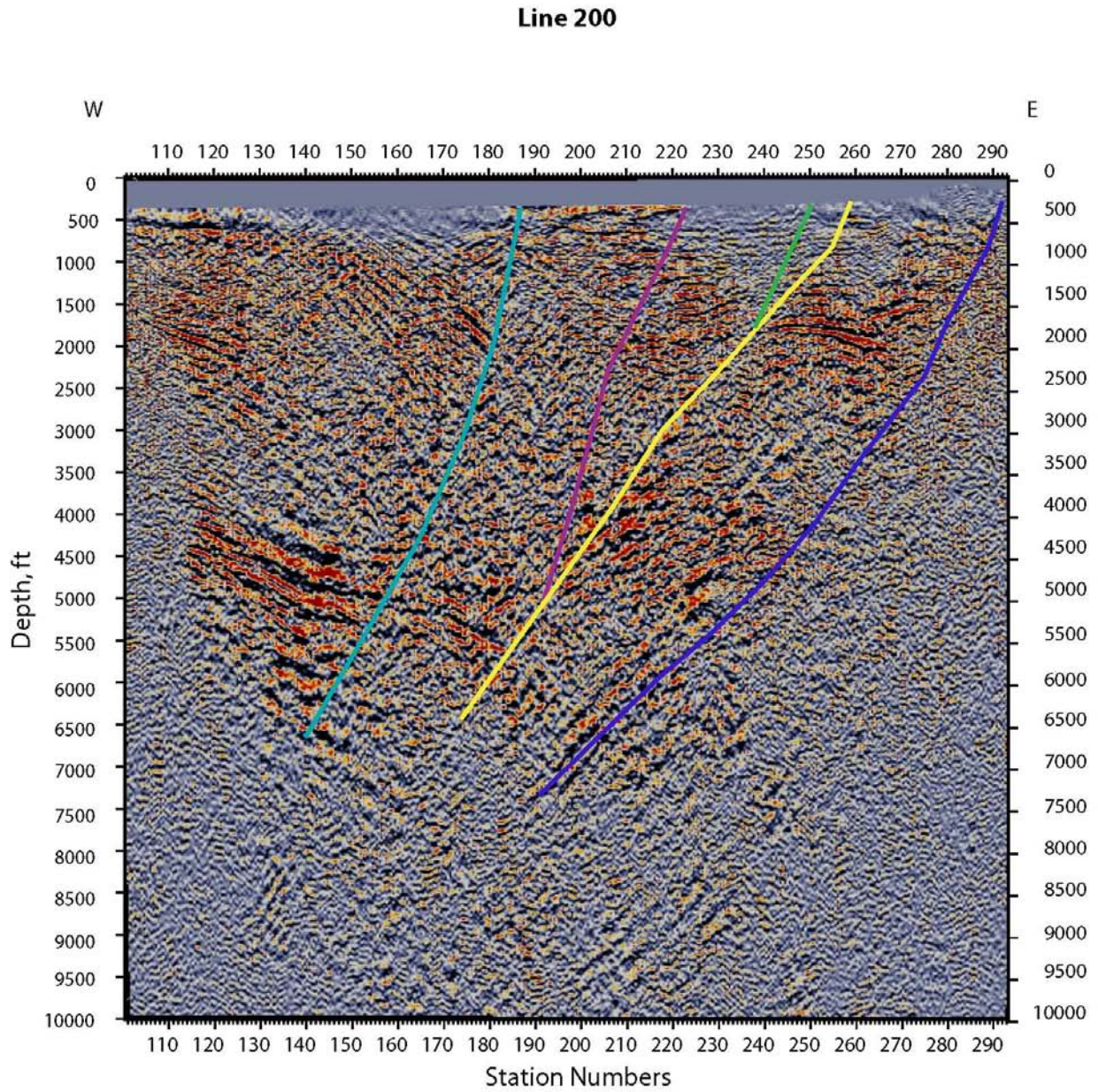


Figure 6i: P-wave depth migrated reflection image along Line 2 (200) showing the faults and discontinuities inferred by the structural team. The interpretations were made in conjunction with the P-wave velocity model (Figure 6g) and the shear-wave image (Figure 6h).

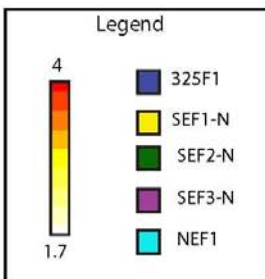
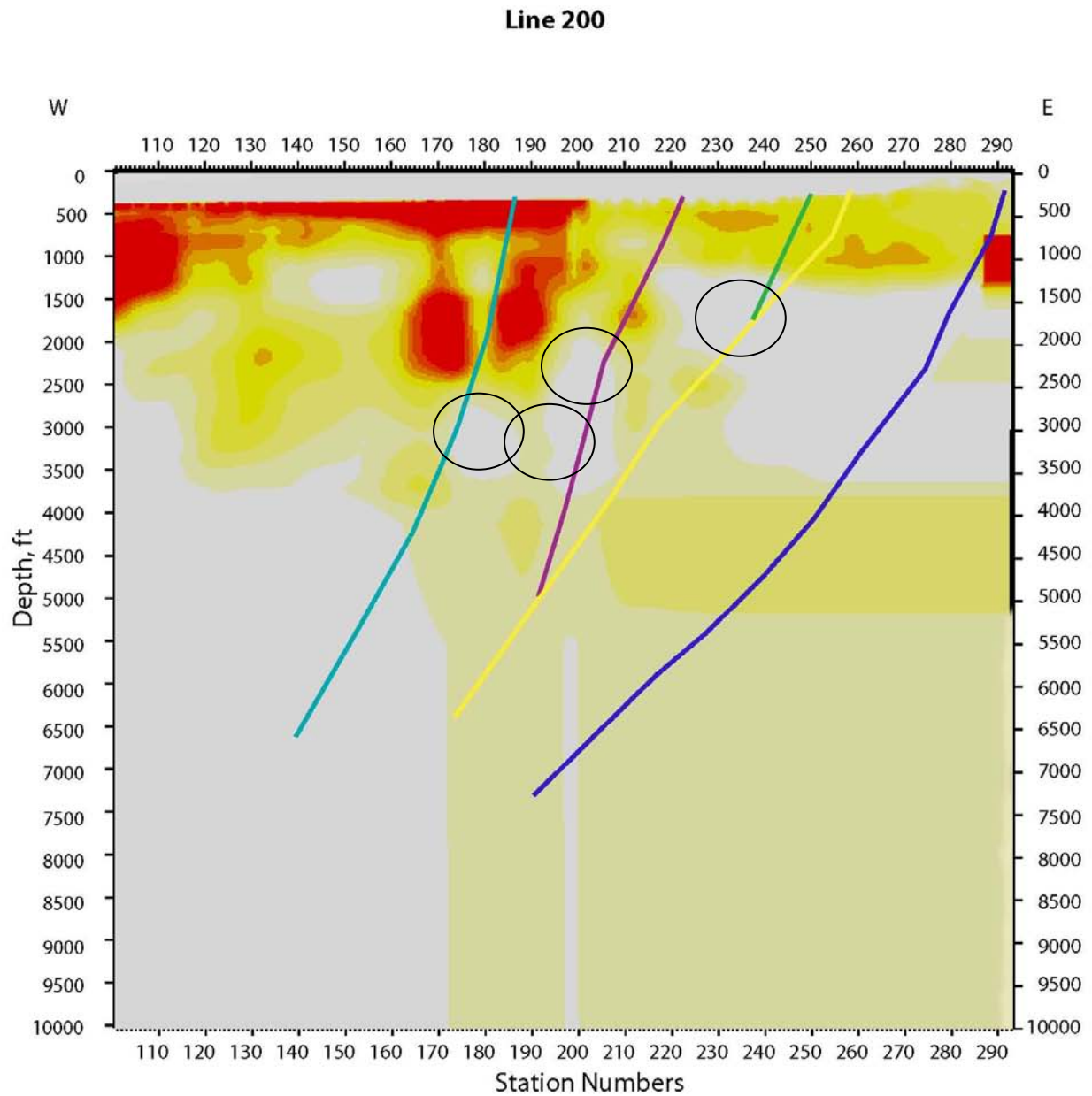


Figure 6j:  $V_p/V_s$  ratio calculated from P-wave and S-wave velocity models along Line 2 (100). The relatively lower  $V_p/V_s$  zones (circles) are potential fractured fluid filled zones.

In Figure 6j, low  $V_p/V_s$  zones that lie close to fault intersections and traces are marked as areas of potential fractured or fluid filled fracture zones.

### 4.3 4.3 Line 3 (300)

Line 3, also called 300, is the in the northern part of the project area, just south of Line 2 (200), and runs east-west from station number 101 in the west to 293 in the east (Figure 7a). It crosses line 10 (101) at station number 260. All of the figures represent true seismic depth sections with no vertical exaggeration.

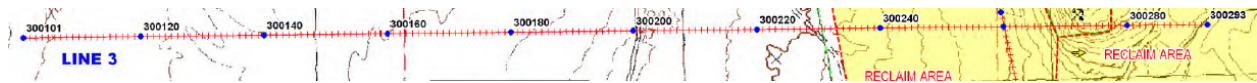


Figure 7a: Line 3 (300) runs east-west from station number 101 in the west to station number 293 in the east.

Figures 7b and 7c show a typical shot gather acquired along Line 3 using P-wave and SH-wave source, respectively. The first arrivals (shown in red) are clearly visible. These were picked and used to obtain the velocity models shown in Figures 7d and 7e, respectively.

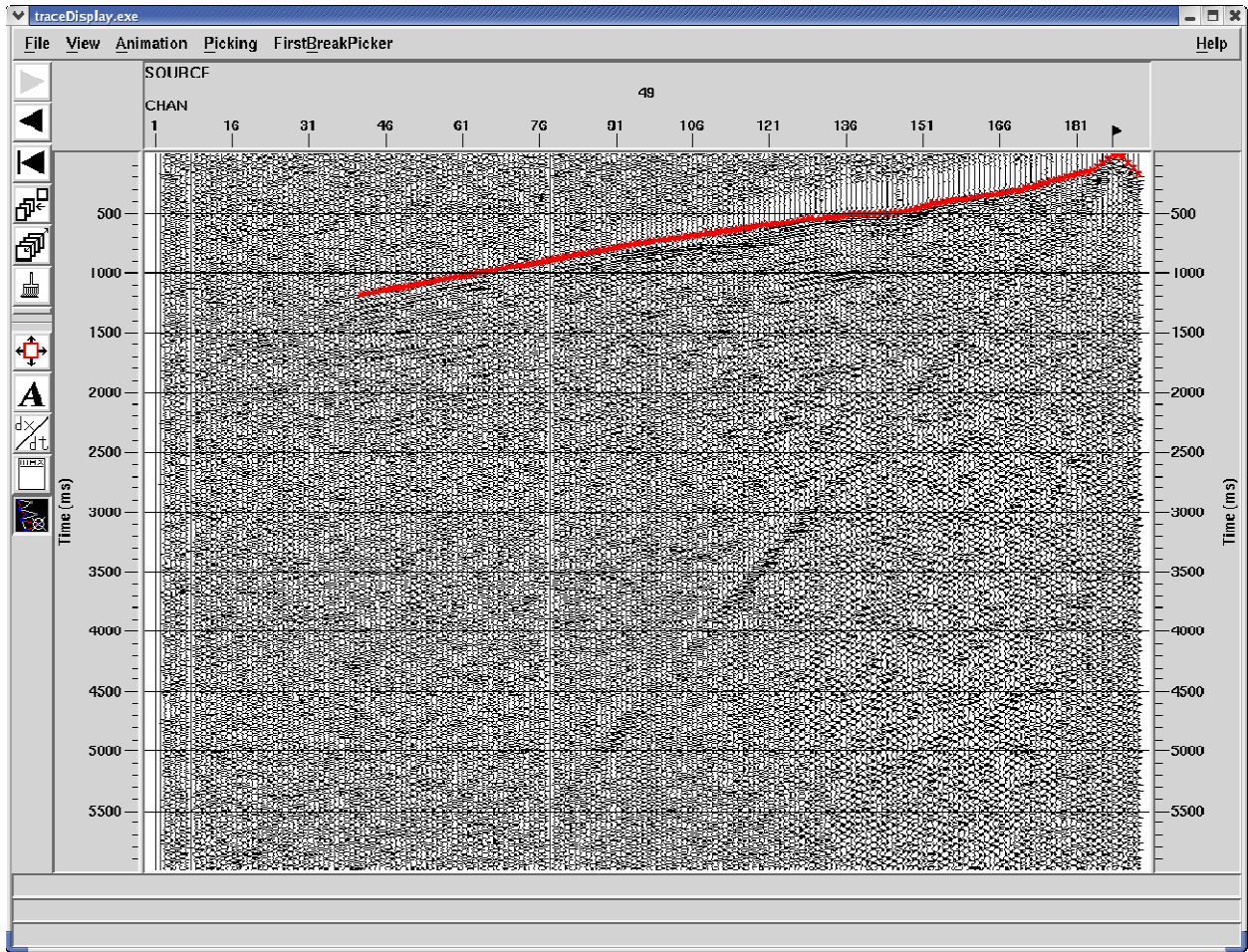


Figure 7b: Typical shot gathers from P-wave data collected along Line 3 (300). The first arrival picks, shown in red, was used to obtain the P-wave velocity model shown in Figure 7d.

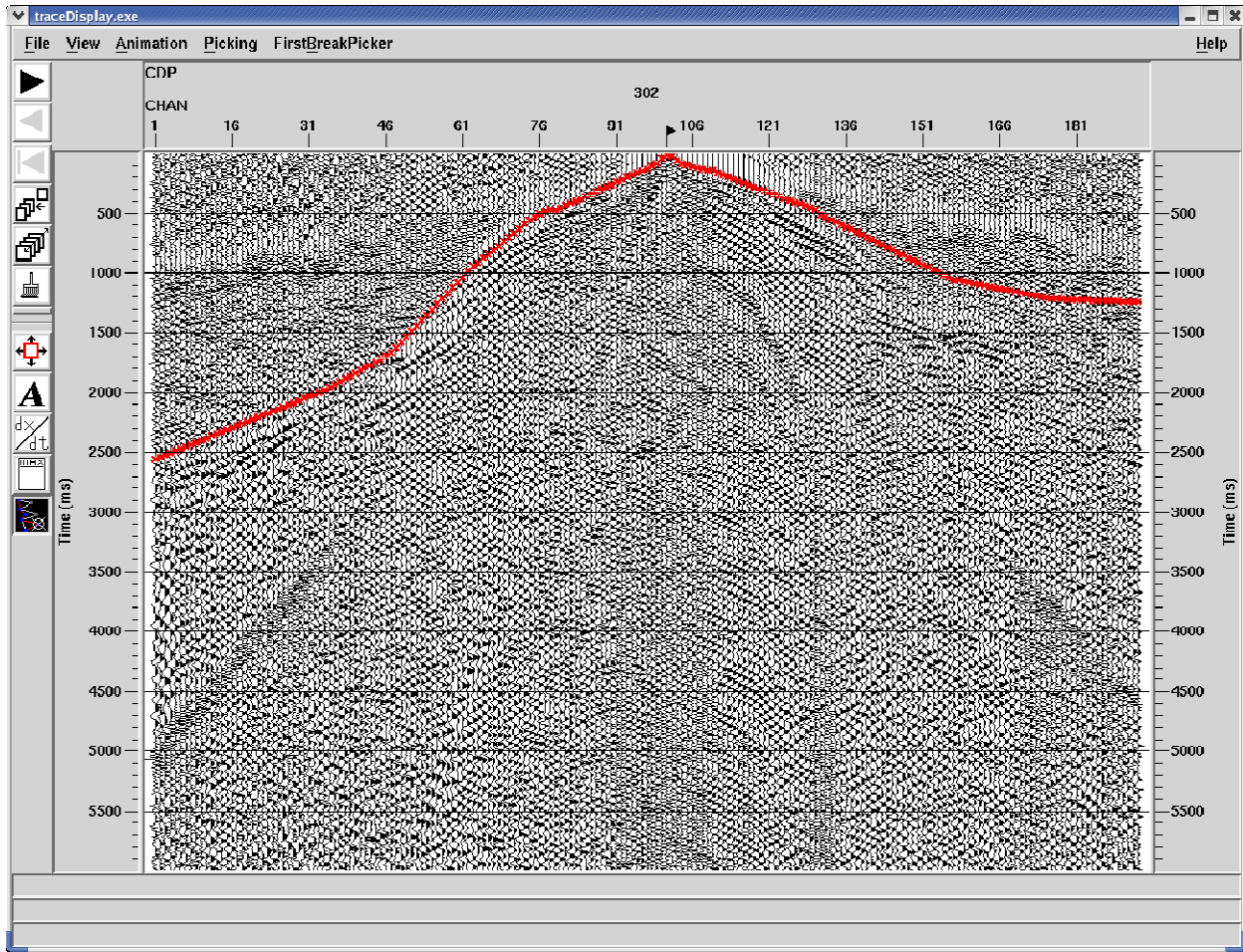


Figure 7c: Typical shot gathers from SH-wave data collected along Line 3 (300). The first arrival picks, shown in red, was used to obtain the S-wave velocity model shown in Figure 7e.

Figures 7d and 7e show the velocity model obtained from optimization of P-wave and SH-wave first arrival data (Pullammanappallil and Louie, 1994), respectively. P-wave velocities range from 1,500 ft/s to 15,000 ft/s at a depth of about 3,000 ft. High velocities in the range of 10,000 ft/s shallow towards the range front in the east. The S-wave velocities range from 500 ft/s to 10,000 ft/s. As with the P-wave velocities, the higher velocities shallow towards the east. The S-wave arrivals resolve velocities to deeper depth compared to the P-wave model. Both models show relatively low-velocity areas within the higher velocity horizons at depth. There is a distinct low velocity zone around station 140 at a depth of 1,200 feet.

This model is then extended in depth by interactive velocity modeling. It involved selecting an appropriate gradient that was consistent with the velocities observed along the other lines, including the intersecting Line 10 (101). Figure 7f shows results of a P-wave depth migration

(Louie and Qin, 1991) obtained using the P-wave velocity model shown in Figure 7d. Velocities are simply assumed to be a constant where there is no constraint. These are shown in Figures 7g, 7h and 7i. During the interpretation both the reflection images and the velocity model was used to identify faults and structures. Faults were inferred by direct reflections of them or by truncations of sub-horizontal reflections. The naming convention was developed by Greg Rhodes.

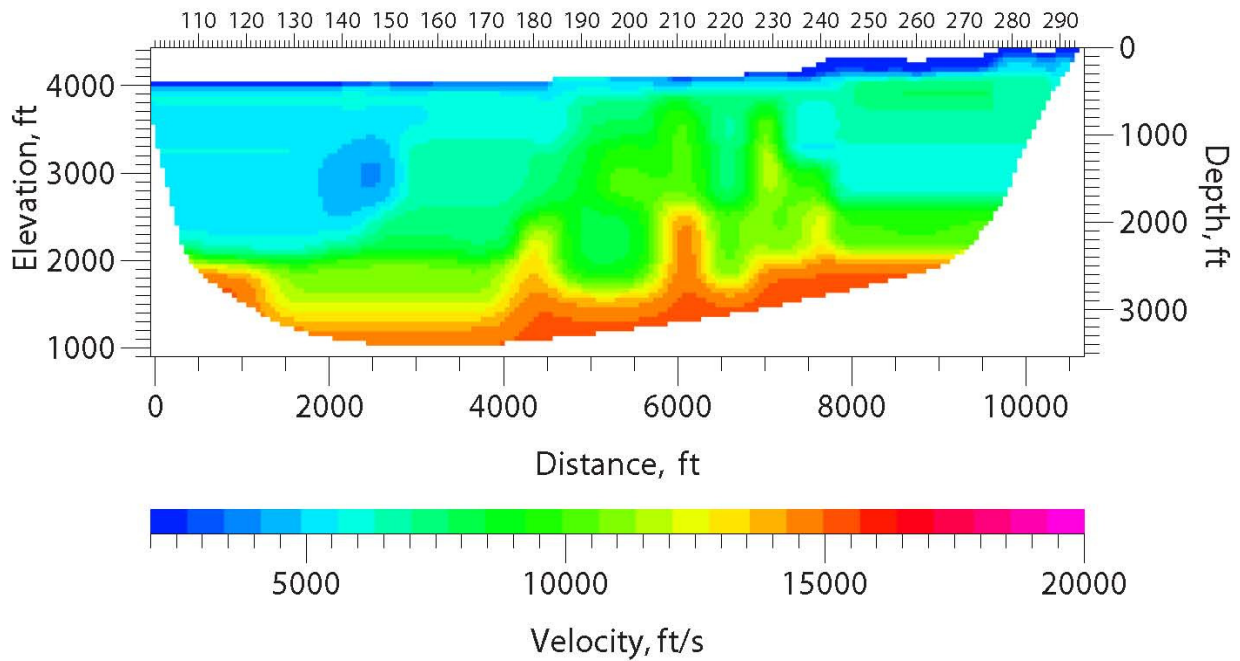


Figure 7d: P-wave velocity model along Line 3 (300) obtained from optimization of P-wave first-arrival travel times.

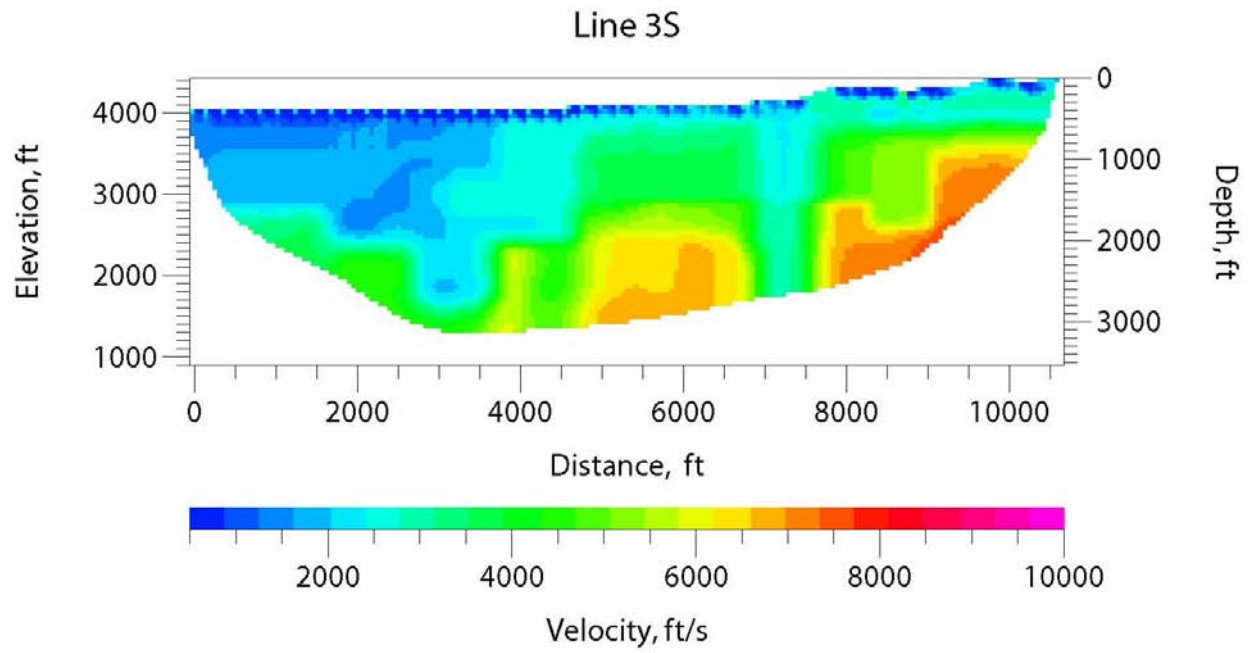


Figure 7e: S-wave velocity model along Line 3 (300) obtained from optimization of SH-wave first-arrival travel times.

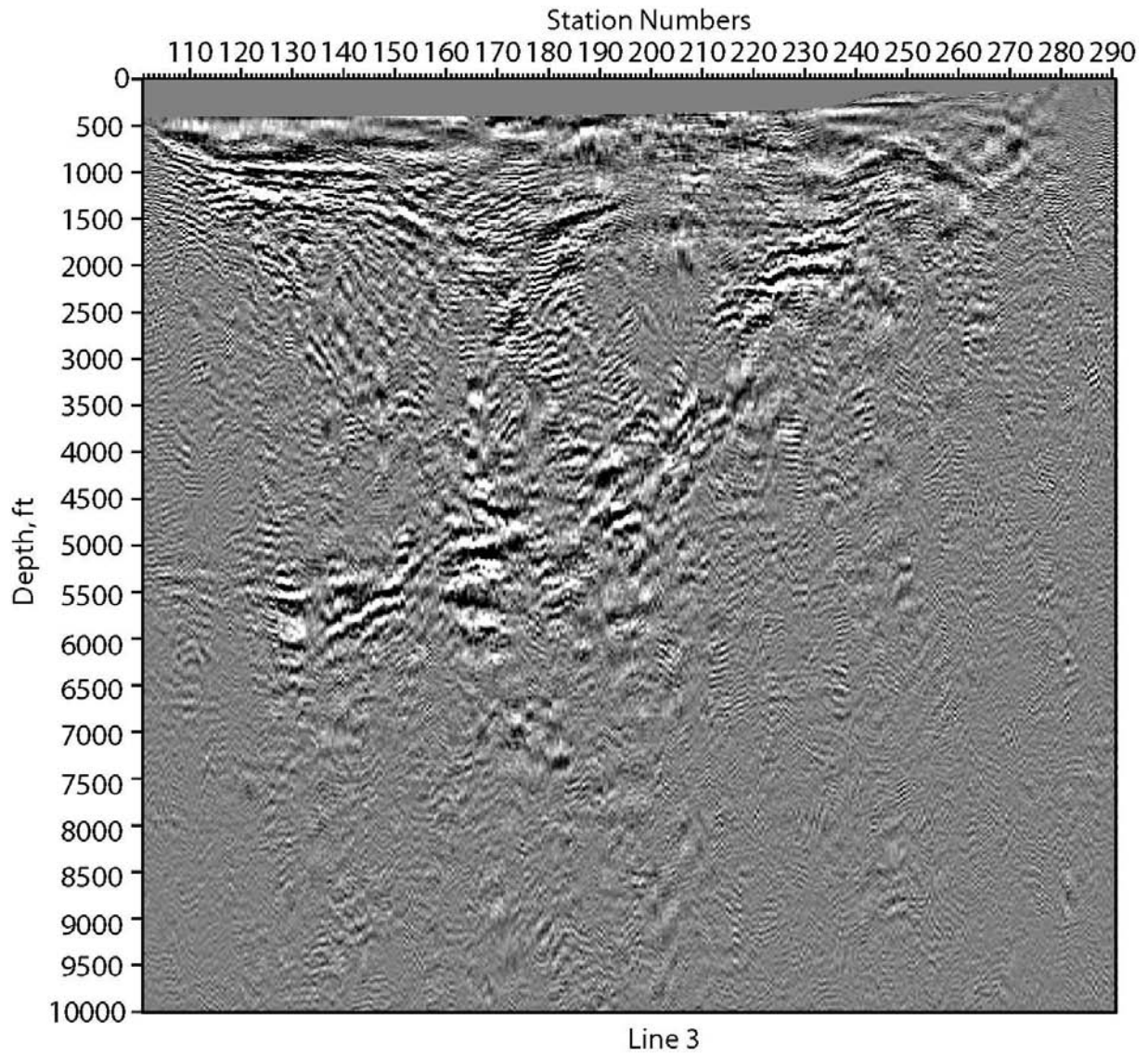


Figure 7f: Depth-migrated image along Line 3 (300) using the velocity model shown in Figure 7g.

### Line 300

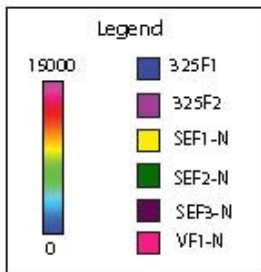
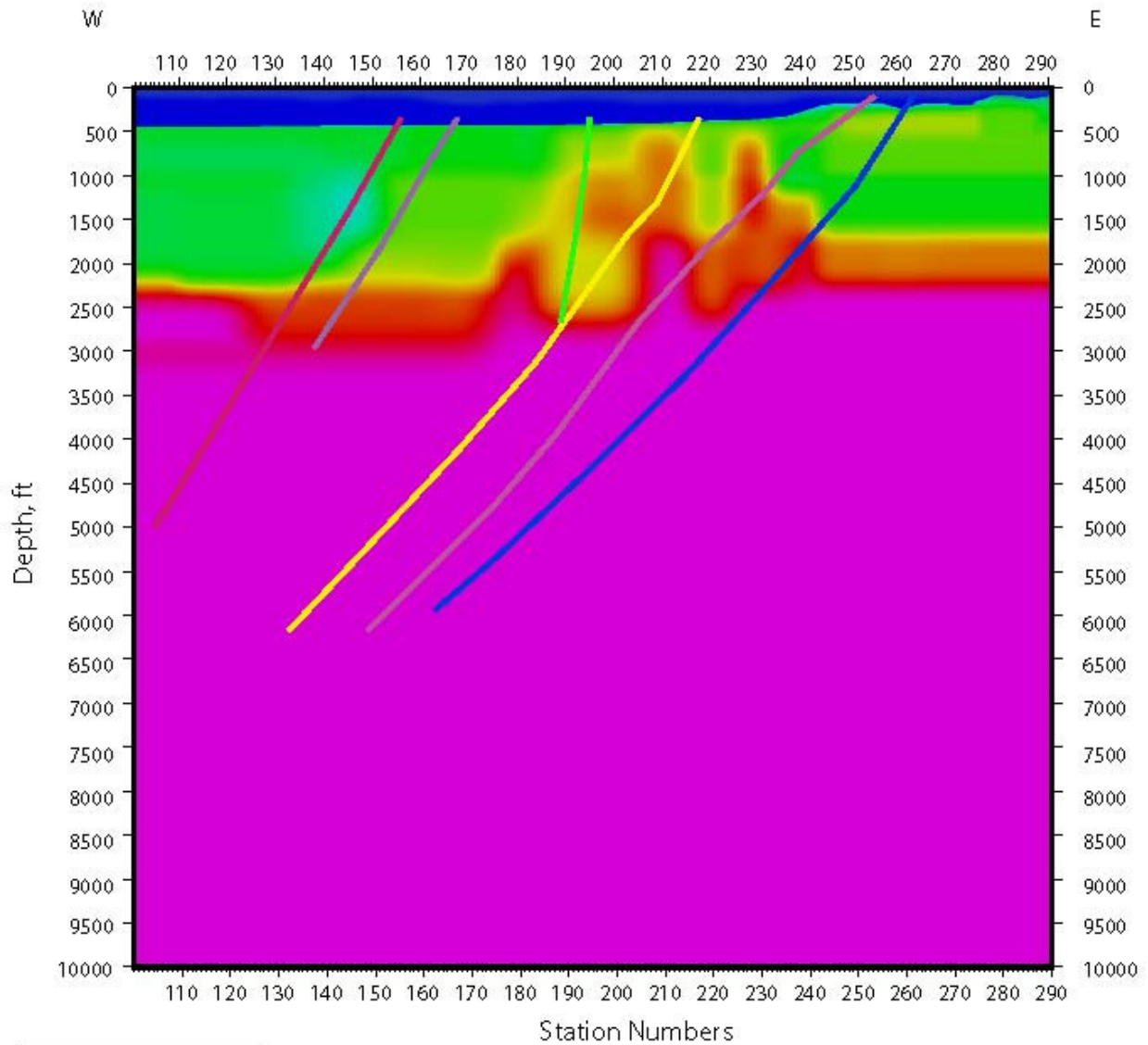


Figure 7g: P-wave velocity model along Line 3 (300) extended in depth. The interpretations were made in conjunction with the shear-wave velocity model (Figure 7h) and the P-wave reflection image (Figure 7i). Velocities go from 0 ft/s (blue) to 15,000 ft/s (purple).

# Line 300

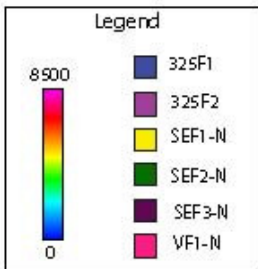
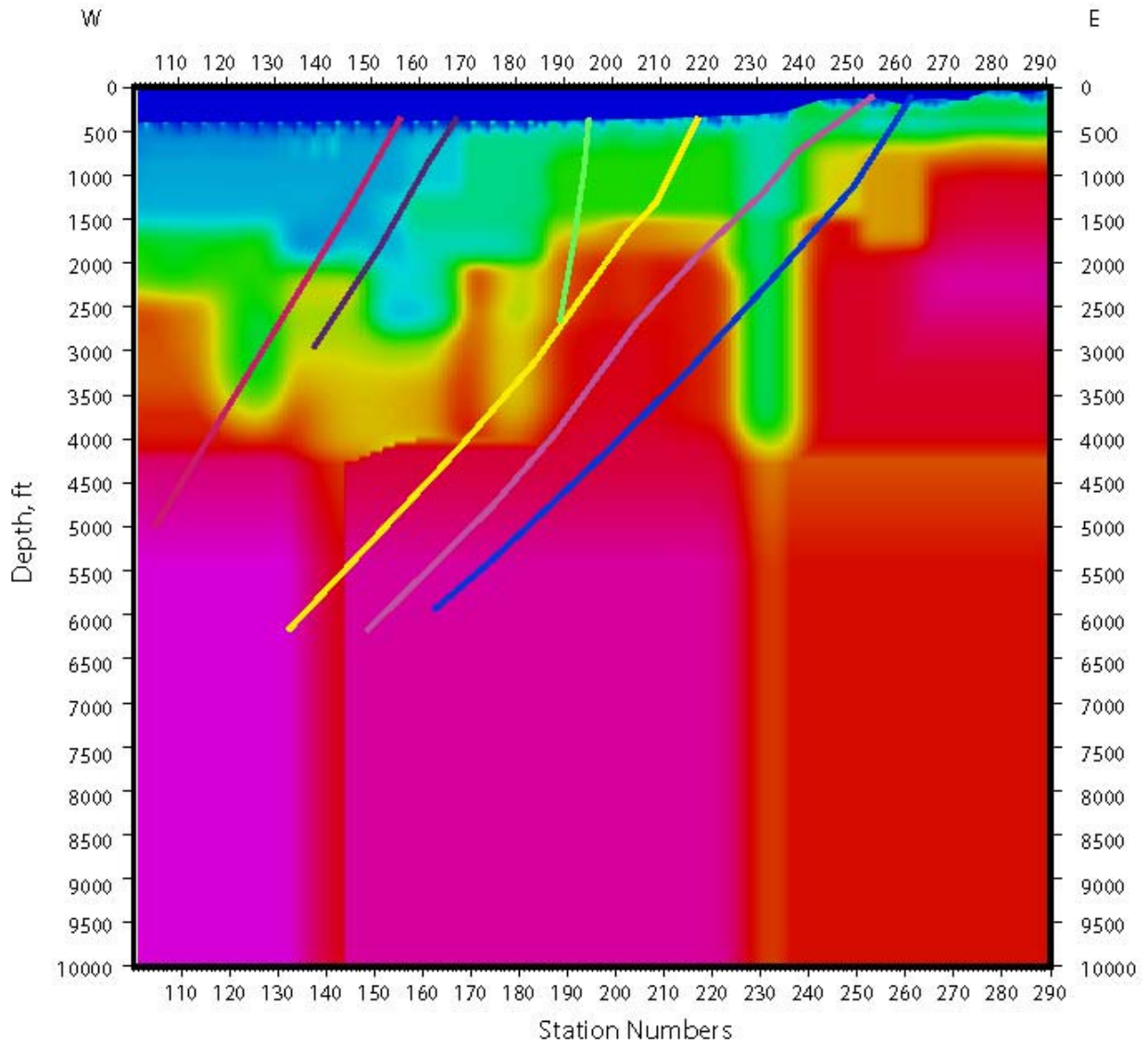


Figure 7h: S-wave velocity model along Line 3 (300) extended in depth showing the faults and discontinuities inferred by the structural team. The interpretations were made in conjunction with the P-wave velocity model (Figure 7g) and the reflection image (Figure 7i). Velocities go from 0 ft/s (blue) to 8,500 ft/s (purple).

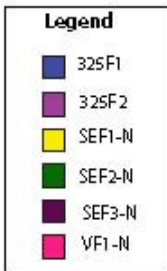
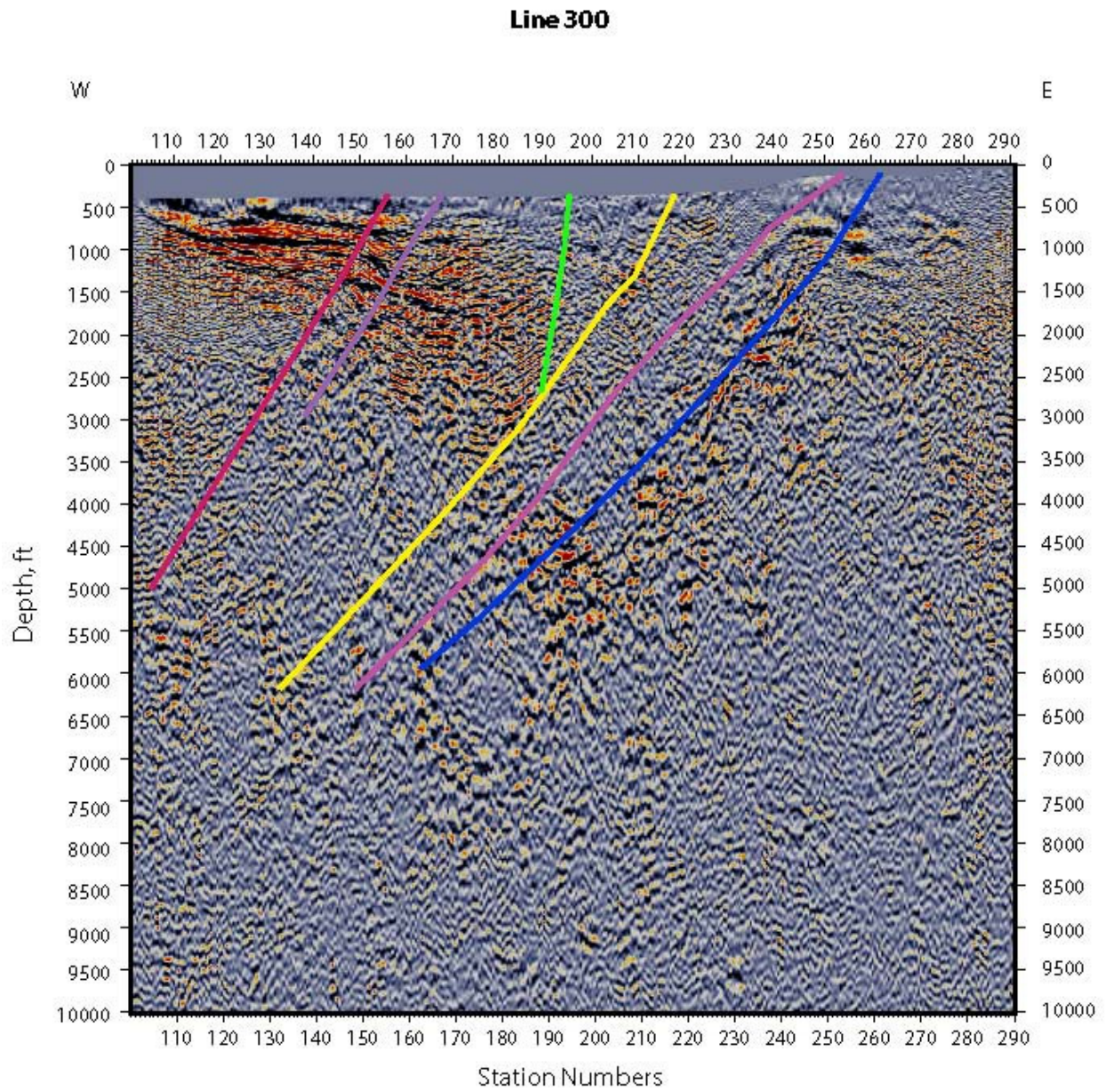


Figure 7i: P-wave depth migrated reflection image along Line 3 (300) showing the faults and discontinuities inferred by the structural team. The interpretations were made in conjunction with the P-wave velocity model (Figure 7g) and the shear-wave image (Figure 7h).

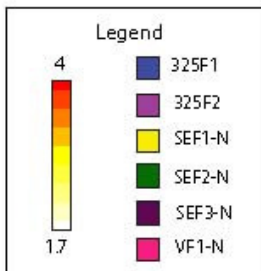
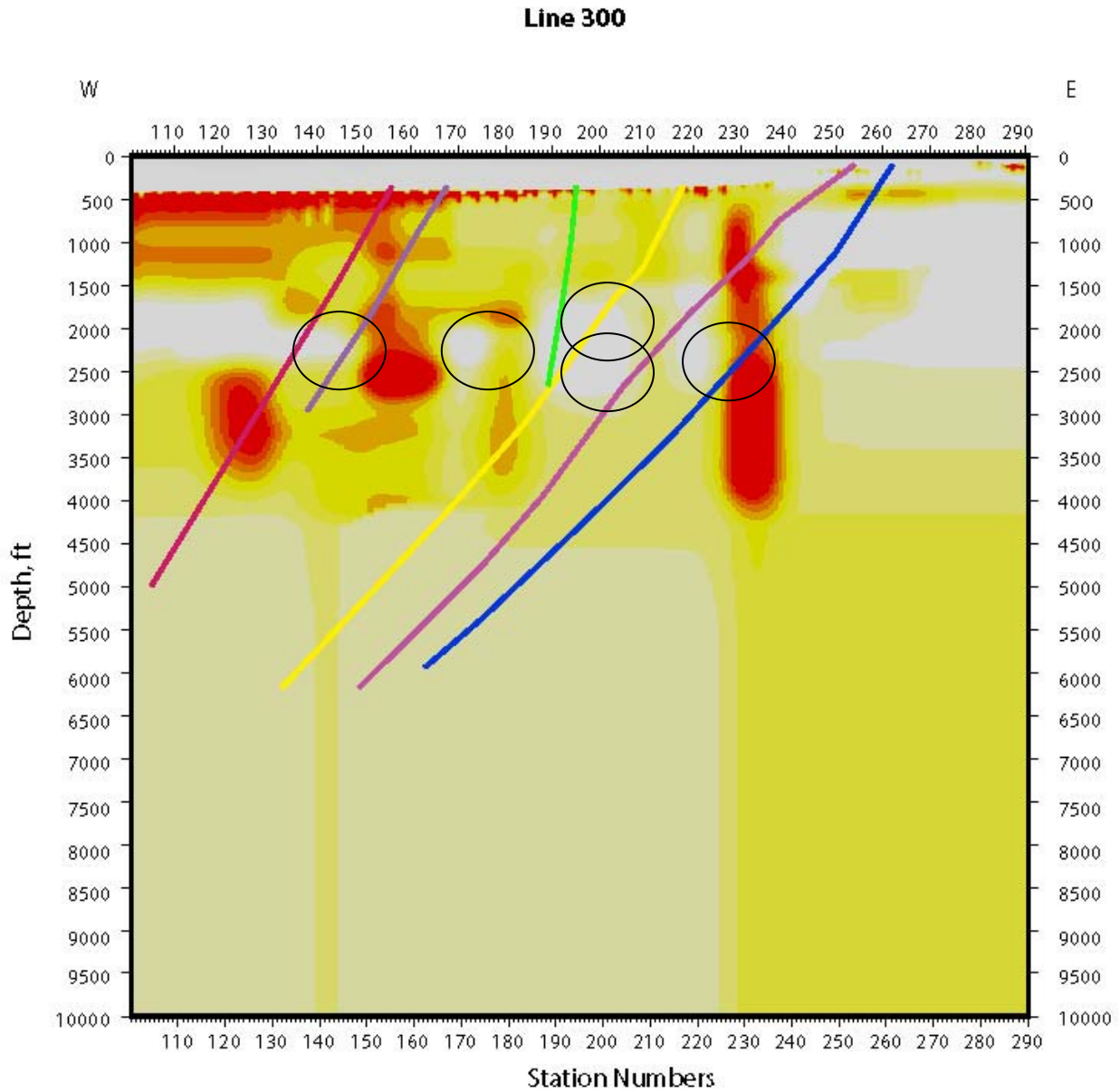


Figure 7j:  $V_p/V_s$  ratio calculated from P-wave and S-wave velocity models along Line 3 (300). The relatively lower  $V_p/V_s$  zones (circles) are potential fractured fluid filled zones.

We also calculate a  $V_p/V_s$  model from the P-wave and S-wave velocities and it is shown in Figure 7j. The low  $V_p/V_s$  zones that lie close to fault intersections and traces are marked as areas of potential fractured or fluid filled fracture zones.

#### 4.4 4.4 Line 4 (400)

Line 4, also called 400, is in the northern part of the project area, just south of Line 3 (300), and runs east-west from station number 101 in the west to 293 in the east (Figure 8a). It crosses line 10 (101) at station number 258. All of the figures represent true seismic depth sections with no vertical exaggeration.

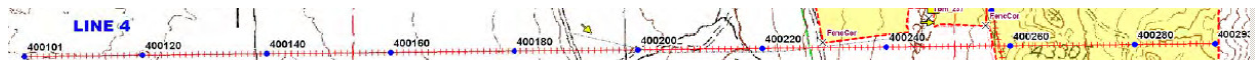


Figure 8a: Line 4 (400) runs east-west from station number 101 in the west to station number 293 in the east.

Figures 8b and 8c show a typical shot gather acquired along Line 4 using P-wave and SH-wave source, respectively. The first arrivals (shown in red) are clearly visible. These were picked and used to obtain the velocity models shown in Figures 8d and 8e, respectively.

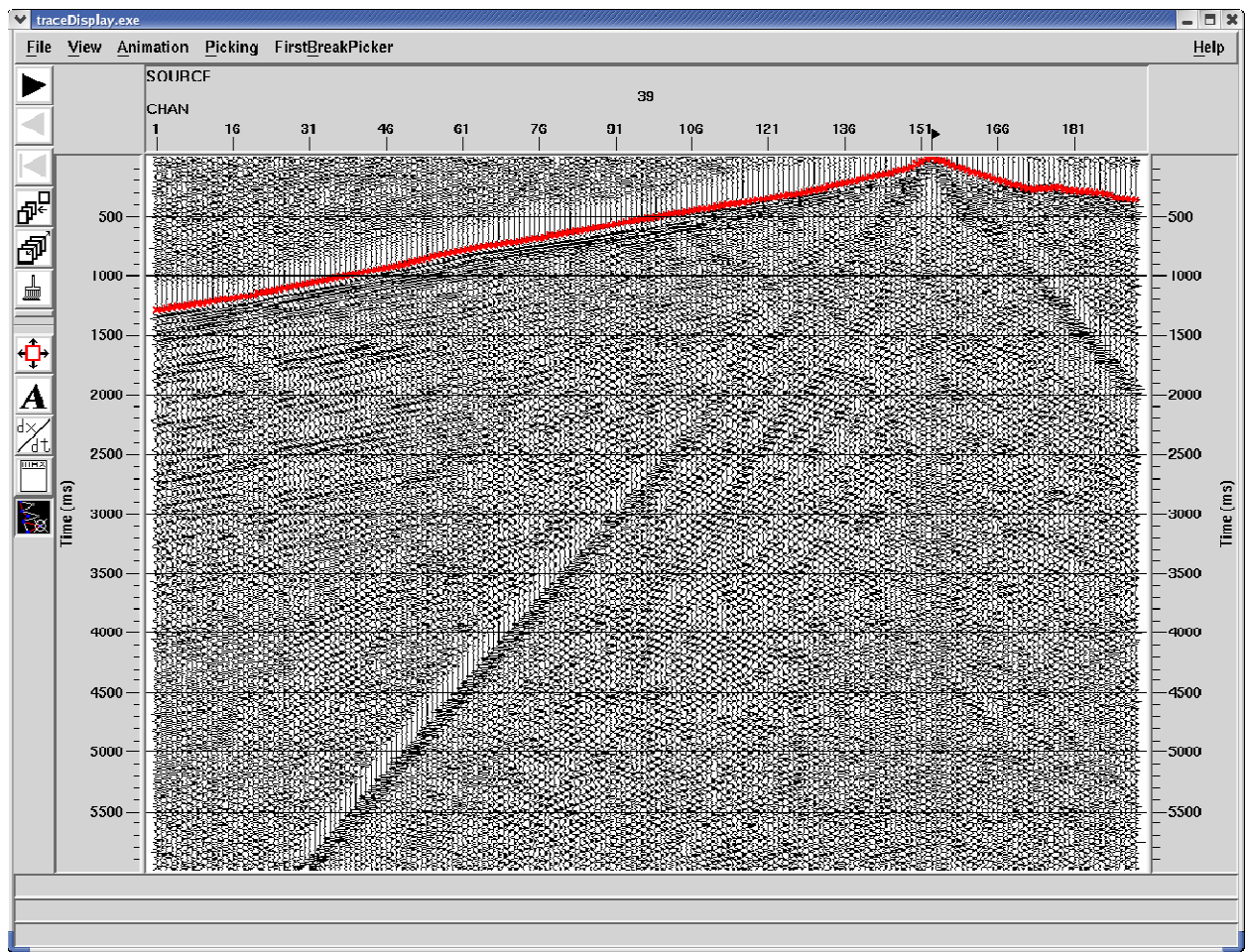


Figure 8b: Typical shot gathers from P-wave data collected along Line 4 (400). The first arrival picks, shown in red, was used to obtain the P-wave velocity model shown in Figure 8d.

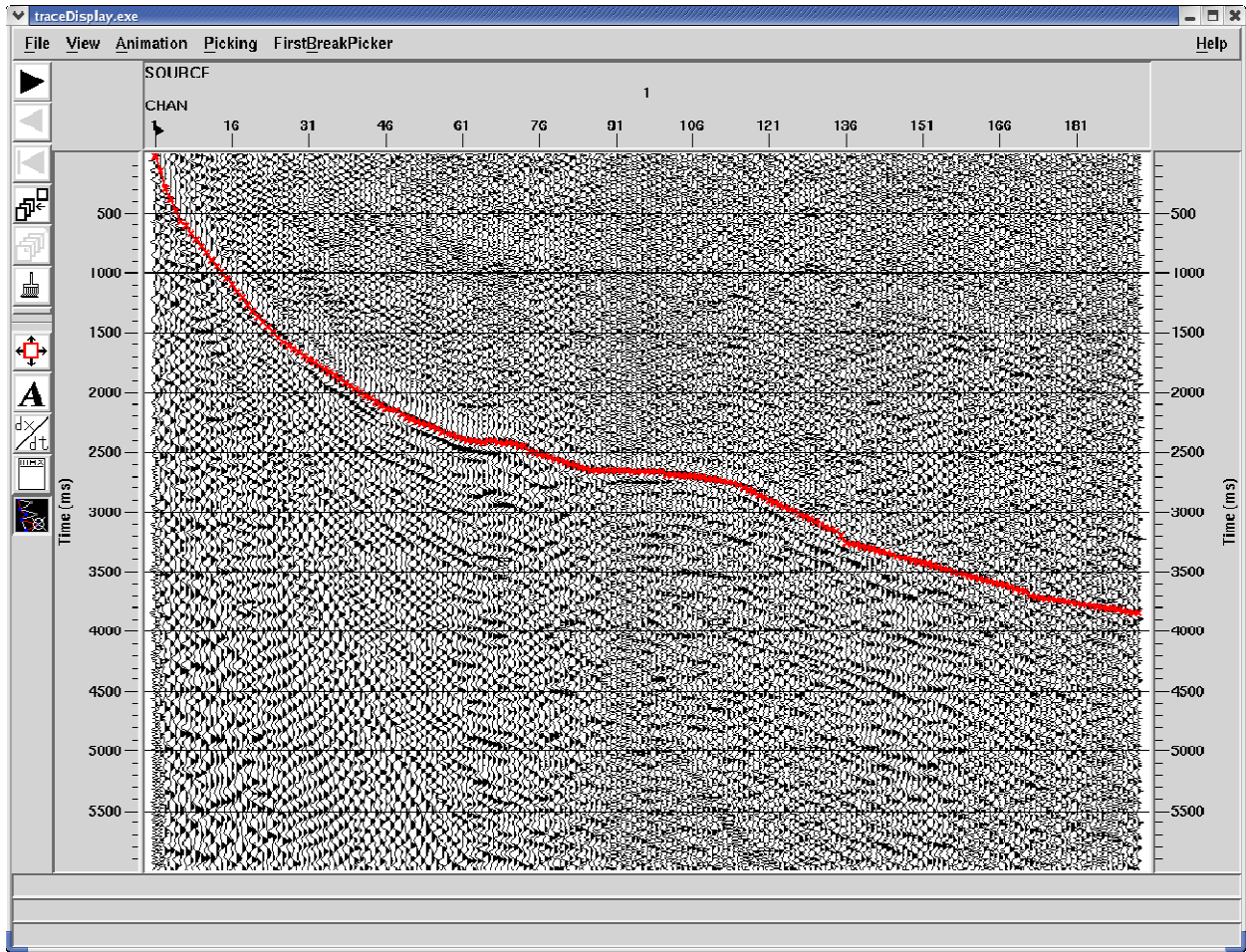


Figure 8c: Typical shot gathers from SH-wave data collected along Line 4 (400). The first arrival picks, shown in red, was used to obtain the S-wave velocity model shown in Figure 8e.

Figures 8d and 8e show the velocity model obtained from optimization of P-wave and SH-wave first arrival data (Pullammanappallil and Louie, 1994), respectively. P-wave velocities range from 1,500 ft/s to 15,000 ft/s at a depth of about 3,000 ft. High velocities in the range of 10,000 ft/s shallow towards the range front in the east. The S-wave velocities range from 500 ft/s to 10,000 ft/s. As with the P-wave velocities, the higher velocities shallow towards the east. The S-wave arrivals resolve velocities to deeper depth compared to the P-wave model. Both models show relatively low-velocity areas within the higher velocity horizons at depth. There is a distinct low velocity zone around station 200 in the P-wave model that breaks up the higher velocities.

This model is then extended in depth by interactive velocity modeling. It involved selecting an appropriate gradient that was consistent with the velocities observed along the other lines,

including the intersecting Line 10 (101). Figure 8f shows results of a P-wave depth migration (Louie and Qin, 1991) obtained using the P-wave velocity model shown in Figure 8d. Velocities are simply assumed to be a constant where there is no constraint. These are shown in Figures 8g, 8h and 8i. During the interpretation both the reflection images and the velocity model was used to identify faults and structures. Faults were inferred by direct reflections of them or by truncations of sub-horizontal reflections. The naming convention was developed by Greg Rhodes.

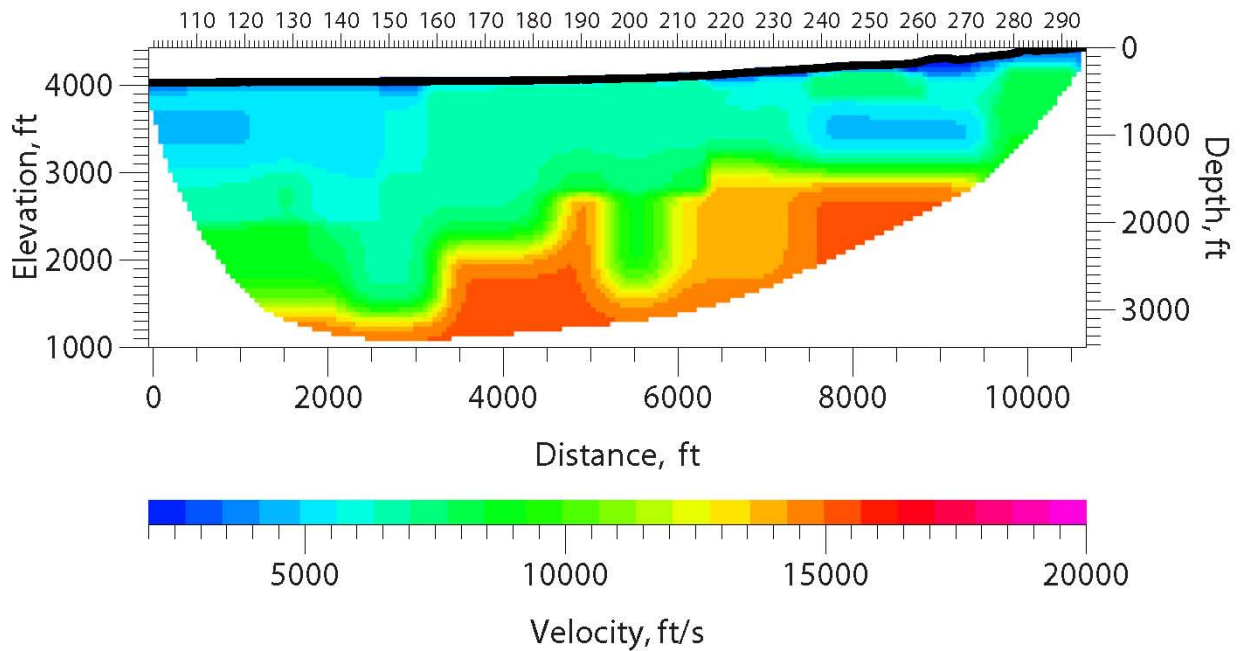


Figure 8d: P-wave velocity model along Line 4 (400) obtained from optimization of P-wave first-arrival travel times.

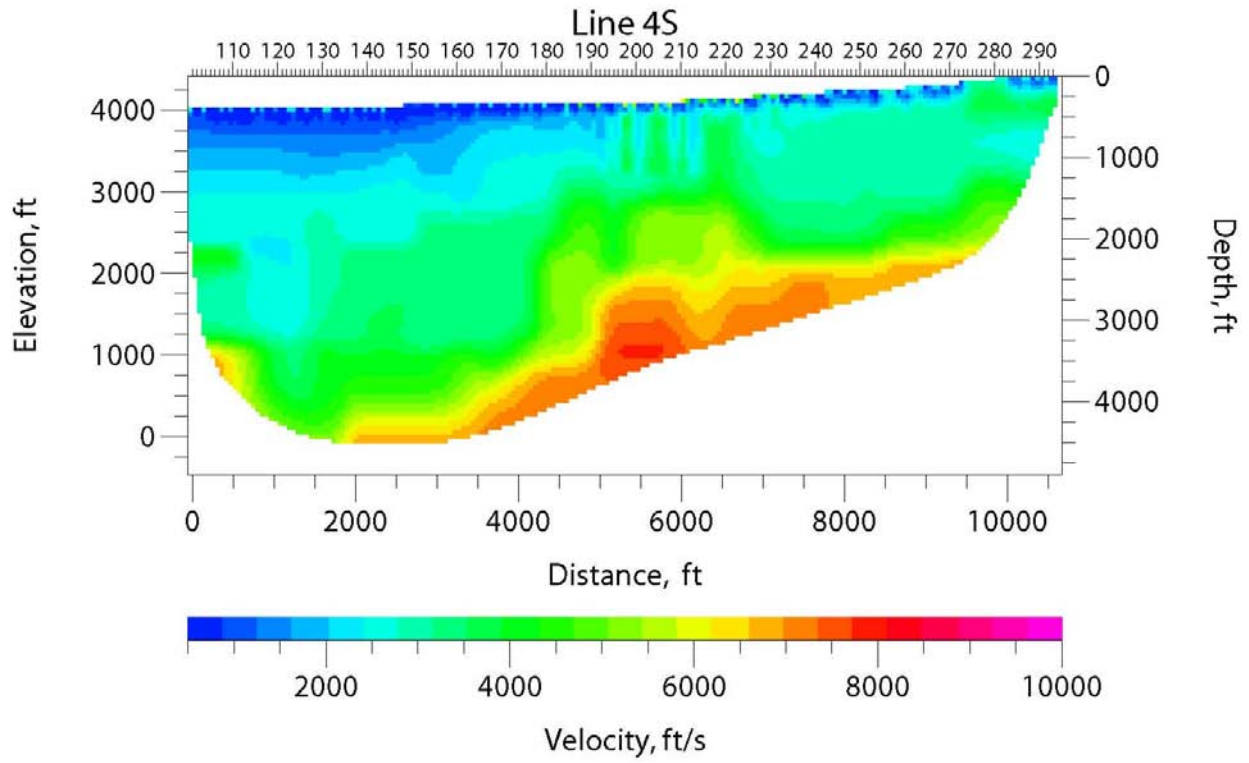


Figure 8e: S-wave velocity model along Line 4 (400) obtained from optimization of SH-wave first-arrival travel times.

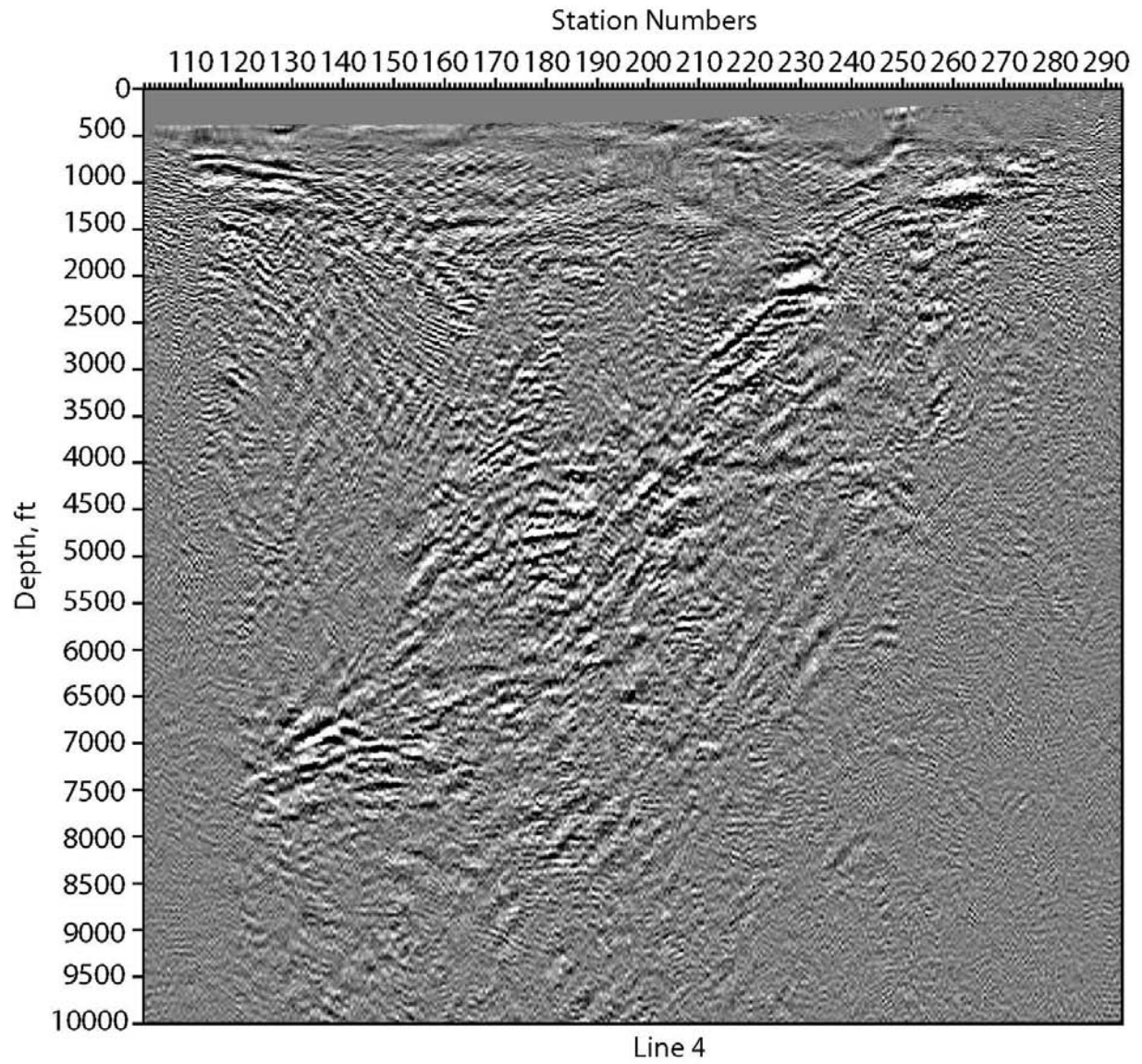


Figure 8f: Depth-migrated image along Line 4 (400) using the velocity model shown in Figure 8g.

### Line 400

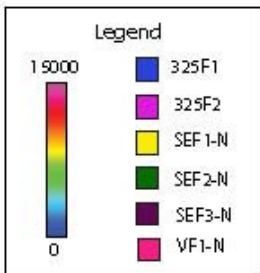
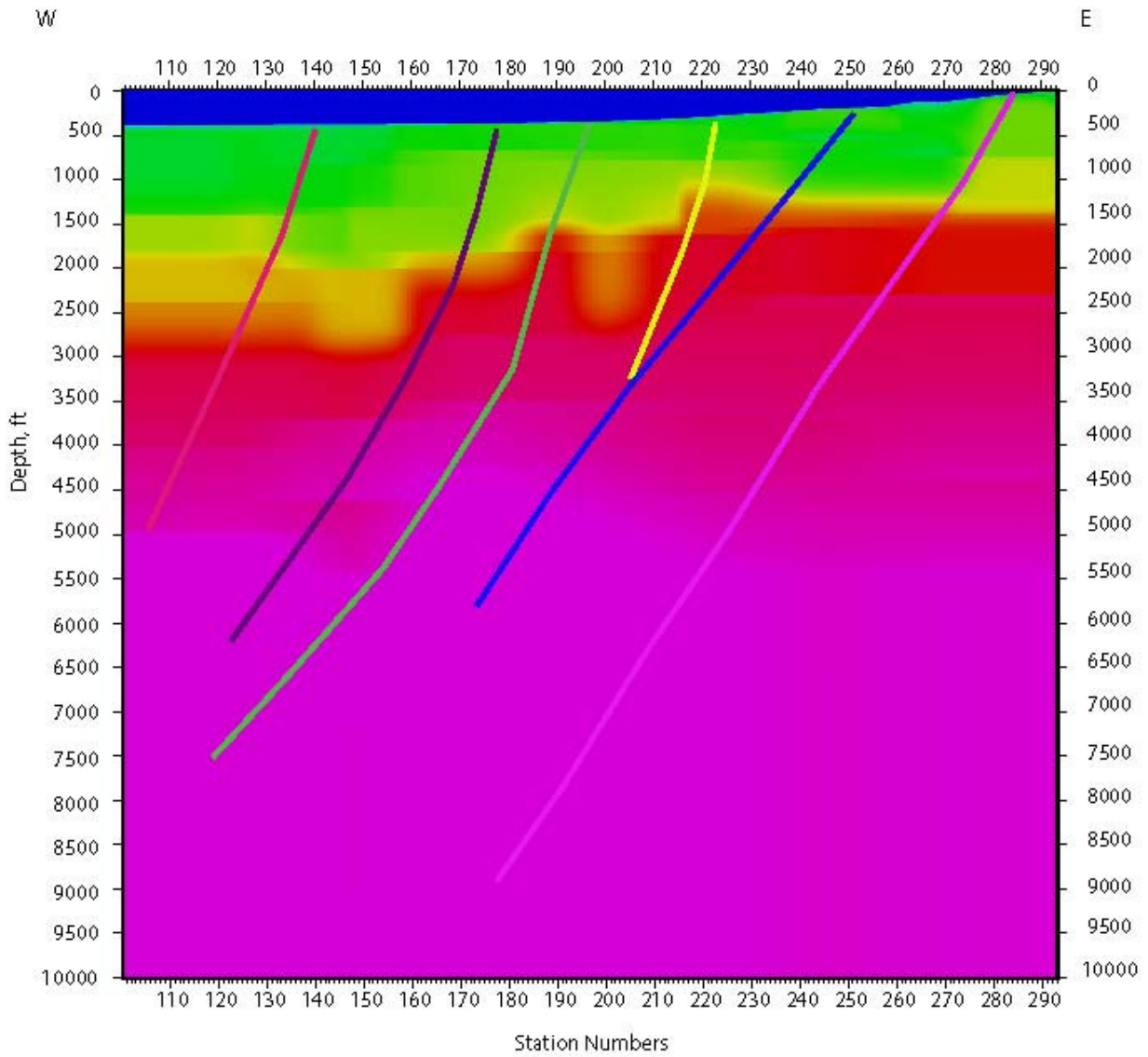


Figure 8g: P-wave velocity model along Line 4 (400) extended in depth. The interpretations were made in conjunction with the shear-wave velocity model (Figure 8h) and the P-wave reflection image (Figure 8i). Velocities go from 0 ft/s (blue) to 15,000 ft/s (purple).

### Line 400

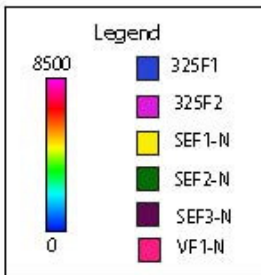
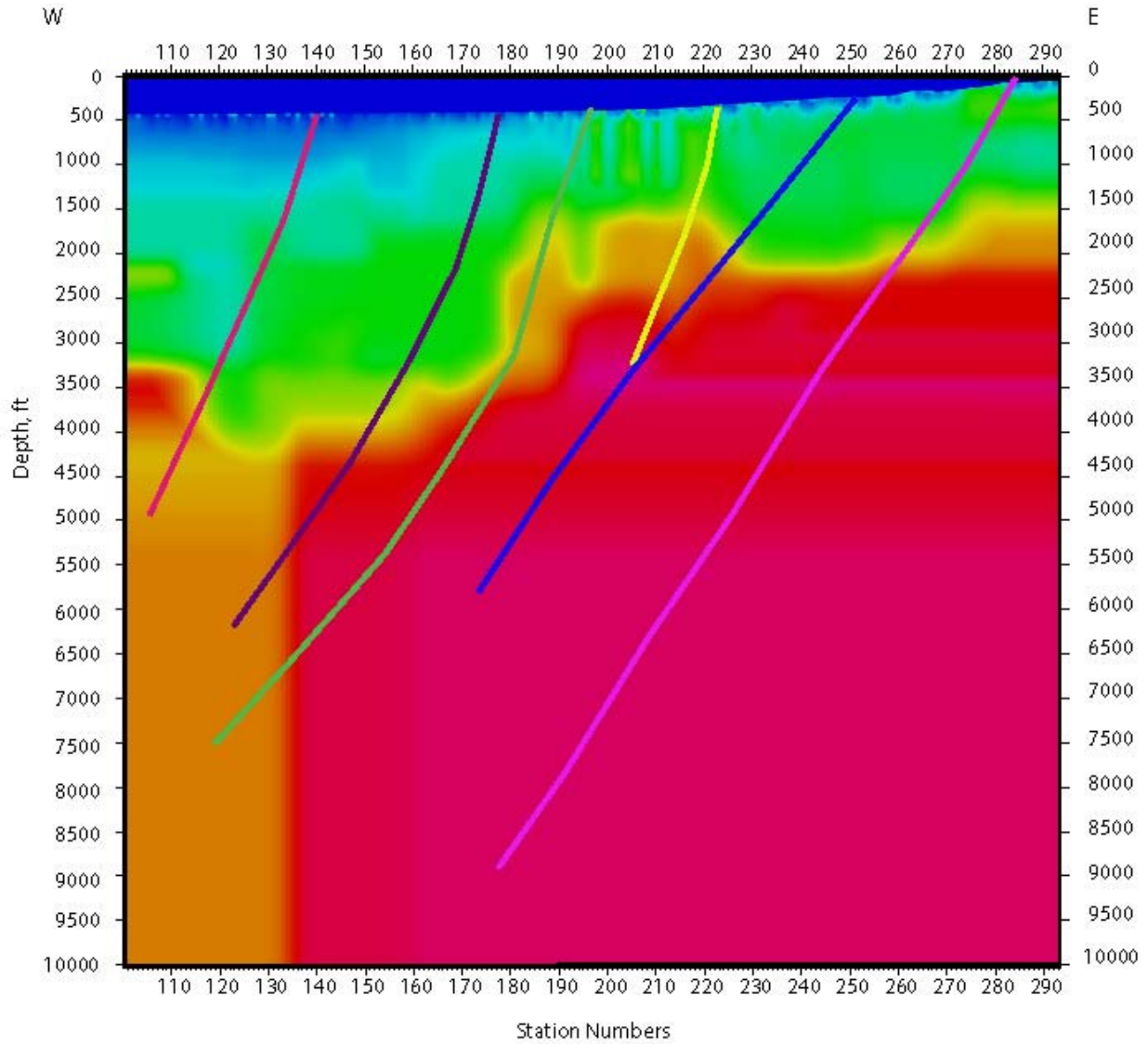


Figure 8h: S-wave velocity model along Line 4 (400) extended in depth showing the faults and discontinuities inferred by the structural team. The interpretations were made in conjunction with the P-wave velocity model (Figure 8g) and the reflection image (Figure 8i). Velocities go from 0 ft/s (blue) to 8,500 ft/s (purple).

# Line 400

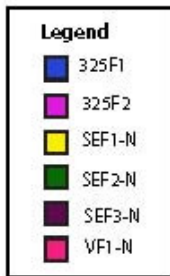
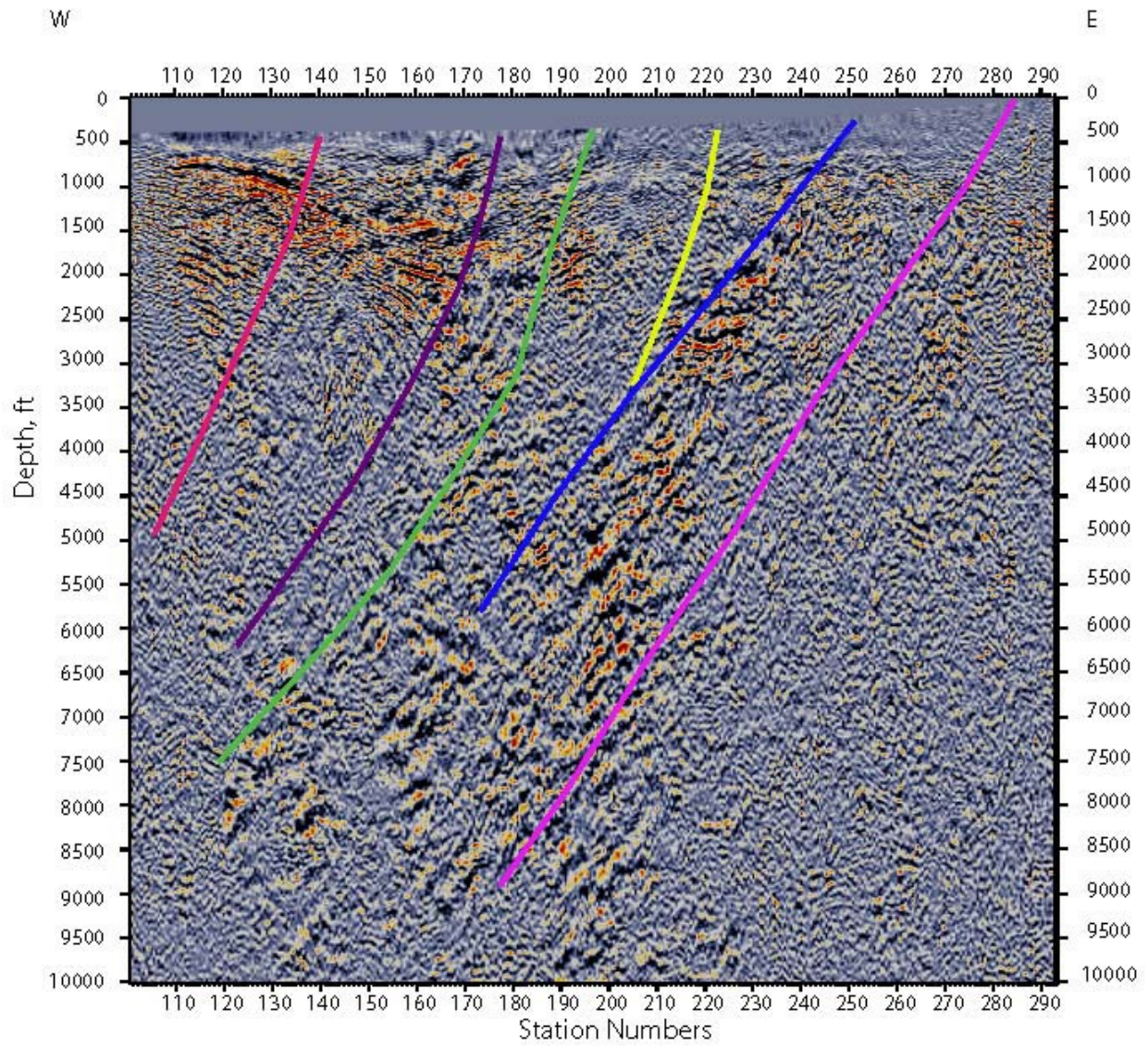


Figure 8i: P-wave depth migrated reflection image along Line 4 (400) showing the faults and discontinuities inferred by the structural team. The interpretations were made in conjunction with the P-wave velocity model (Figure 8g) and the shear-wave image (Figure 8h).

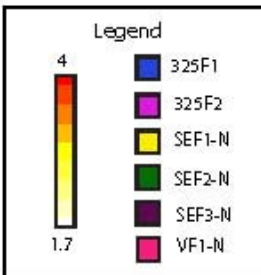
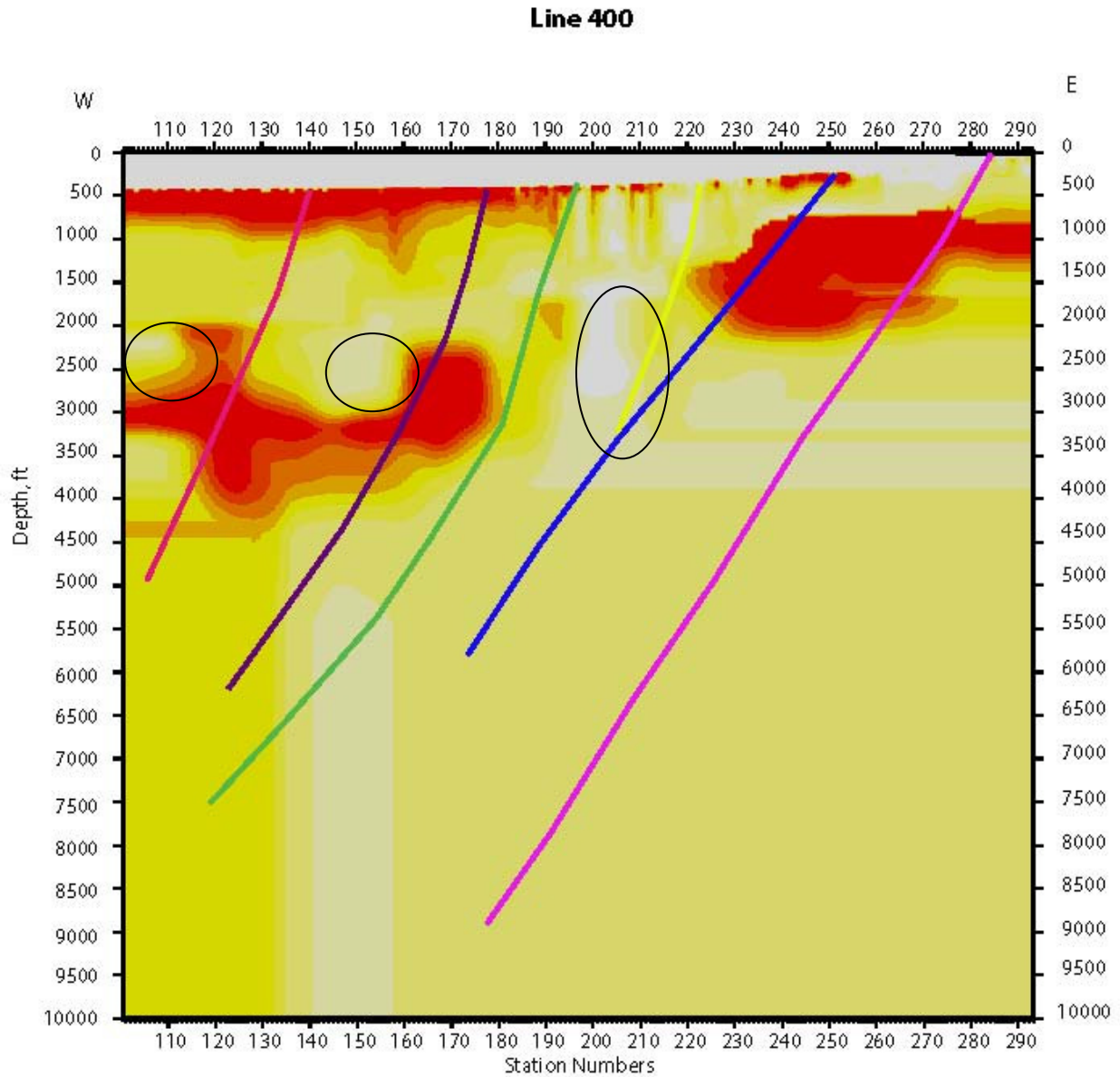


Figure 8j:  $V_p/V_s$  ratio calculated from P-wave and S-wave velocity models along Line 4 (400). The relatively lower  $V_p/V_s$  zones (circles) are potential fractured fluid filled zones.

We also calculate a  $V_p/V_s$  model from the P-wave and S-wave velocities and it is shown in Figure 8j. The low  $V_p/V_s$  zones that lie close to fault intersections and traces are marked as areas of potential fractured or fluid filled fracture zones.

#### **4.5 4.5 Line10 (101)**

Line10, also called 101, is the in the northern part of the project area and runs north-south from station number 101 in the north to 293 in the south (Figure 9a). It was acquired to map any faults that might be striking in the east-west direction. All of the figures represent true seismic depth sections with no vertical exaggeration.



Figure 9a: Line 10 (101) runs east-west from station number 101 in the north to station number 293 in the south.

Figure 9b shows a typical shot gather acquired along Line 4 using P-wave source. We couldn't get any good data from the S-wave source, probably due to the site conditions created by the mine workings. The first arrivals (shown in red) are clearly visible in the P-wave though and these were picked and used to obtain the velocity models shown in Figures 9c.

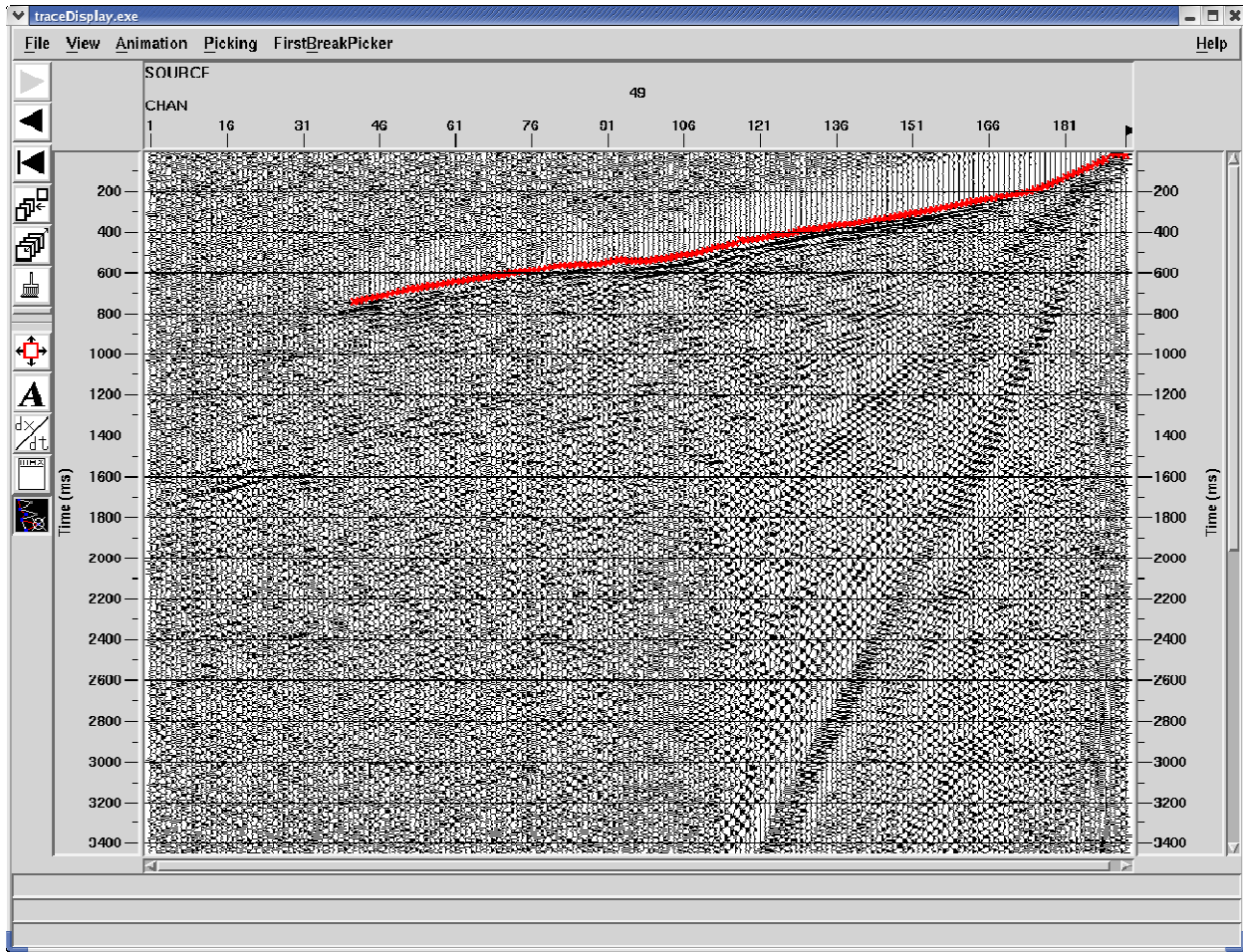


Figure 9b: Typical shot gathers from P-wave data collected along Line 10 (101). The first arrival picks, shown in red, was used to obtain the P-wave velocity model shown in Figure 9c.

Figure 9c shows the P-wave velocity model obtained from optimization of first arrivals. P-wave velocities range from 1,500 ft/s to 20,000 ft/s at a depth of about 2,000 feet. Relatively higher velocities are encountered along this line due to the fact that it is location along the range front. Lateral velocity variations are observed within the high velocity zone, for example, around station 160 and station 220 which might indicate presence of cross cutting features.

This model is then extended in depth by interactive velocity modeling. It involved selecting an appropriate gradient that was consistent with the velocities observed along the other lines, including the intersecting lines 1, 2, 3 and 4. Figure 9d shows results of a P-wave depth migration (Louie and Qin, 1991) obtained using the P-wave velocity model shown in Figure 9c. Velocities are simply assumed to be a constant where there is no constraint. During the interpretation both the reflection images and the velocity model was used to identify faults and

structures. Faults were inferred by direct reflections of them or by truncations of sub-horizontal reflections. The naming convention was developed by Greg Rhodes.

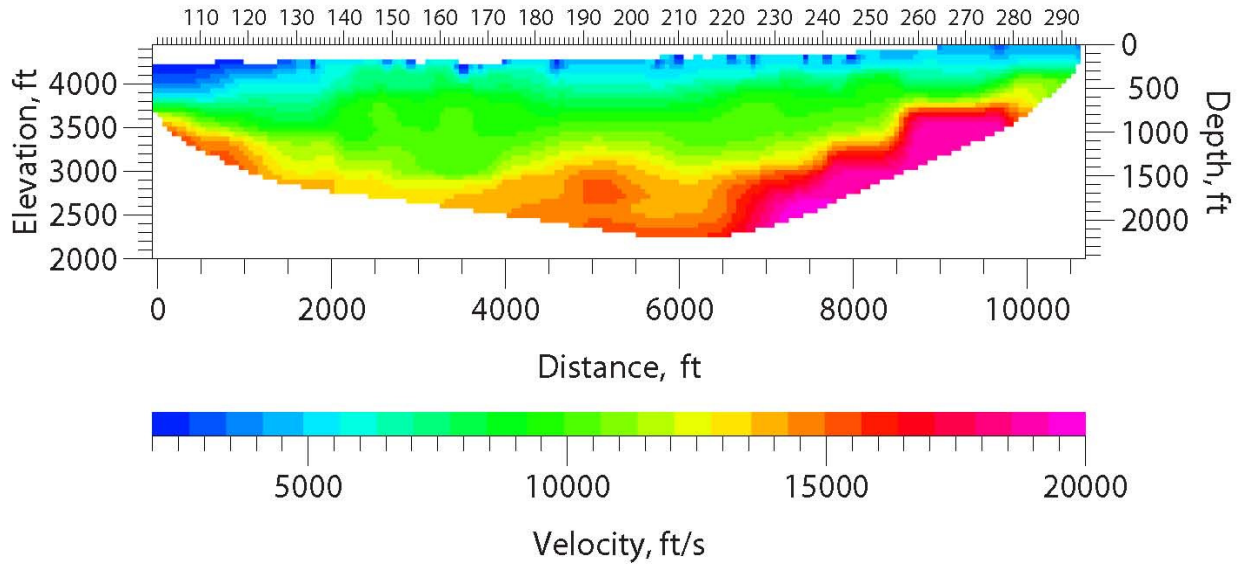


Figure 9c: P-wave velocity model along Line 10 (101) obtained from optimization of P-wave first-arrival travel times.

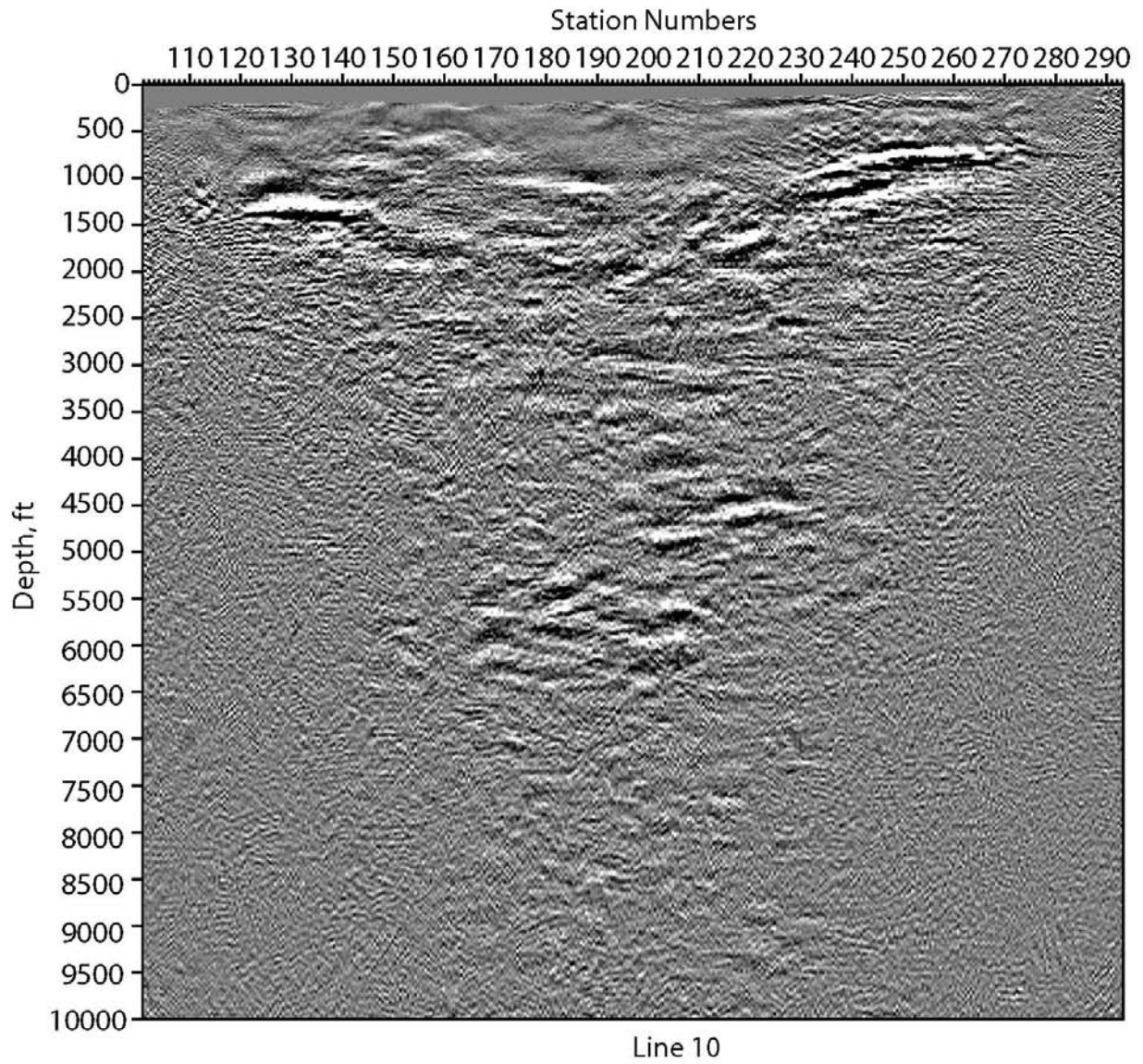


Figure 9d: Depth-migrated image along Line 10 (101) using the velocity model shown in Figure 9e.

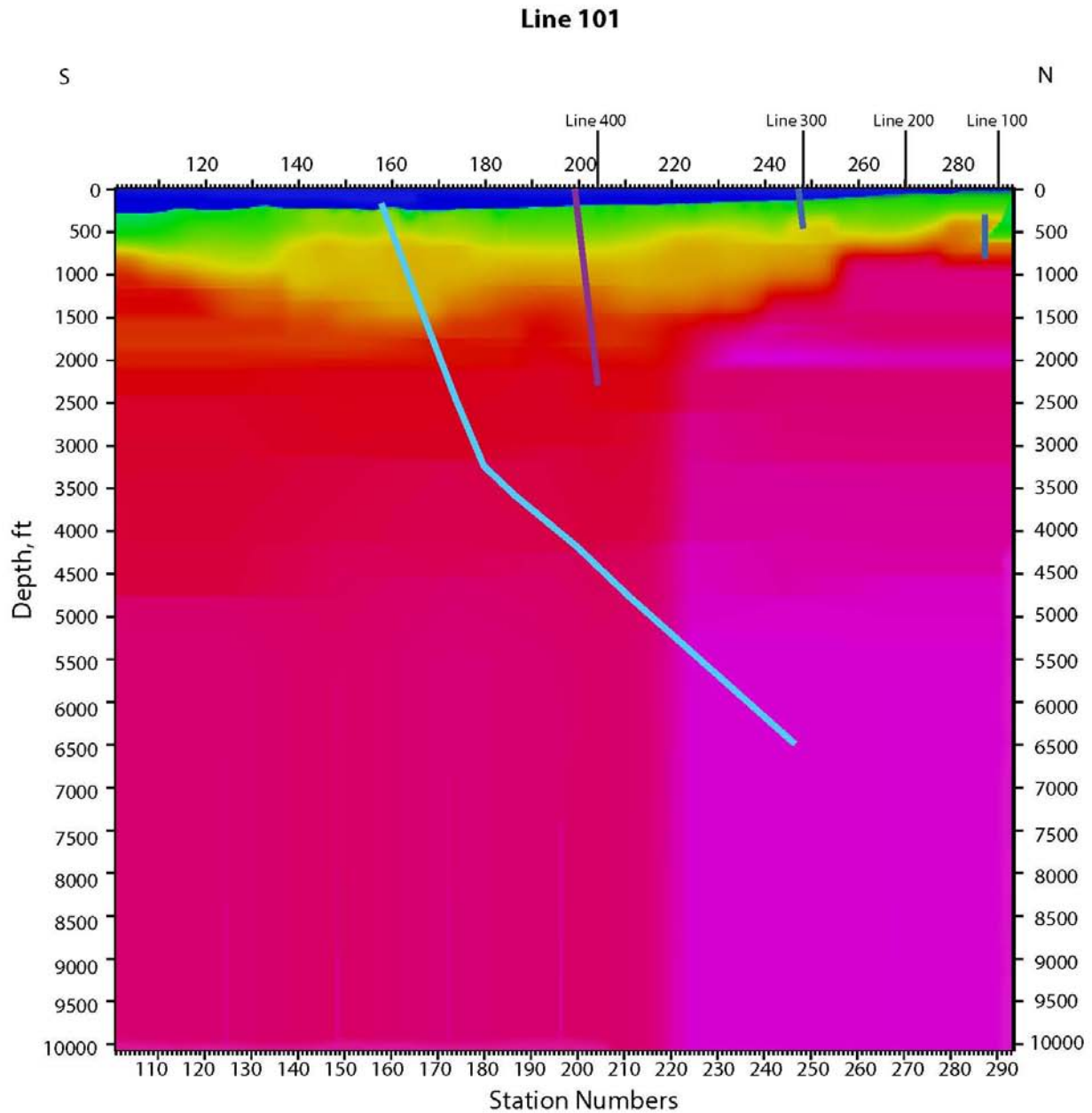


Figure 9d: P-wave velocity model along Line 10 (101) extended in depth. Velocities go from 0 ft/s (blue) to 15,000 ft/s (purple). The faults shown are interpreted in conjunction with the reflection image shown in Figure 9e.

### Line 101

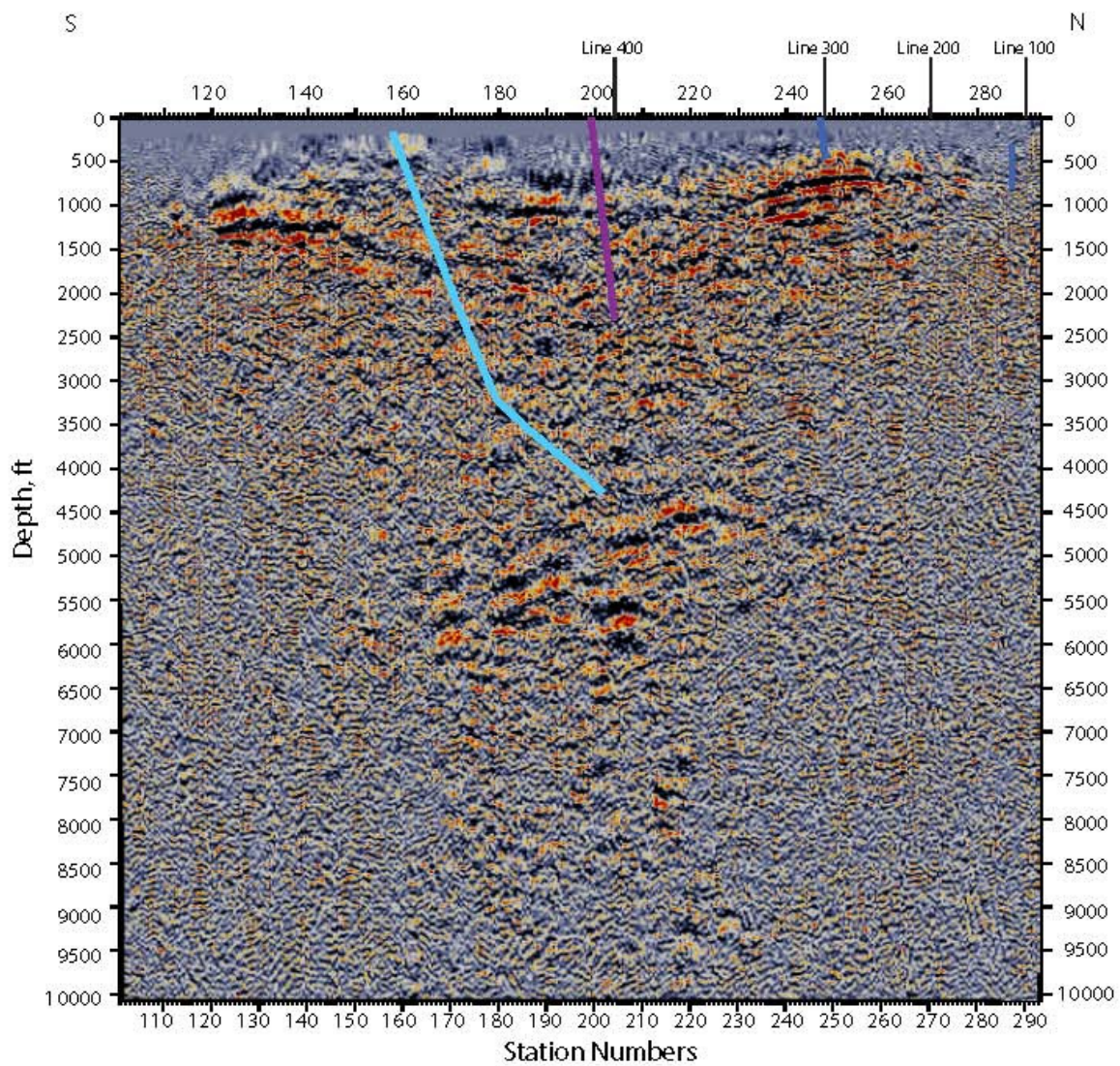


Figure 9e: P-wave depth migrated reflection image along Line 10 (101) showing the faults and discontinuities inferred by the structural team. The interpretations were made in conjunction with the P-wave velocity model (Figure 9d).

#### 4.6 4.6 Line 5 (500)

Line 5, also called 500, is the northernmost line in the southern part of the project area and runs east-west from station number 101 in the west to 293 in the east (Figure 10a). It is close to three existing wells, Kosmos 1-8, Kosmos 1-9 and SE-2. All of the figures represent true seismic depth sections with no vertical exaggeration.

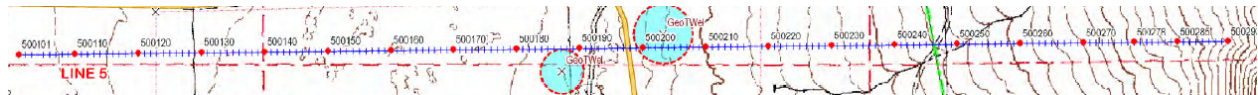


Figure 10a: Line 5 (500) runs east-west from station number 101 in the west to station number 293 in the east.

Figures 10b and 10c show a typical shot gather acquired along Line 5 using P-wave and SH-wave source, respectively. The first arrivals (shown in red) are clearly visible. These were picked and used to obtain the velocity models shown in Figures 10d and 10e, respectively.

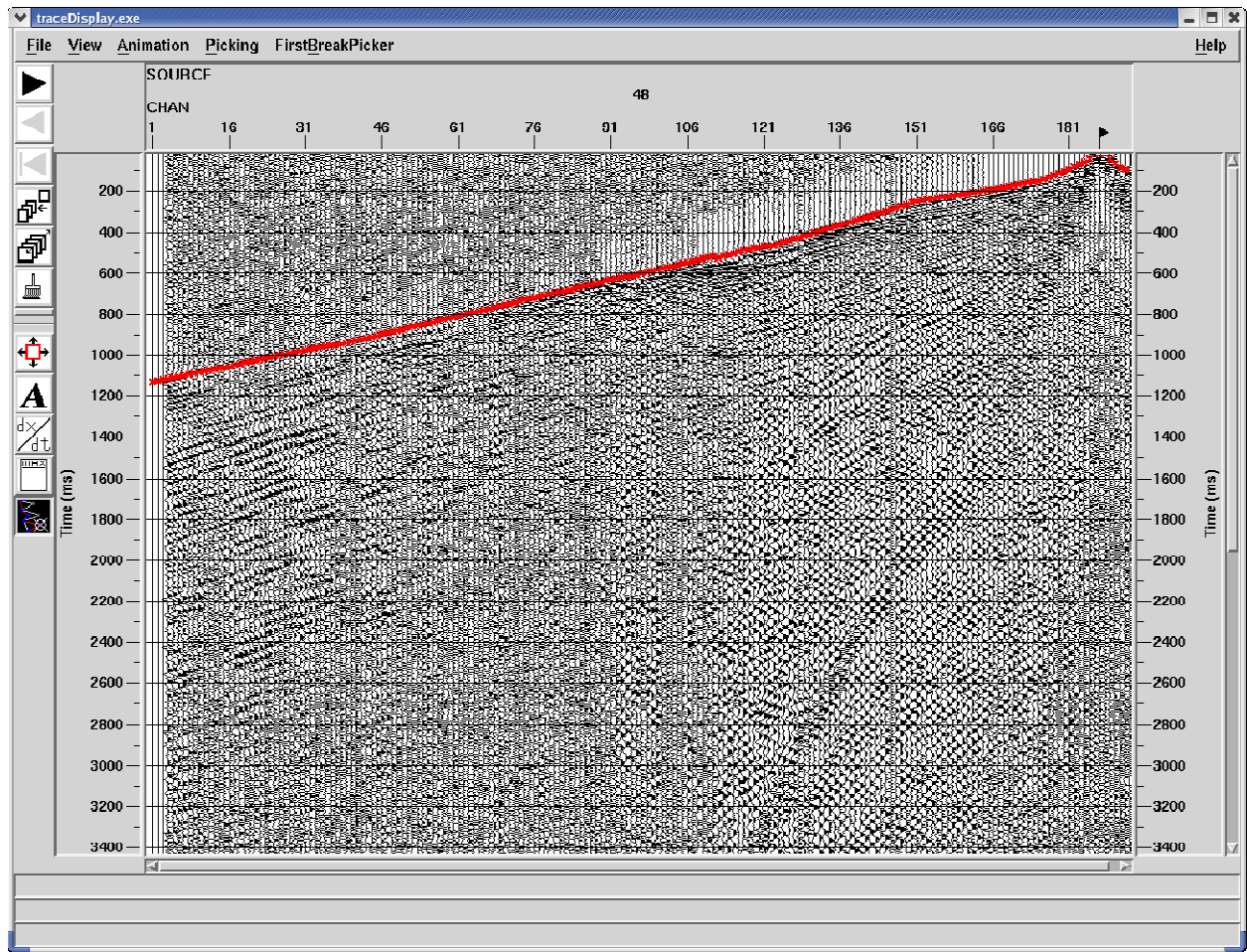


Figure 10b: Typical shot gathers from P-wave data collected along Line 5 (500). The first arrival picks, shown in red, was used to obtain the P-wave velocity model shown in Figure 10d.

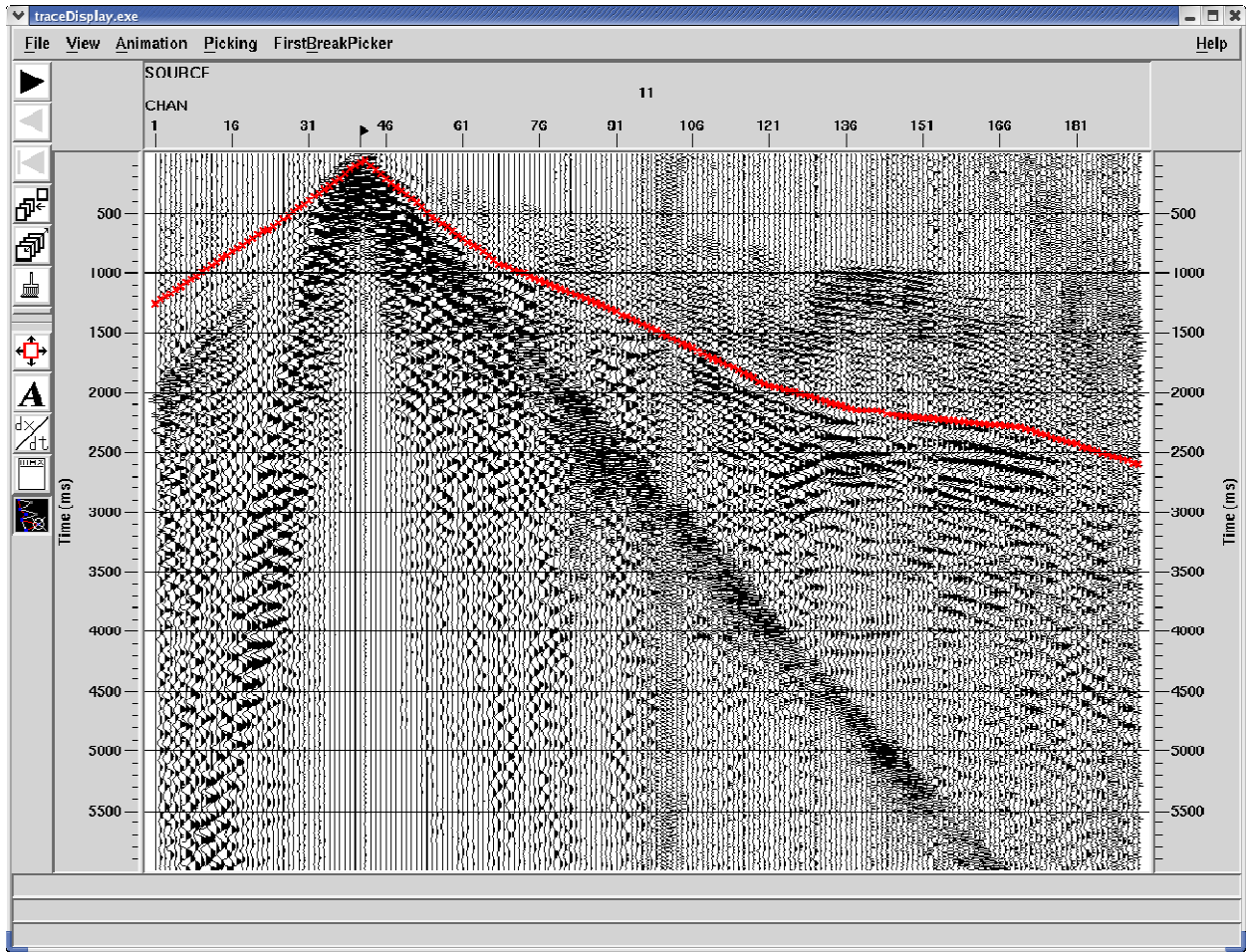


Figure 10c: Typical shot gathers from SH-wave data collected along Line 5 (500). The first arrival picks, shown in red, was used to obtain the S-wave velocity model shown in Figure 10e.

Figures 10d and 10e show the velocity model obtained from optimization of P-wave and SH-wave first arrival data (Pullammanappallil and Louie, 1994), respectively. P-wave velocities range from 1,500 ft/s to 15,000 ft/s at a depth of about 4,000 ft. High velocities in the range of 15,000 ft/s shallow towards the range front in the east. Since the seismic line goes well into the ranges, the higher velocities appear shallower in the east compared to the northern lines. The S-wave velocities range from 500 ft/s to 10,000 ft/s. As with the P-wave velocities, the higher velocities shallow towards the east. There is a distinct lateral change in velocities around station 230 and relatively low velocities around station 180.

This model is then extended in depth by interactive velocity modeling. It involved selecting an appropriate gradient that was consistent with the velocities observed along the other lines. Figure 10f shows results of a P-wave depth migration (Louie and Qin, 1991) obtained using the

P-wave velocity model shown in Figure 10d. Interpretations of the velocity and reflection images are shown in Figures 10g, 10h, and 10i. During the interpretation both the reflection images and the velocity model was used to identify faults and structures. Faults were inferred by direct reflections of them or by truncations of sub-horizontal reflections. The naming convention was developed by Greg Rhodes.

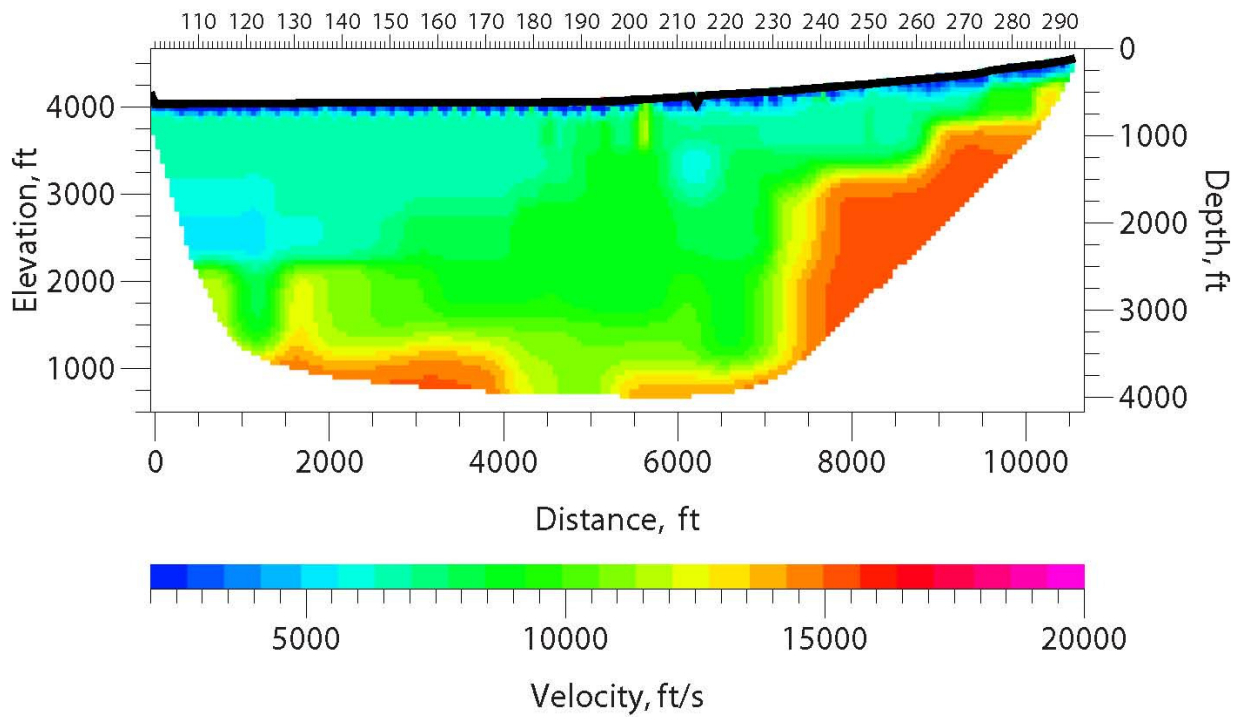


Figure 10d: P-wave velocity model along Line 5 (500) obtained from optimization of P-wave first-arrival travel times.

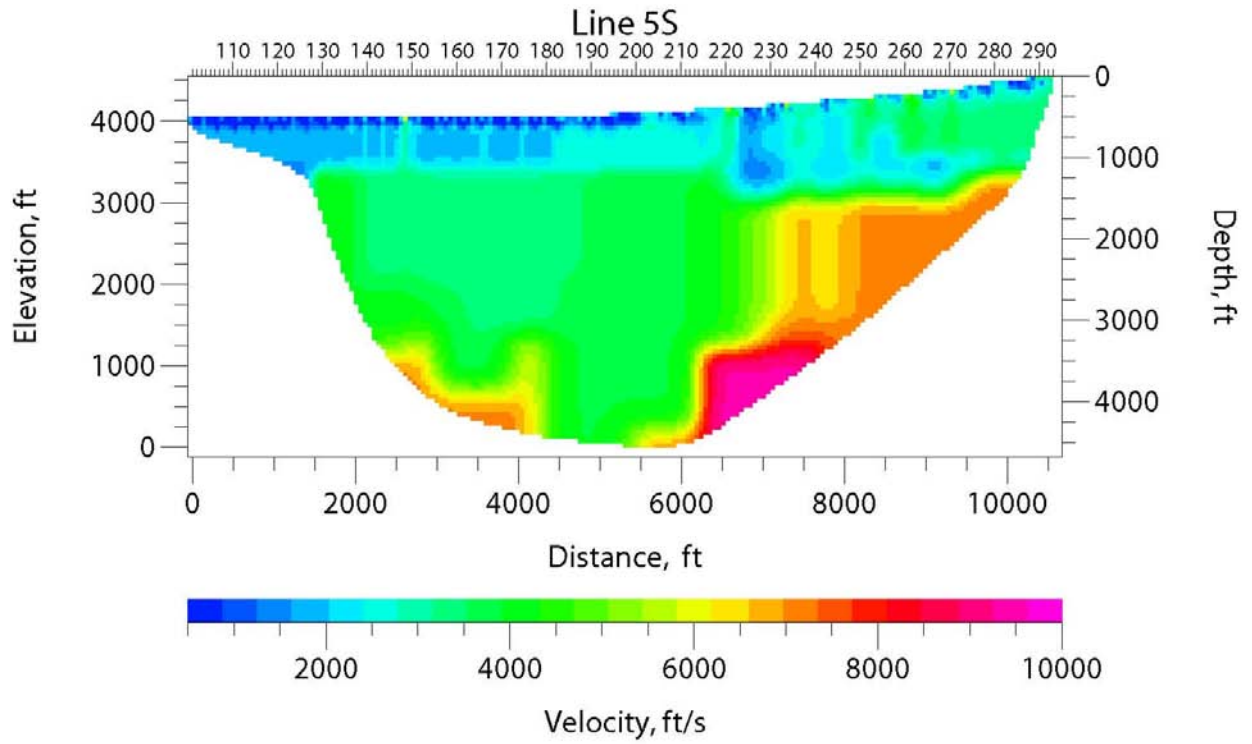


Figure 10e: S-wave velocity model along Line 5 (500) obtained from optimization of SH-wave first-arrival travel times.

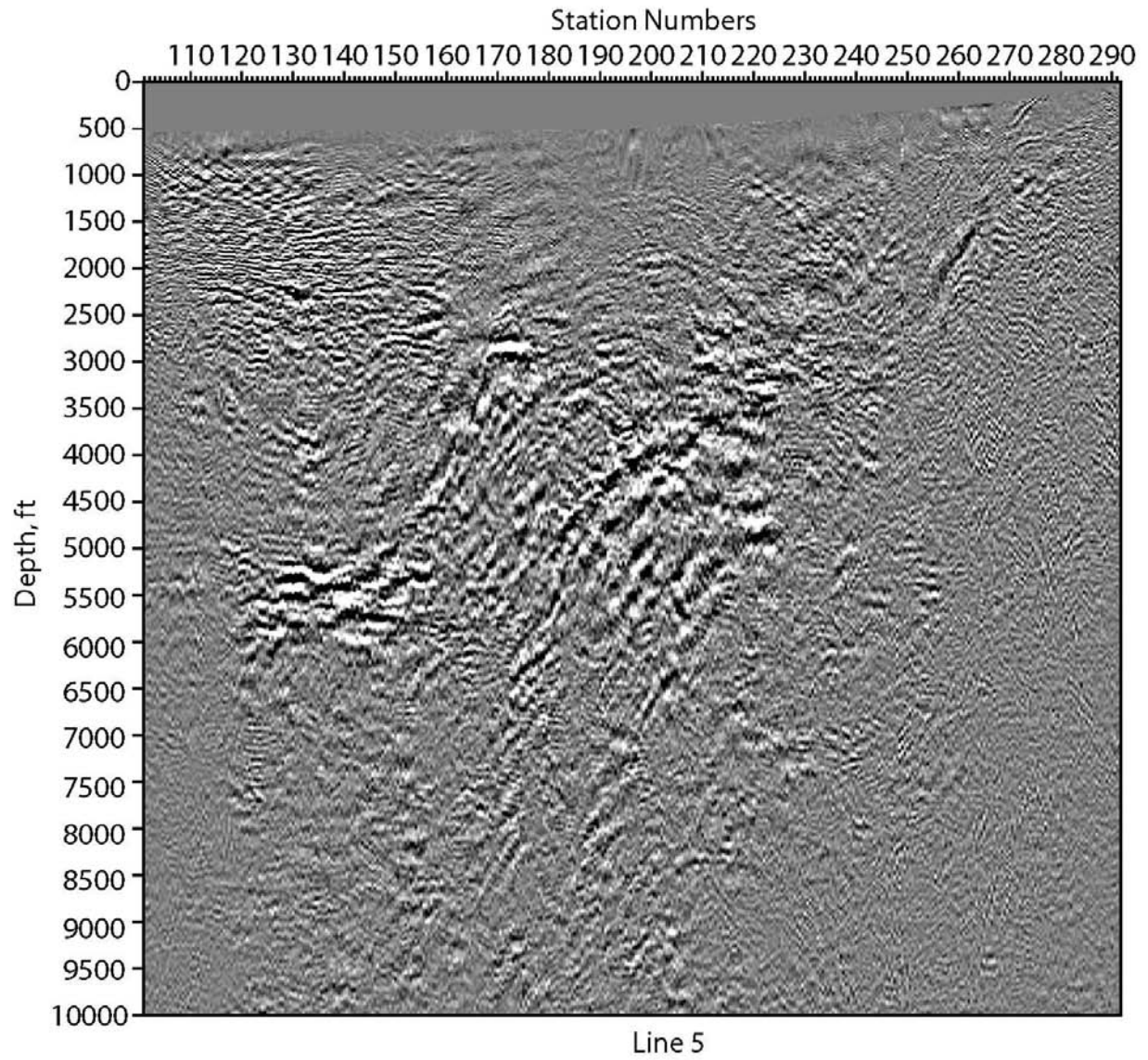


Figure 10f: Depth-migrated image along Line 5 (500) using the velocity model shown in Figure 10g.

### Line 500

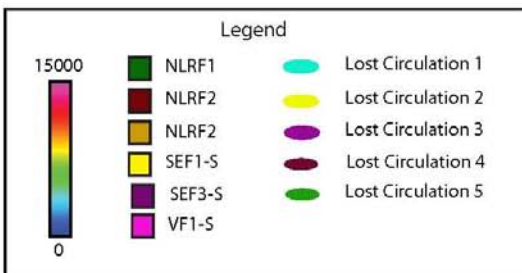
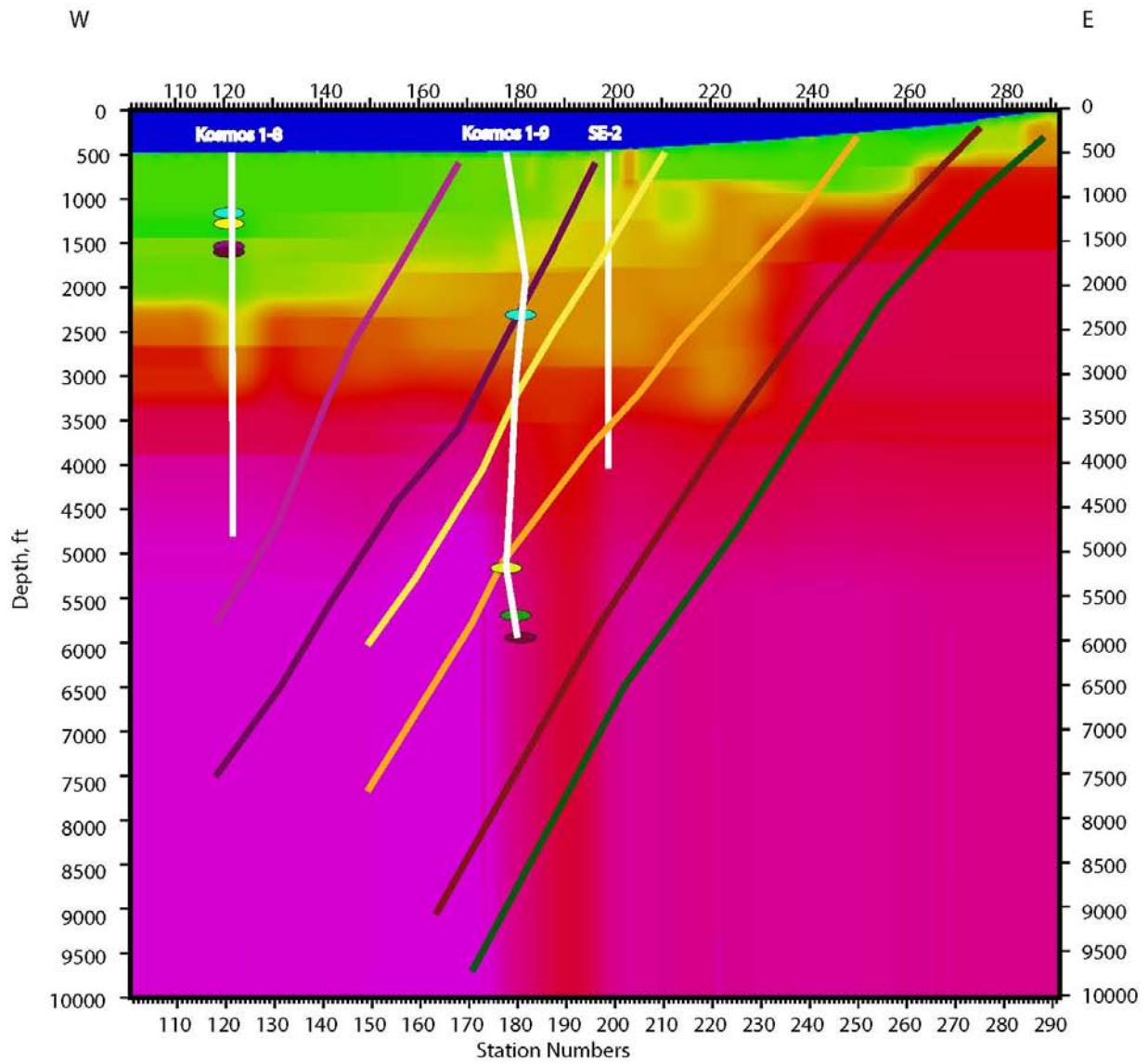


Figure 10g: P-wave velocity model along Line 5 (500) extended in depth. The interpretations were made in conjunction with the shear-wave velocity model (Figure 10h) and the P-wave reflection image (Figure 10i). Velocities go from 0 ft/s (blue) to 15,000 ft/s (purple).

# Line 500

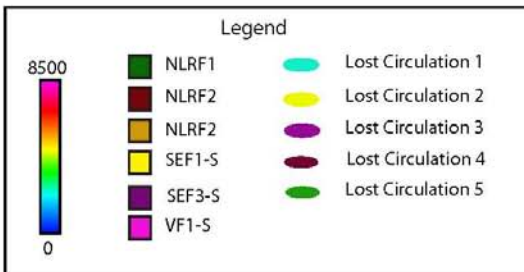
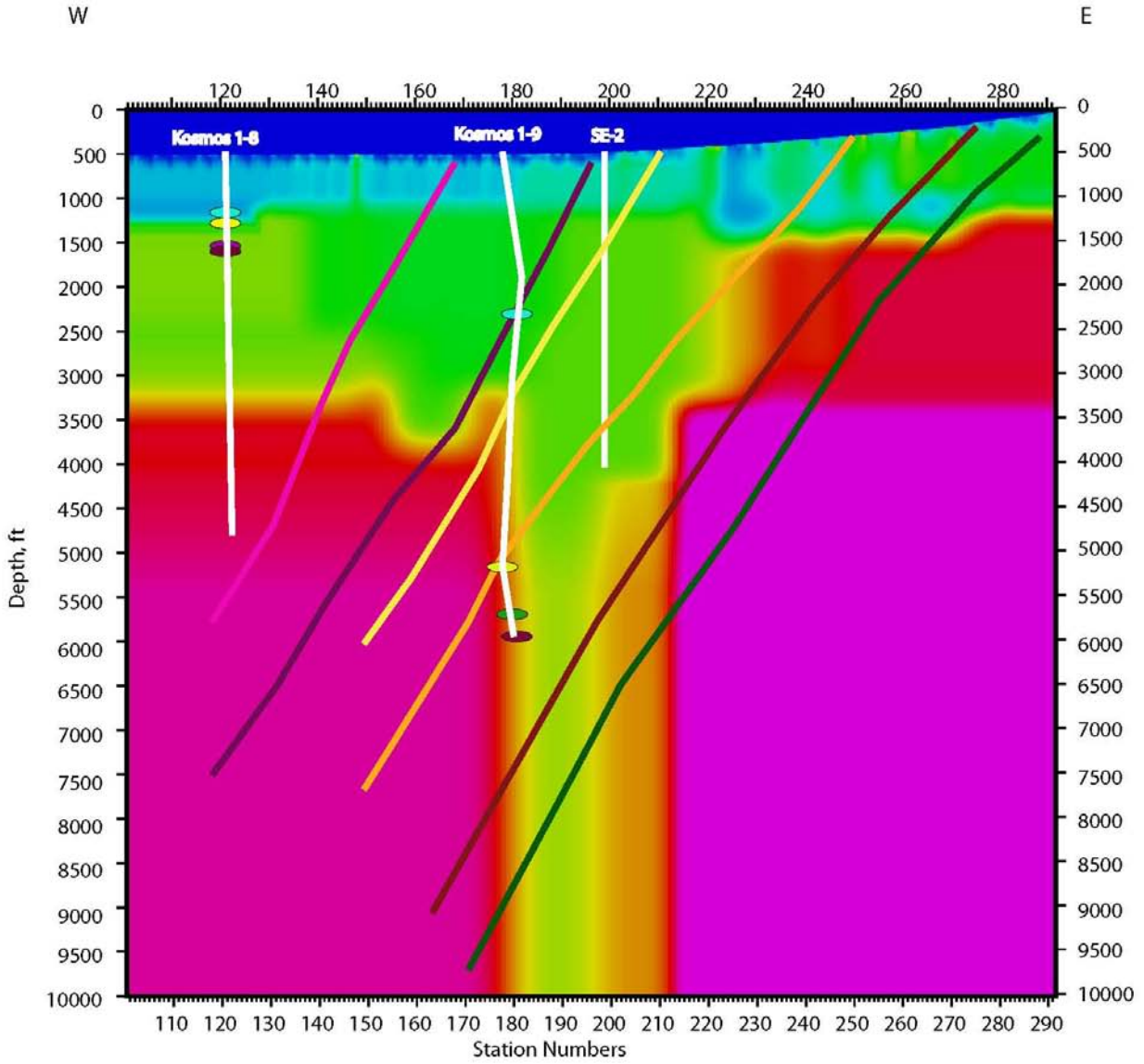


Figure 10h: S-wave velocity model along Line 5 (500) extended in depth showing the faults and discontinuities inferred by the structural team. The interpretations were made in conjunction with the P-wave velocity model (Figure 10g) and the reflection image (Figure 10i). Velocities go from 0 ft/s (blue) to 8,500 ft/s (purple).

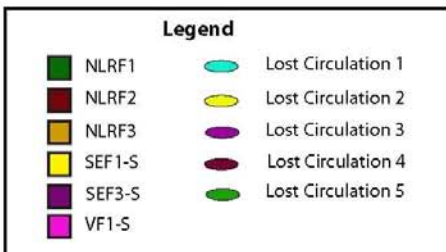
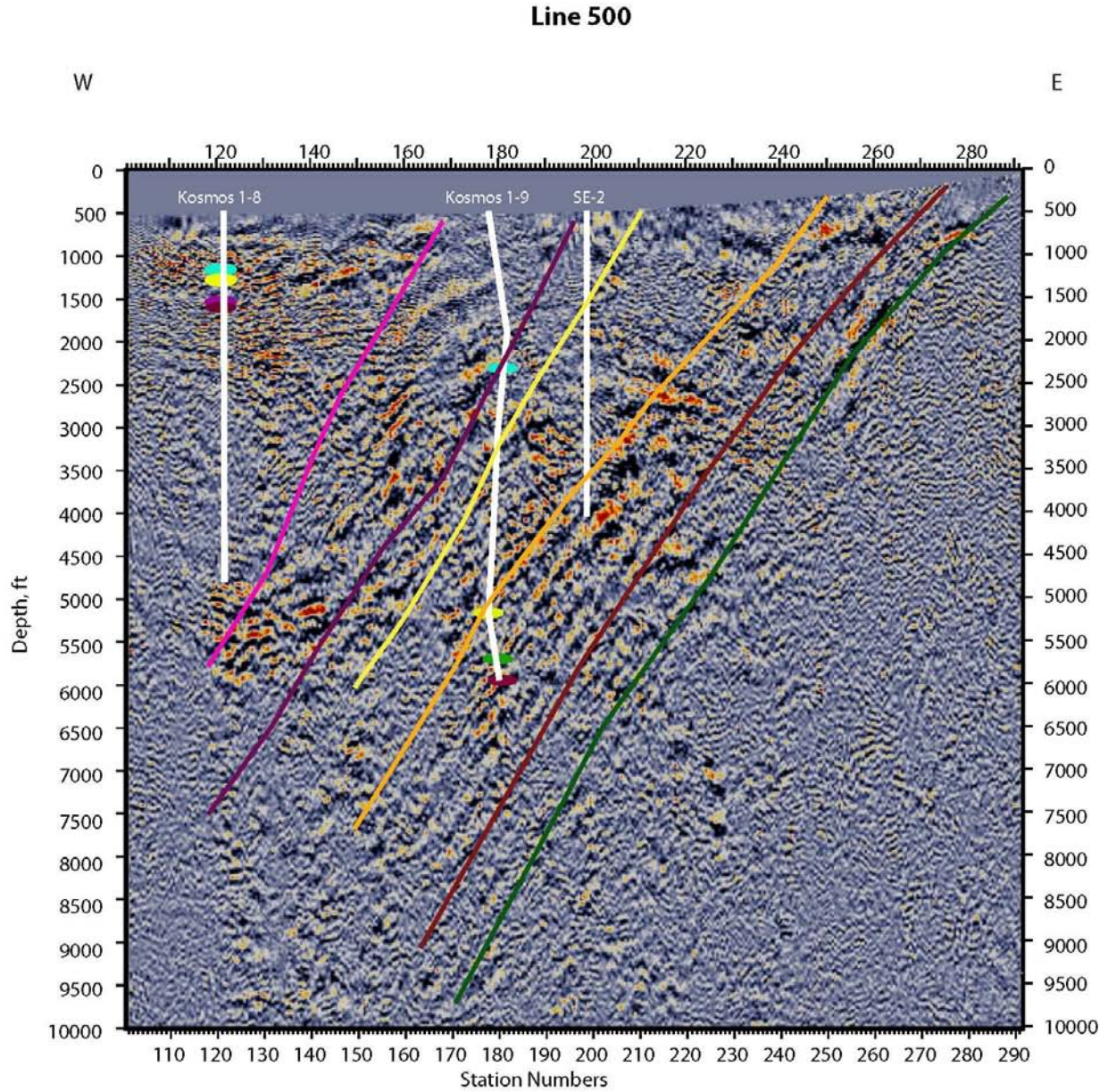


Figure 10i: P-wave depth migrated reflection image along Line 5 (500) showing the faults and discontinuities inferred by the structural team. The interpretations were made in conjunction with the P-wave velocity model (Figure 10g) and the shear-wave image (Figure 10h).

### Line 500

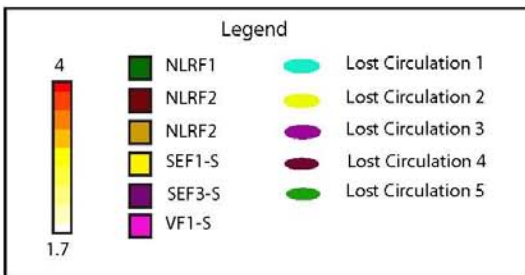
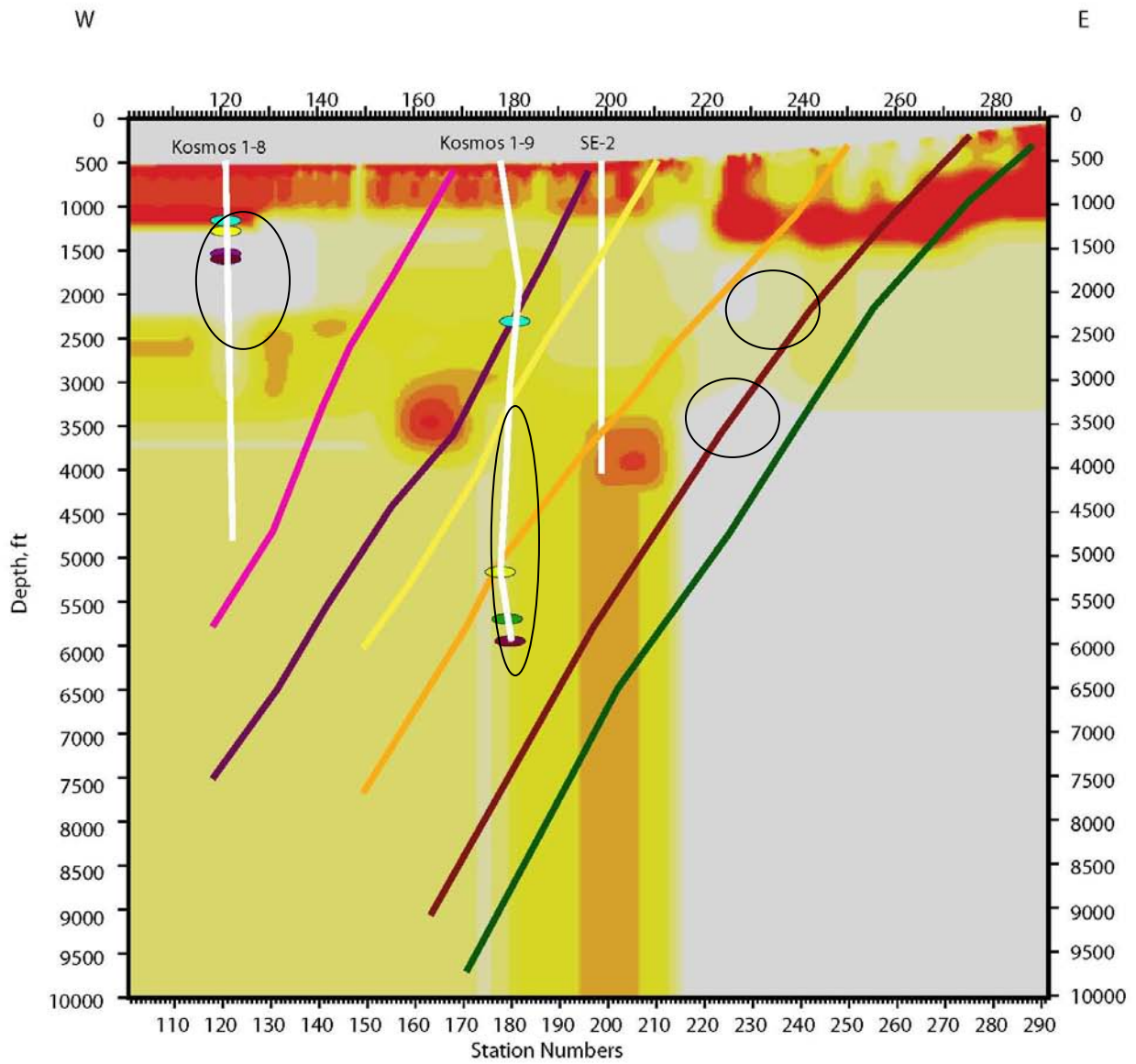


Figure 10j:  $V_p/V_s$  ratio calculated from P-wave and S-wave velocity models along Line 5 (500). The relatively lower  $V_p/V_s$  zones (circles) are potential fractured fluid filled zones.

We also calculate a  $V_p/V_s$  model from the P-wave and S-wave velocities and it is shown in Figure 10j. The low  $V_p/V_s$  zones that lie close to fault intersections and traces are marked as areas of potential fractured or fluid filled fracture zones. These match the fact that lost circulation zones were encountered along Kosmos 1-8 and Kosmos 1-9. Interestingly no low  $V_p/V_s$  zones are encountered along SE-2 which didn't intersect any lost circulation zones. These also coincide with zones of very strong lateral variations in both P-wave and S-wave velocities. The Kosmos 1-9 lost circulation zones fall at the intersection of the well with faults labeled SEF3-S and NLRF-2.

#### 4.7 4.7 Line 6 (600)

Line 6, also called 600, is the in the southern part of the project area, south of line 5 and just north of the Philips well. It runs east-west from station number 101 in the west to 293 in the east (Figure 11a). All of the figures represent true seismic depth sections with no vertical exaggeration.

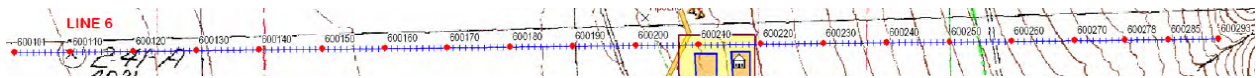


Figure 11a: Line 6 (600) runs east-west from station number 101 in the west to station number 293 in the east.

Figures 11b and 11c show a typical shot gather acquired along Line 6 using P-wave and SH-wave source, respectively. The first arrivals (shown in red) are clearly visible. These were picked and used to obtain the velocity models shown in Figures 11d and 11e, respectively.

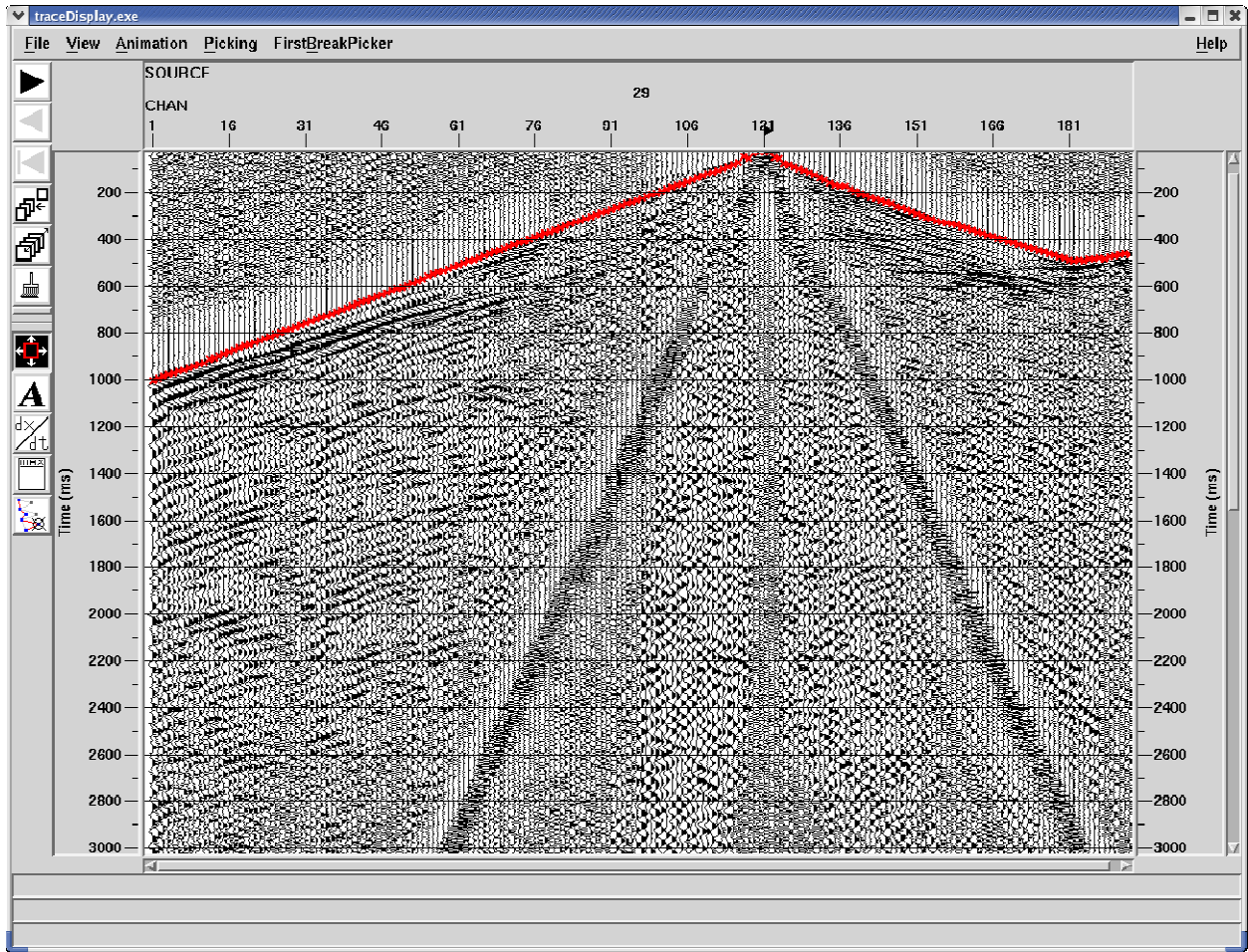


Figure 11b: Typical shot gathers from P-wave data collected along Line 6 (600). The first arrival picks, shown in red, was used to obtain the P-wave velocity model shown in Figure 11d.

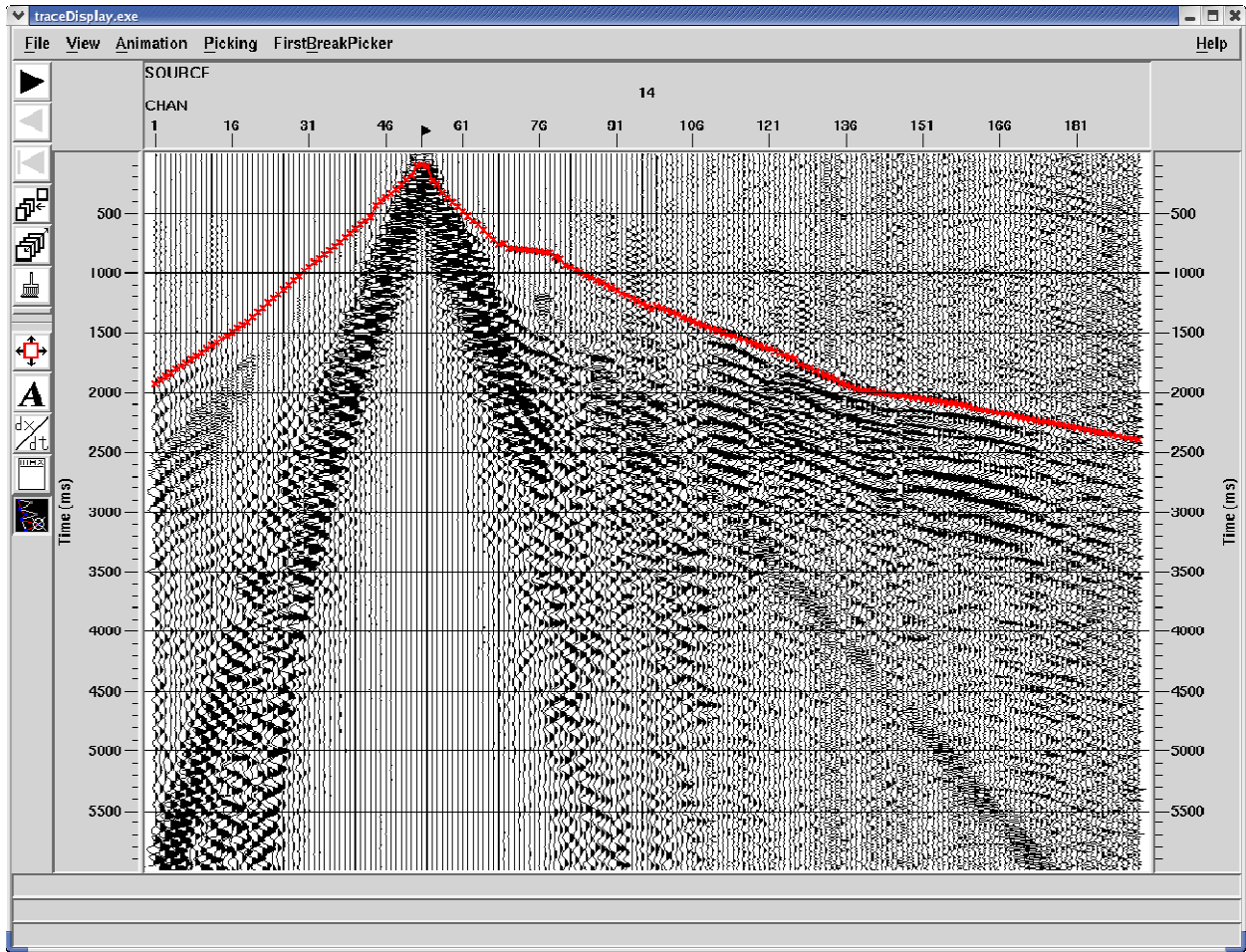


Figure 11c: Typical shot gathers from SH-wave data collected along Line 6 (600). The first arrival picks, shown in red, was used to obtain the S-wave velocity model shown in Figure 11e.

Figures 11d and 11e show the velocity model obtained from optimization of P-wave and SH-wave first arrival data, respectively. P-wave velocities range from 1,500 ft/s to 15,000 ft/s. High velocities in the range of 15,000 ft/s shallow towards the range front in the east. Since the seismic line goes well into the ranges, the higher velocities appear shallower in the east compared to the northern lines. The S-wave velocities range from 500 ft/s to 10,000 ft/s. As with the P-wave velocities, the higher velocities shallow towards the east. There is a distinct lateral change in velocities around station 220.

This model is then extended in depth by interactive velocity modeling. It involved selecting an appropriate gradient that was consistent with the velocities observed along the other lines. Figure 11f shows results of a P-wave depth migration obtained using the P-wave velocity model shown in Figure 11d. Interpretations of the velocity and reflection images are shown in Figures

11g, 11h, and 11i. During the interpretation both the reflection images and the velocity model was used to identify faults and structures. Faults were inferred by direct reflections of them or by truncations of sub-horizontal reflections. The naming convention was developed by Greg Rhodes.

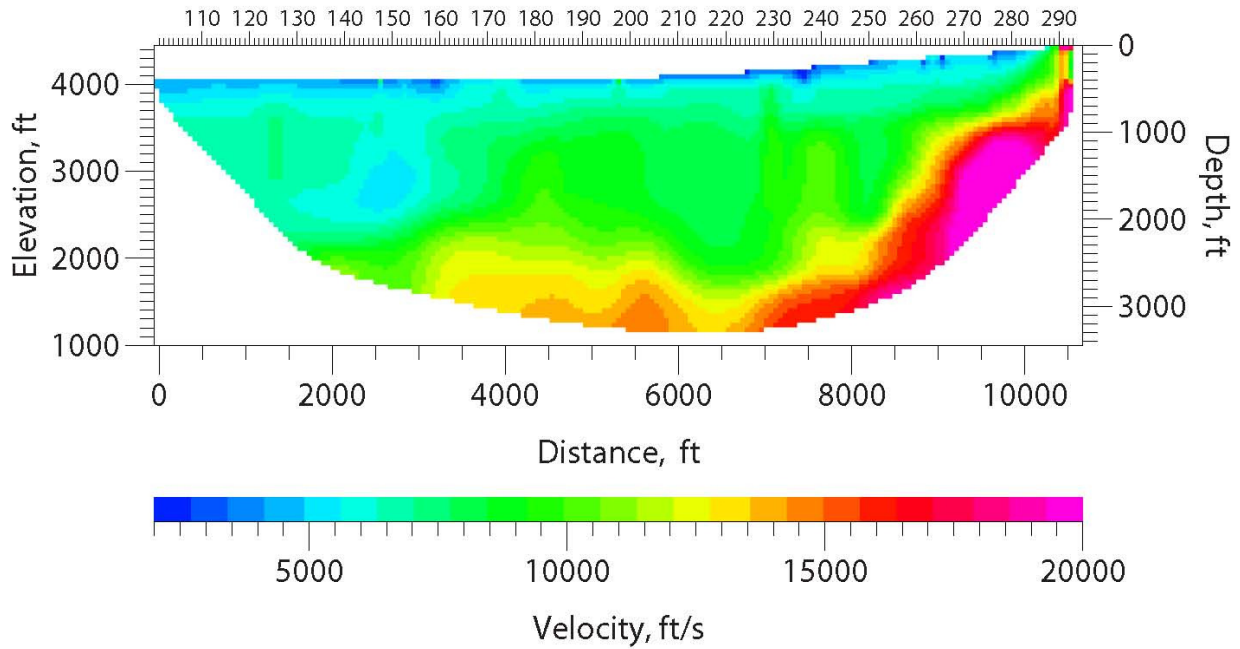


Figure 11d: P-wave velocity model along Line 6 (600) obtained from optimization of P-wave first-arrival travel times.

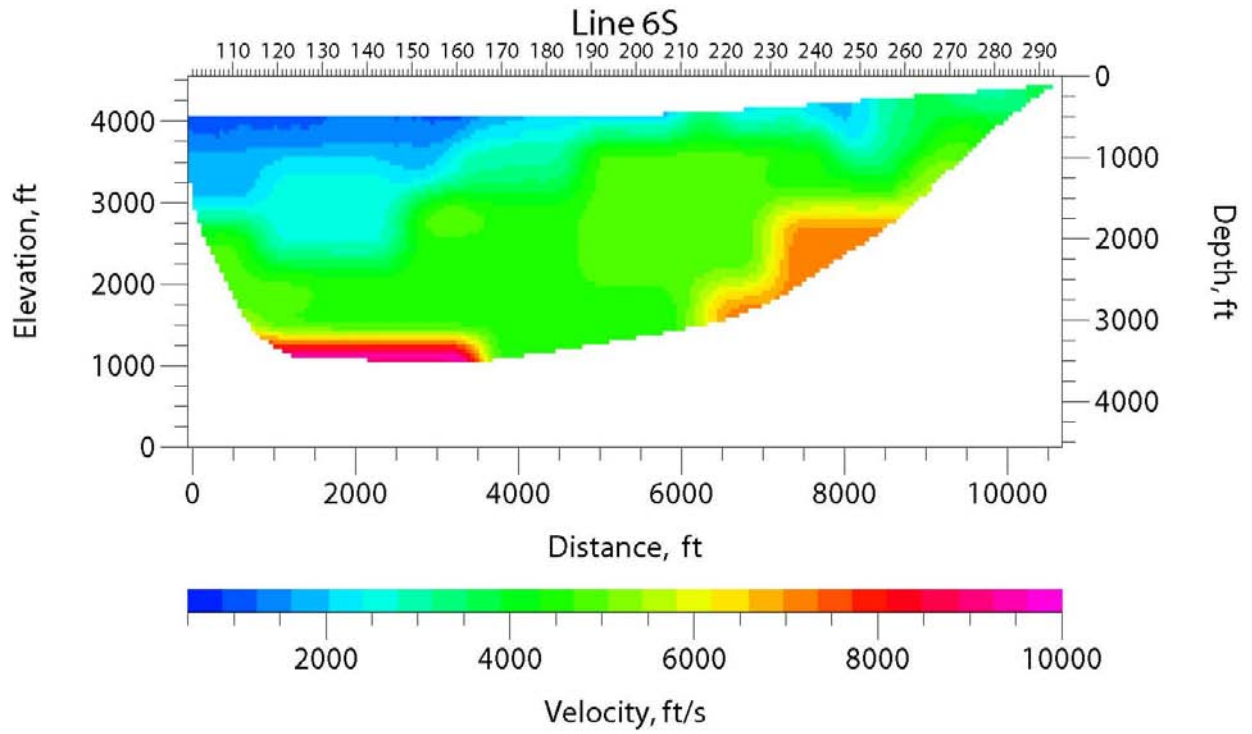


Figure 11e: S-wave velocity model along Line 6 (600) obtained from optimization of SH-wave first-arrival travel times.

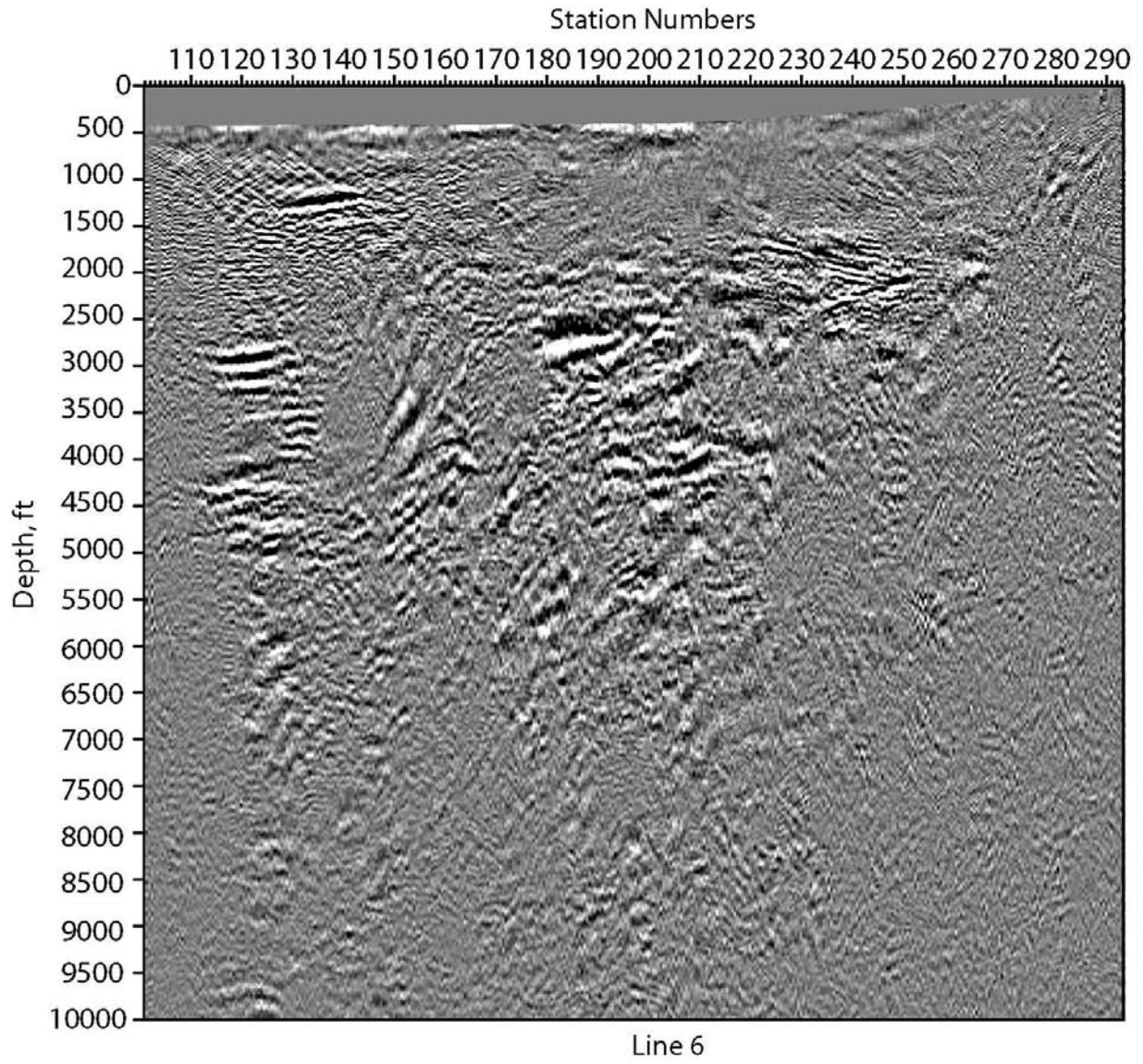


Figure 11f: Depth-migrated image along Line 6 (600) using the velocity model shown in Figure 11g.

### Line 600

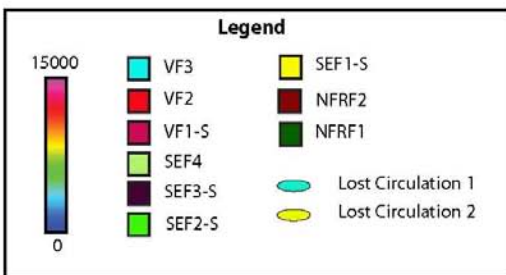
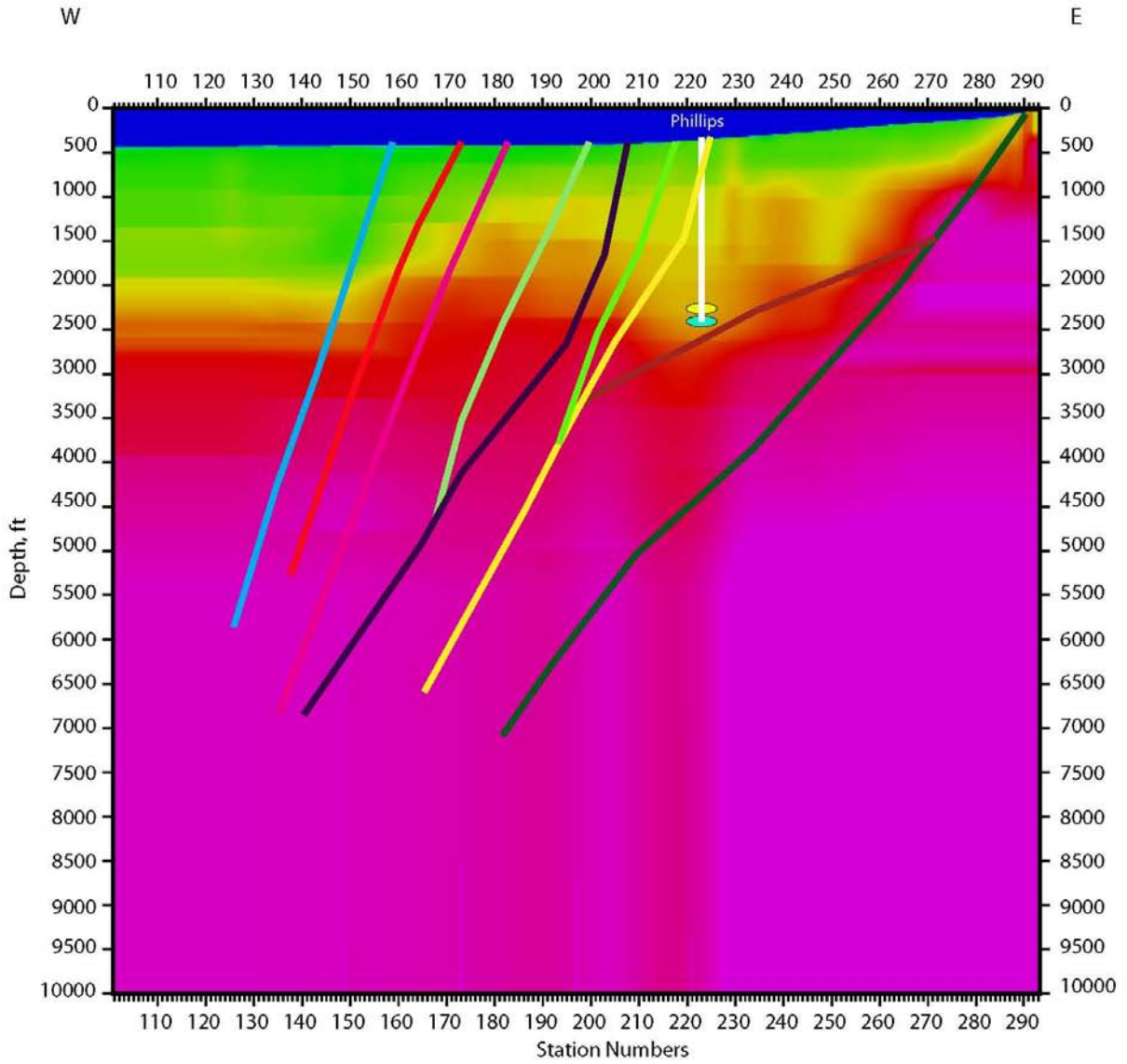


Figure 11g: P-wave velocity model along Line 6 (600) extended in depth. The interpretations were made in conjunction with the shear-wave velocity model (Figure 11h) and the P-wave reflection image (Figure 11i). Velocities go from 0 ft/s (blue) to 15,000 ft/s (purple).

# Line 600

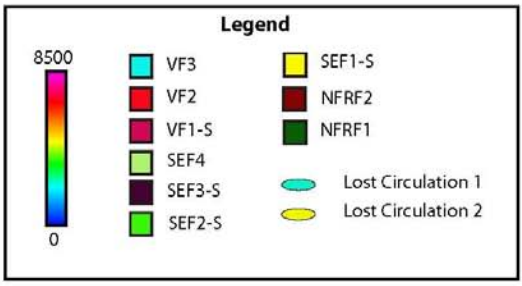
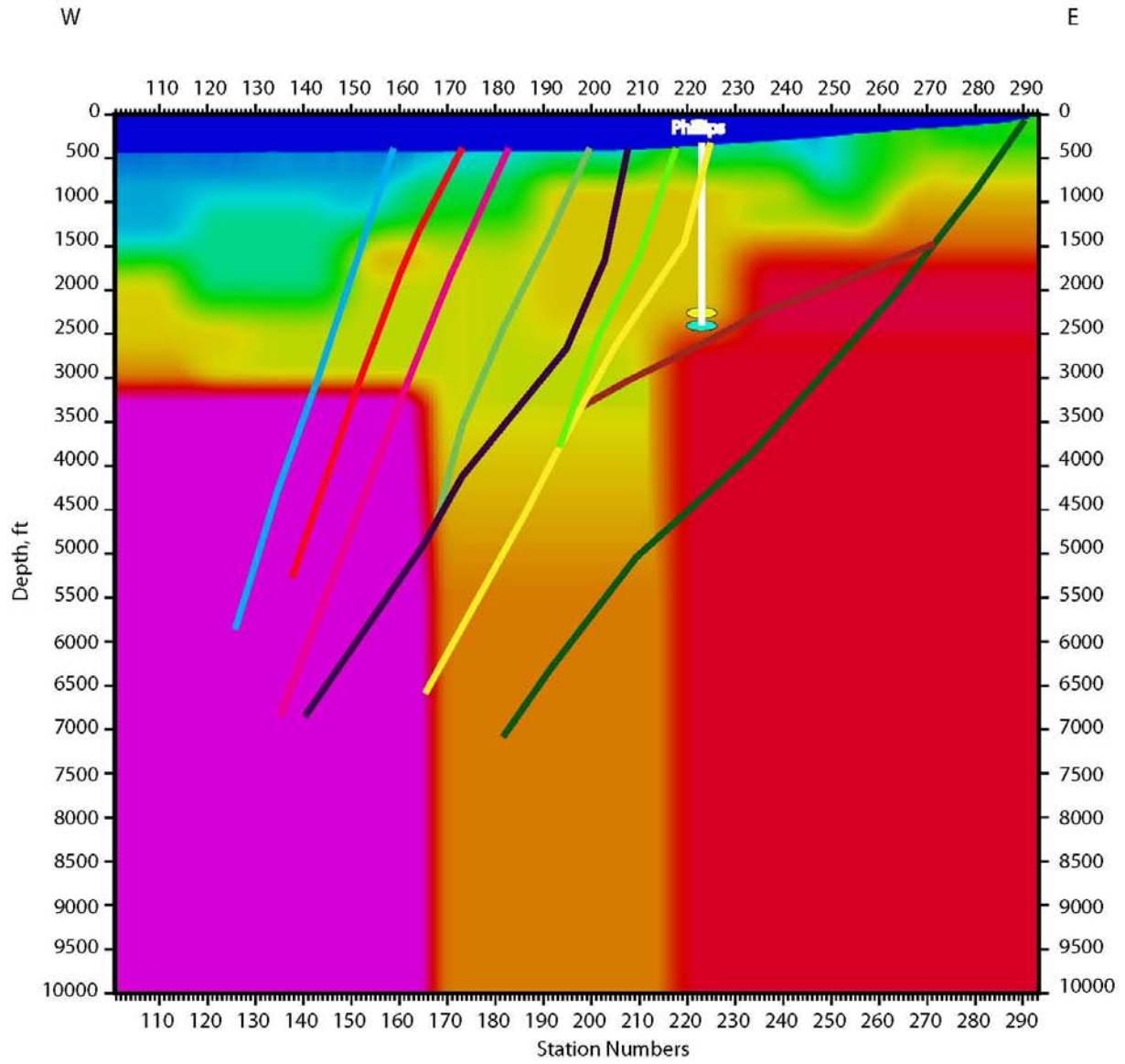


Figure 11h: S-wave velocity model along Line 6 (600) extended in depth showing the faults and discontinuities inferred by the structural team. The interpretations were made in conjunction with the P-wave velocity model (Figure 11g) and the reflection image (Figure 11i). Velocities go from 0 ft/s (blue) to 8,500 ft/s (purple).

# Line 600

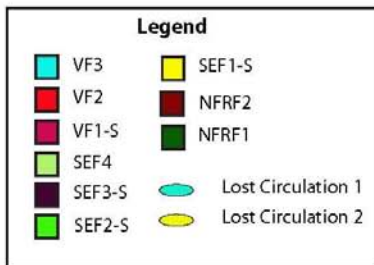
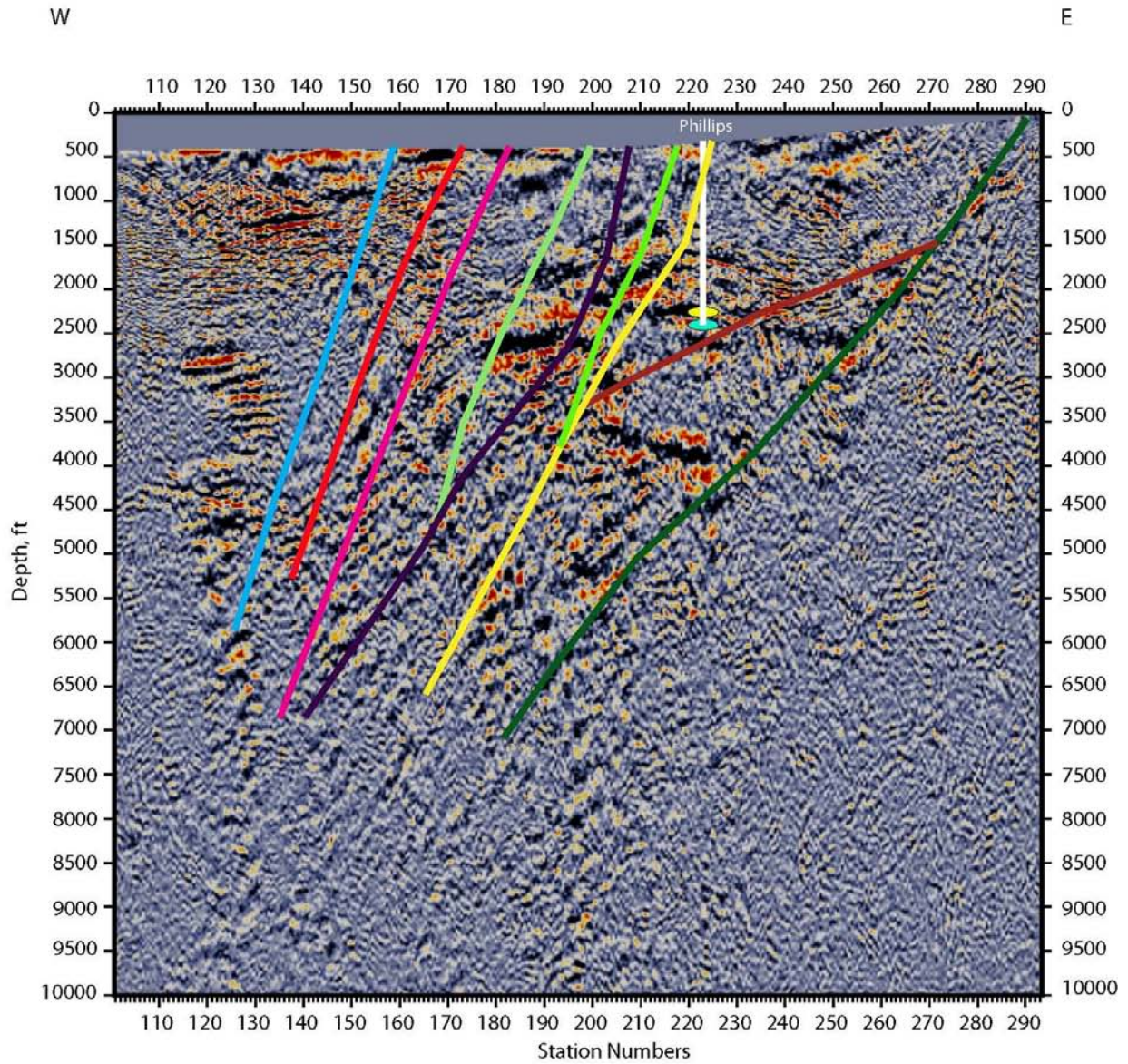


Figure 11i: P-wave depth migrated reflection image along Line 6 (600) showing the faults and discontinuities inferred by the structural team. The interpretations were made in conjunction with the P-wave velocity model (Figure 11g) and the shear-wave image (Figure 11h).

### Line 600

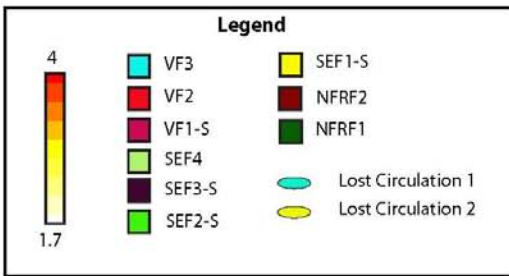
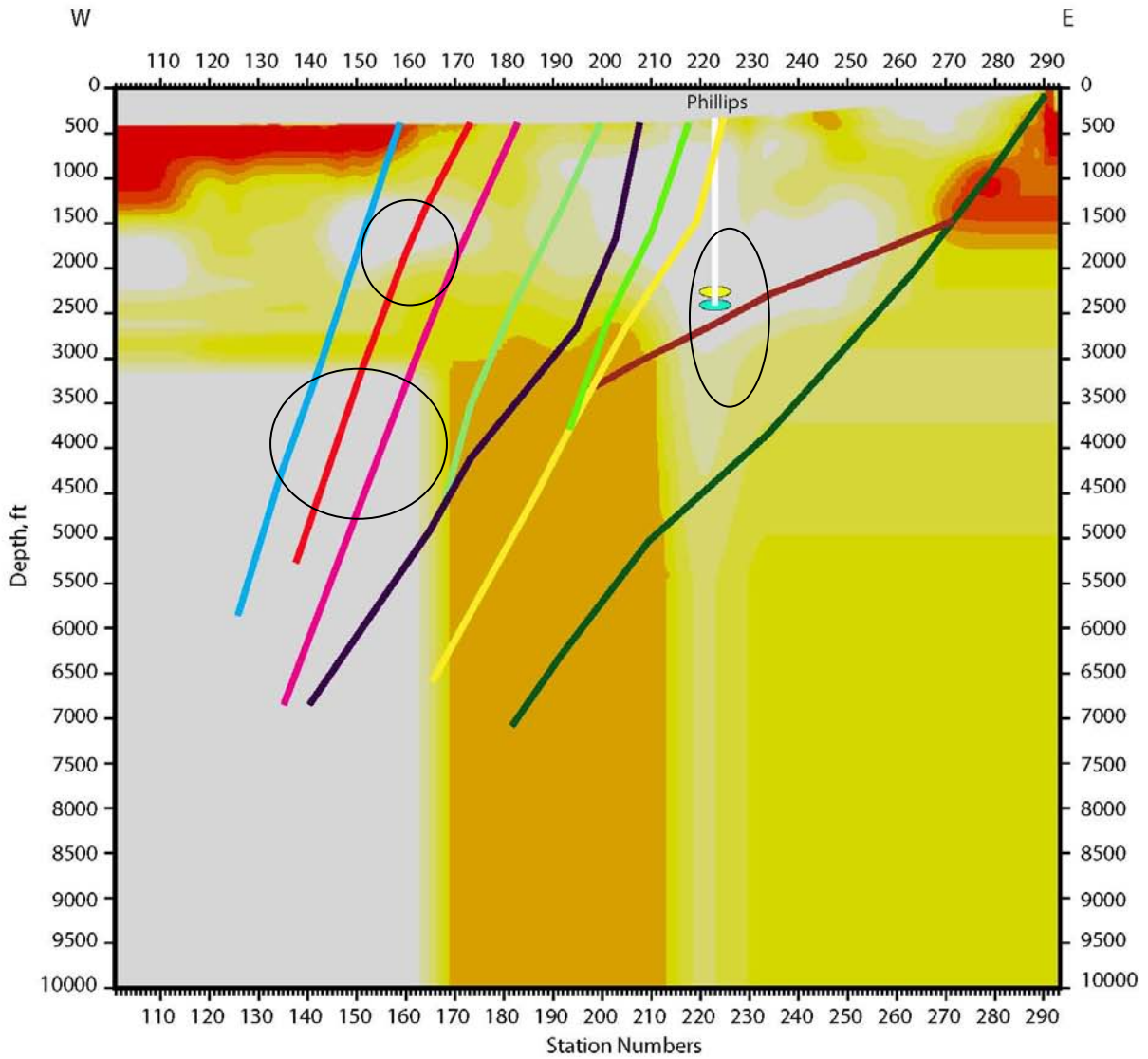


Figure 11j:  $V_p/V_s$  ratio calculated from P-wave and S-wave velocity models along Line 6 (600). The relatively lower  $V_p/V_s$  zones (circles) are potential fractured fluid filled zones.

We also calculate a  $V_p/V_s$  model from the P-wave and S-wave velocities and it is shown in Figure 11j. The low  $V_p/V_s$  zones that lie close to fault intersections and traces are marked as areas of potential fractured or fluid filled fracture zones. The lost circulation encountered along Phillips well lies along the low  $V_p/V_s$  zone. These also coincide with zones of very strong lateral variations in both P-wave and S-wave velocities and location of fault NFRF2.

#### 4.8 4.8 Line 7 (700)

Line 7, also called 700, is the in the southern part of the project area, south of line 6 and just north of 75B-16 and 75-16 wells. It runs east-west from station number 101 in the west to 293 in the east (Figure 12a). All of the figures represent true seismic depth sections with no vertical exaggeration.

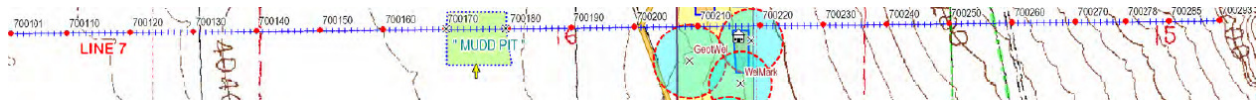


Figure 12a: Line 7 (700) runs east-west from station number 101 in the west to station number 293 in the east.

Figures 12b and 12c show a typical shot gather acquired along Line 7 using P-wave and SH-wave source, respectively. The first arrivals (shown in red) were picked and used to obtain the velocity models shown in Figures 12d and 12e, respectively.

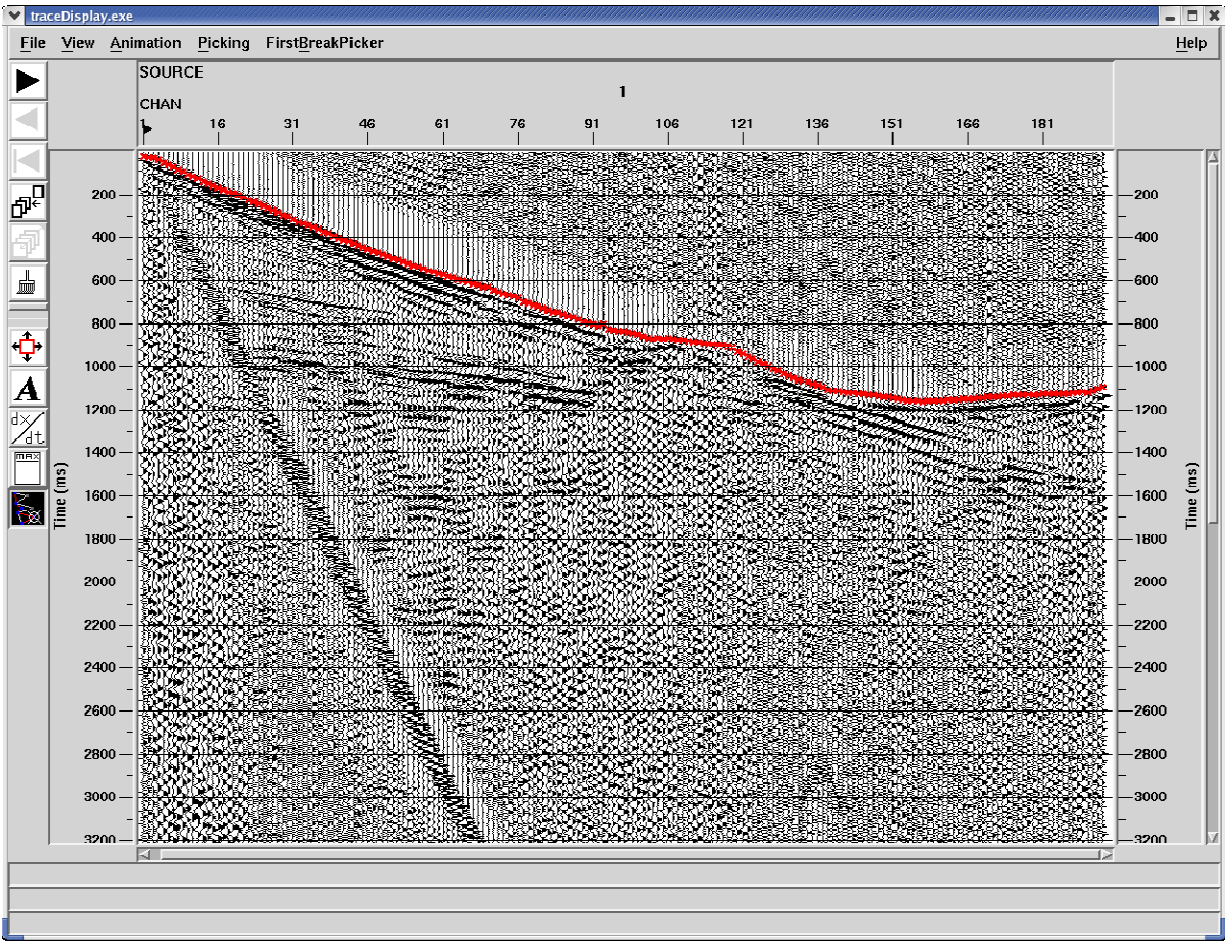


Figure 12b: Typical shot gathers from P-wave data collected along Line 7 (700). The first arrival picks, shown in red, was used to obtain the P-wave velocity model shown in Figure 12d.

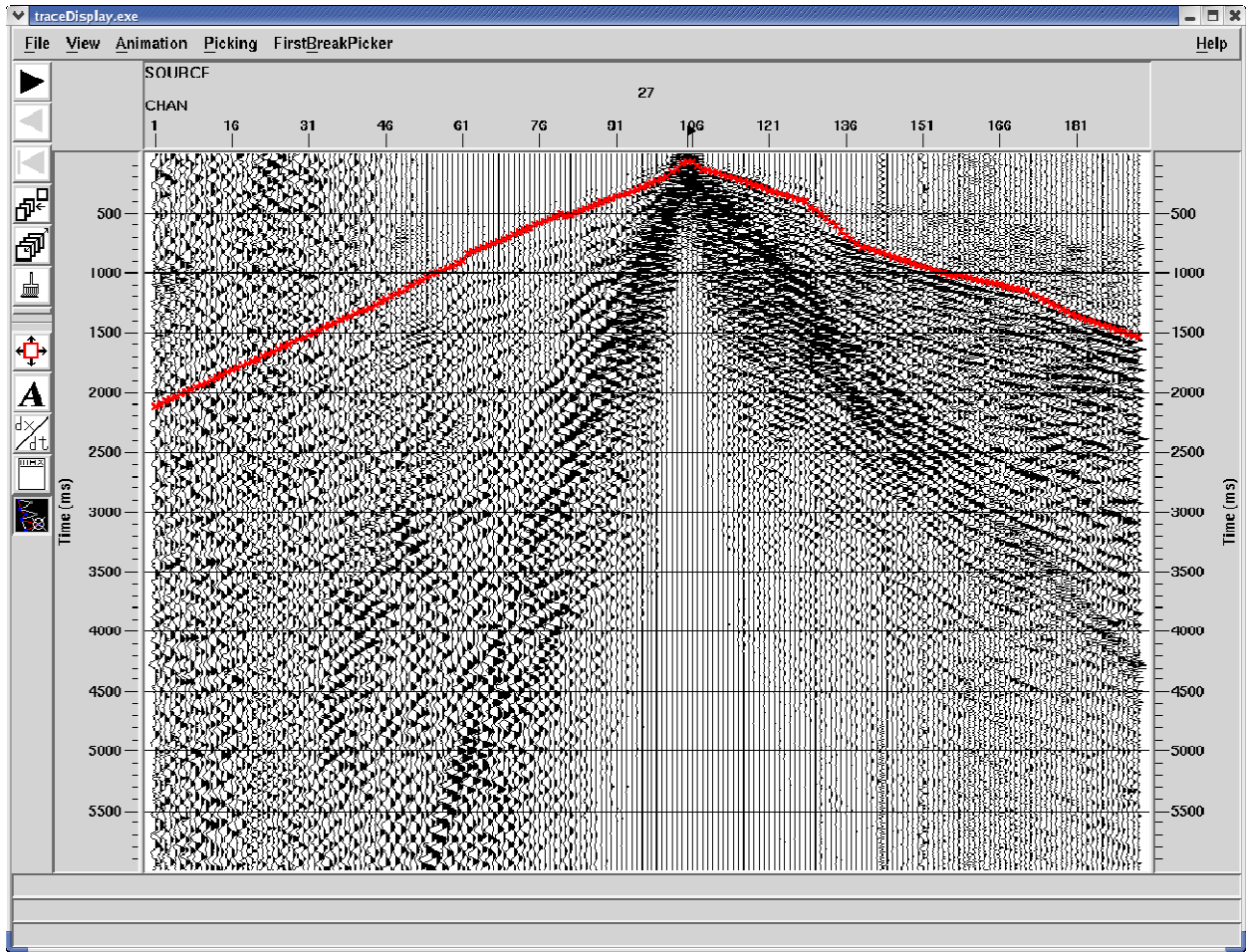


Figure 12c: Typical shot gathers from SH-wave data collected along Line 7 (700). The first arrival picks, shown in red, was used to obtain the S-wave velocity model shown in Figure 12e.

Figures 12d and 12e show the velocity model obtained from optimization of P-wave and SH-wave first arrival data, respectively. P-wave velocities range from 1,500 ft/s to 20,000 ft/s. High velocities in the range of 15,000 ft/s shallow towards the range front in the east. Since the seismic line goes well into the ranges, the higher velocities appear shallower in the east compared to the northern lines. The S-wave velocities range from 500 ft/s to 10,000 ft/s. As with the P-wave velocities, the higher velocities shallow towards the east. There is a distinct lateral change in velocities around station 220.

This model is then extended in depth by interactive velocity modeling. It involved selecting an appropriate gradient that was consistent with the velocities observed along the other lines. Figure 12f shows results of a P-wave depth migration obtained using the P-wave velocity model shown in Figure 12d. Interpretations of the velocity and reflection images are shown in Figures

12g, 12h, and 12i. During the interpretation both the reflection images and the velocity model was used to identify faults and structures. Faults were inferred by direct reflections of them or by truncations of sub-horizontal reflections. The naming convention was developed by Greg Rhodes.

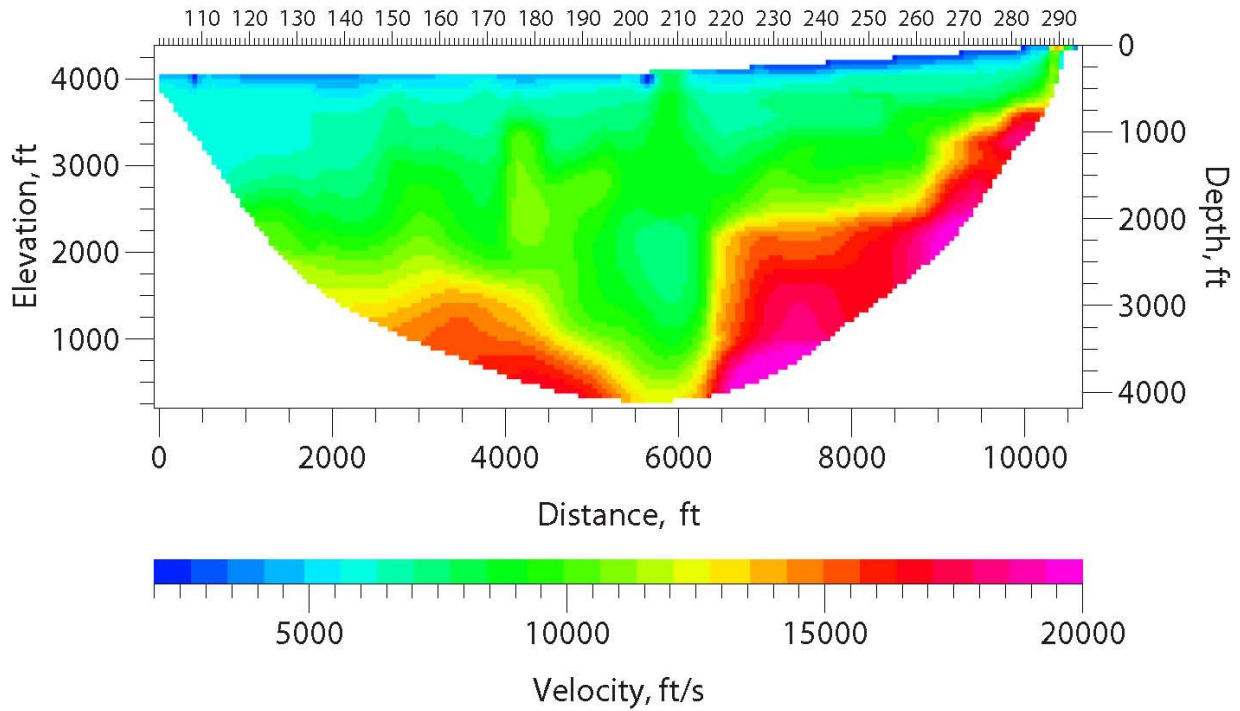


Figure 12d: P-wave velocity model along Line 7 (700) obtained from optimization of P-wave first-arrival travel times.

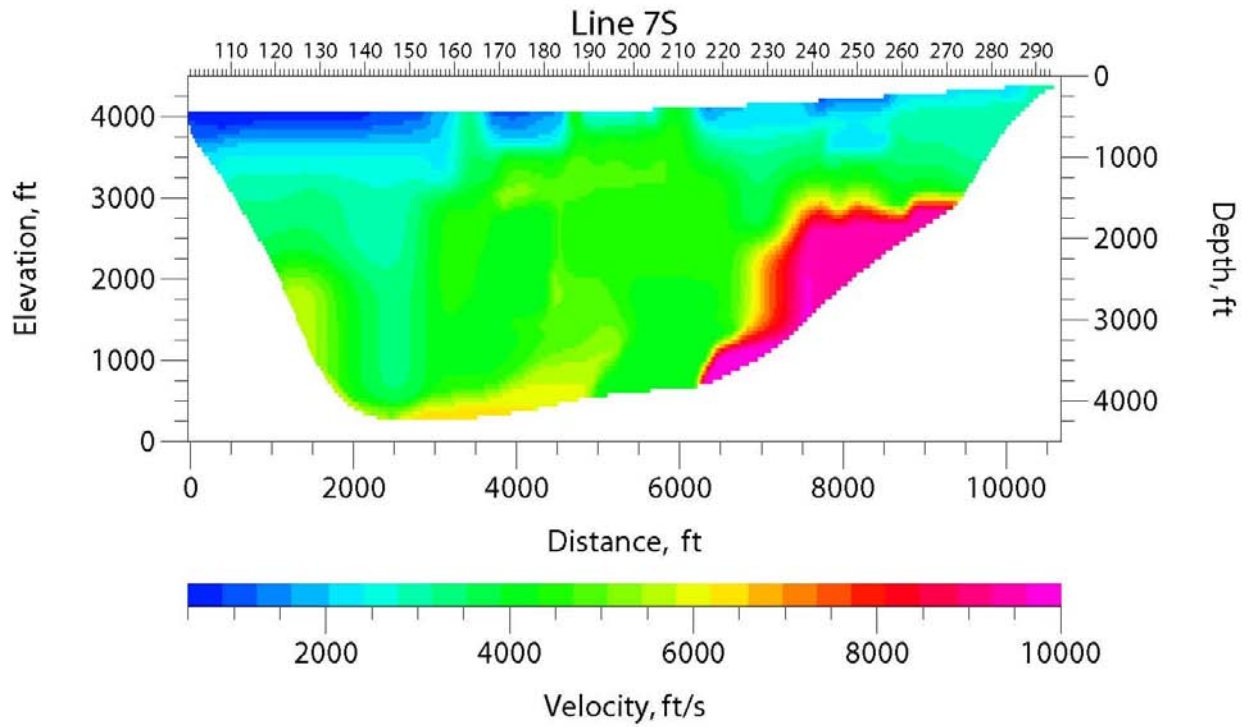


Figure 12e: S-wave velocity model along Line 7 (700) obtained from optimization of SH-wave first-arrival travel times.

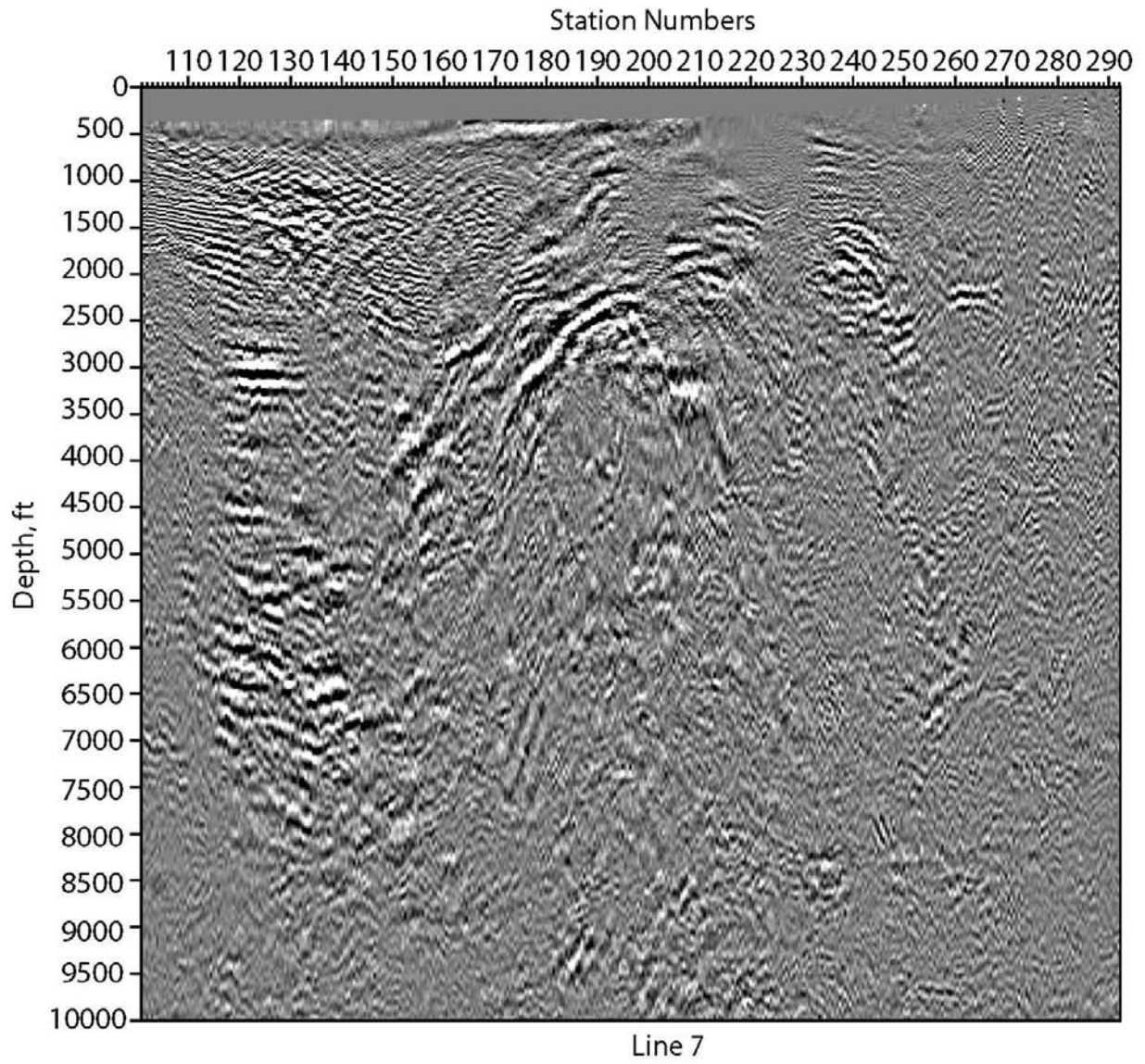


Figure 12f: Depth-migrated image along Line 7 (700) using the velocity model shown in Figure 12g.

### Line 700

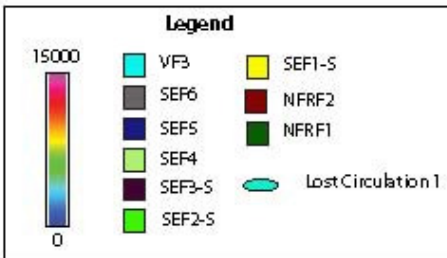
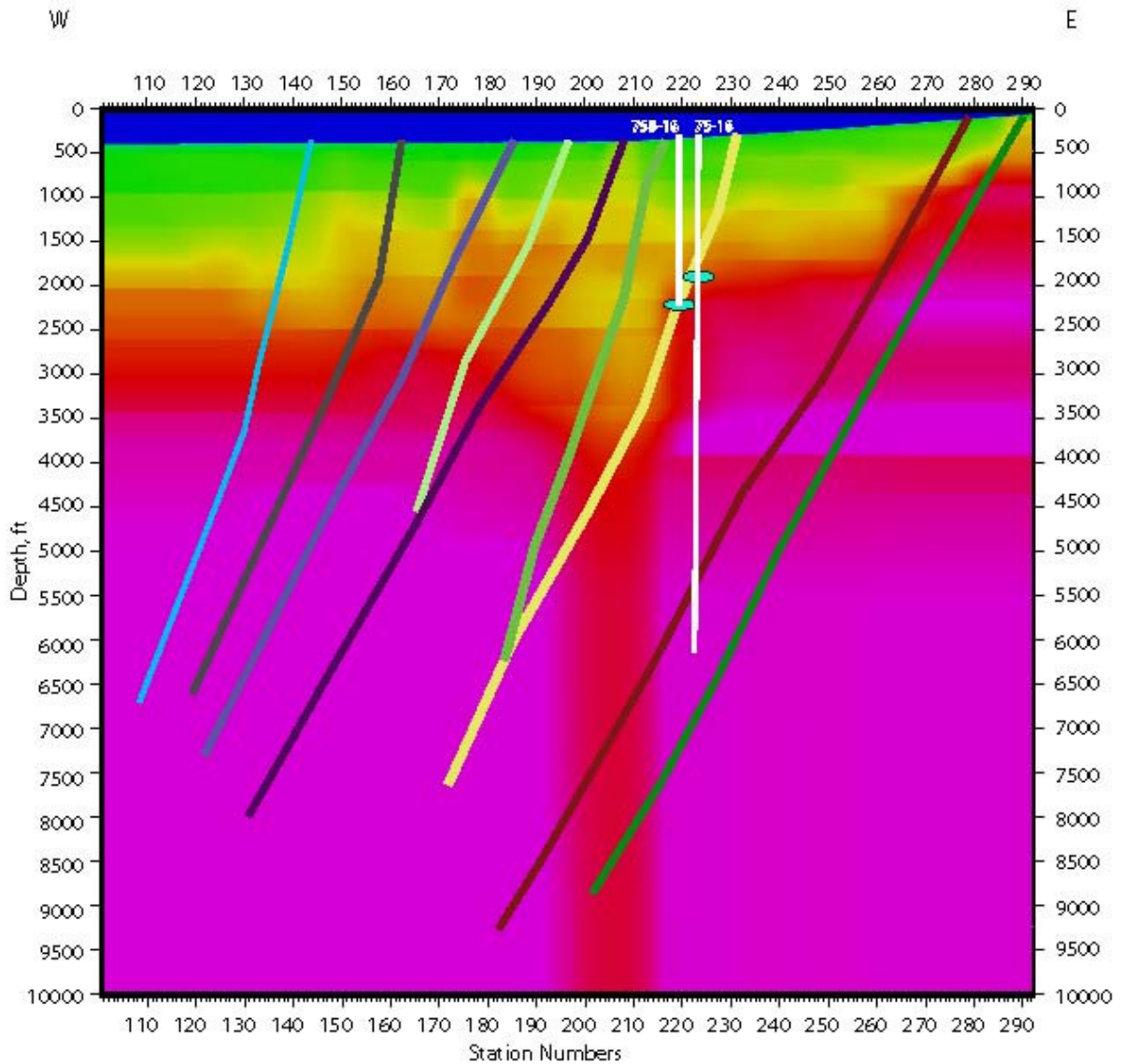


Figure 12g: P-wave velocity model along Line 7 (700) extended in depth. The interpretations were made in conjunction with the shear-wave velocity model (Figure 12h) and the P-wave reflection image (Figure 12i). Velocities go from 0 ft/s (blue) to 15,000 ft/s (purple).

### Line 700

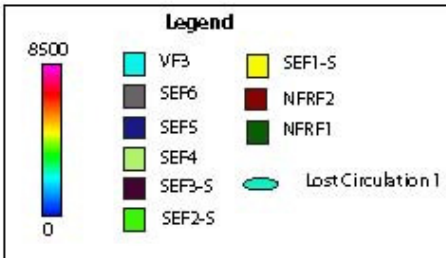
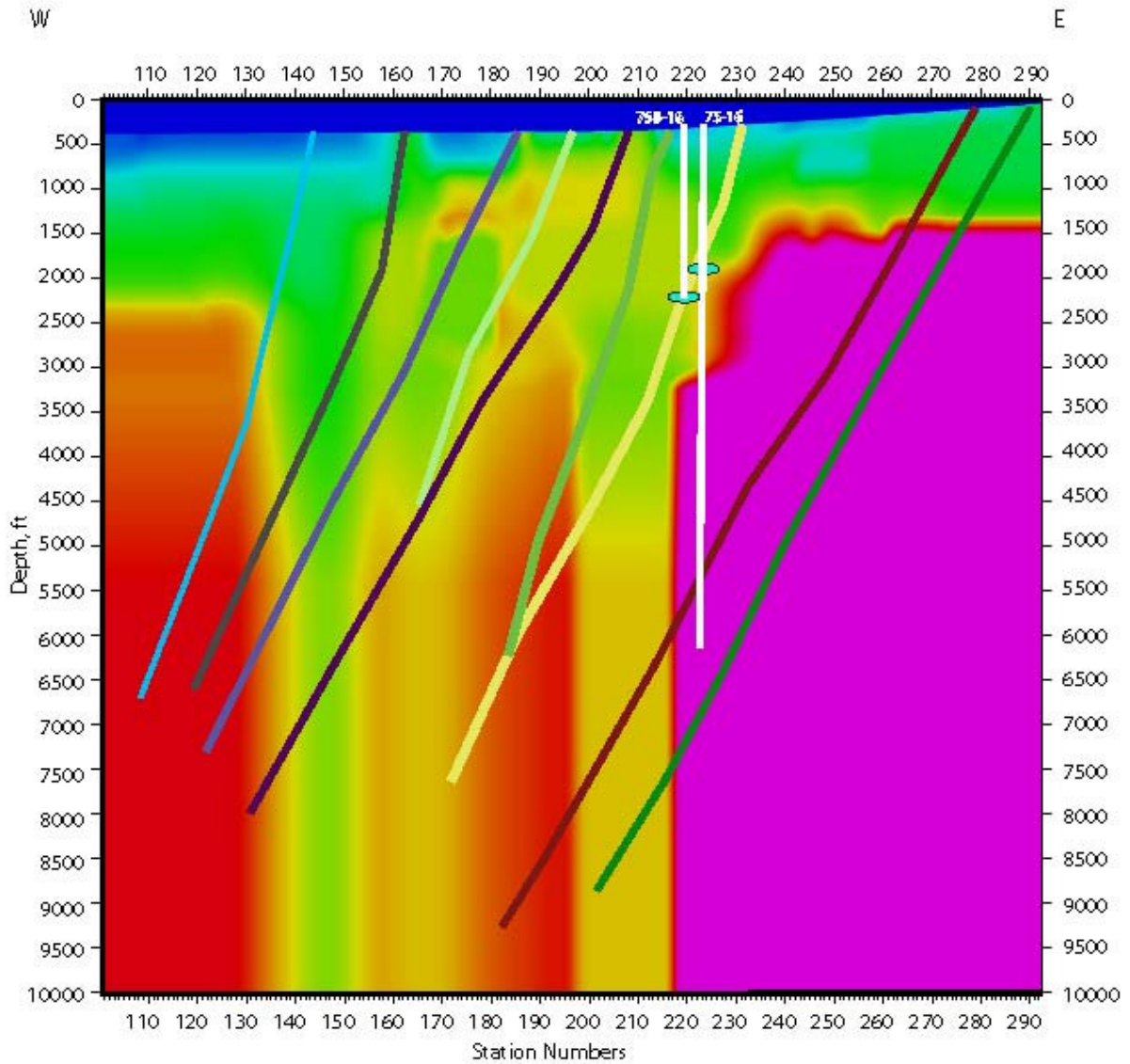


Figure 12h: S-wave velocity model along Line 7 (700) extended in depth showing the faults and discontinuities inferred by the structural team. The interpretations were made in conjunction with the P-wave velocity model (Figure 12g) and the reflection image (Figure 12i). Velocities go from 0 ft/s (blue) to 8,500 ft/s (purple).

### Line 700

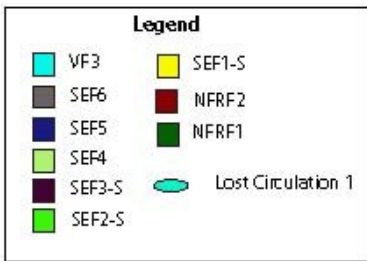
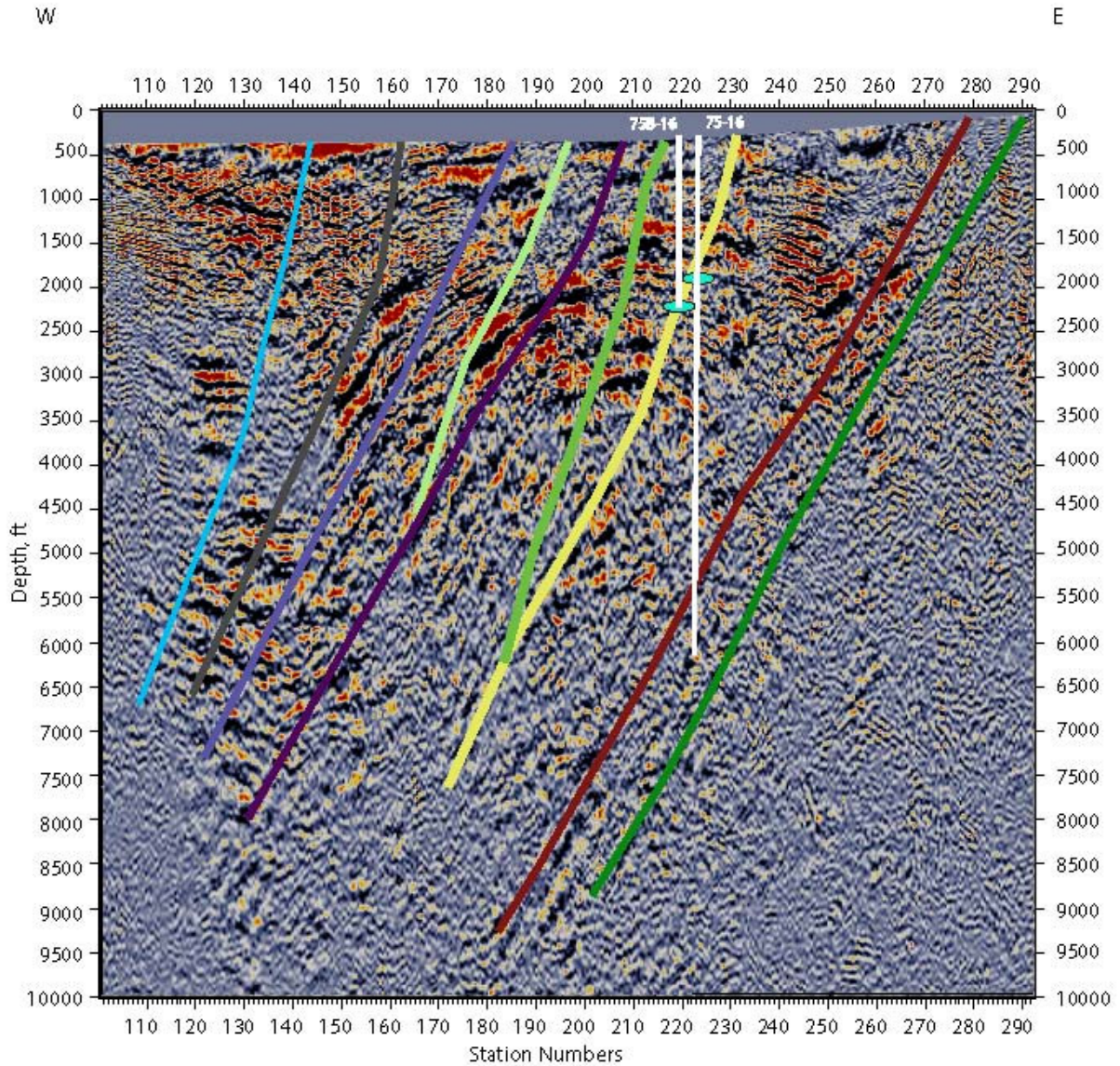


Figure 12i: P-wave depth migrated reflection image along Line 7 (700) showing the faults and discontinuities inferred by the structural team. The interpretations were made in conjunction with the P-wave velocity model (Figure 12g) and the shear-wave image (Figure 12h).

# Line 700

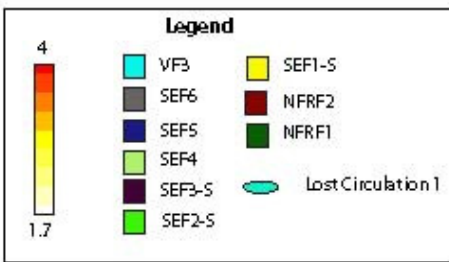
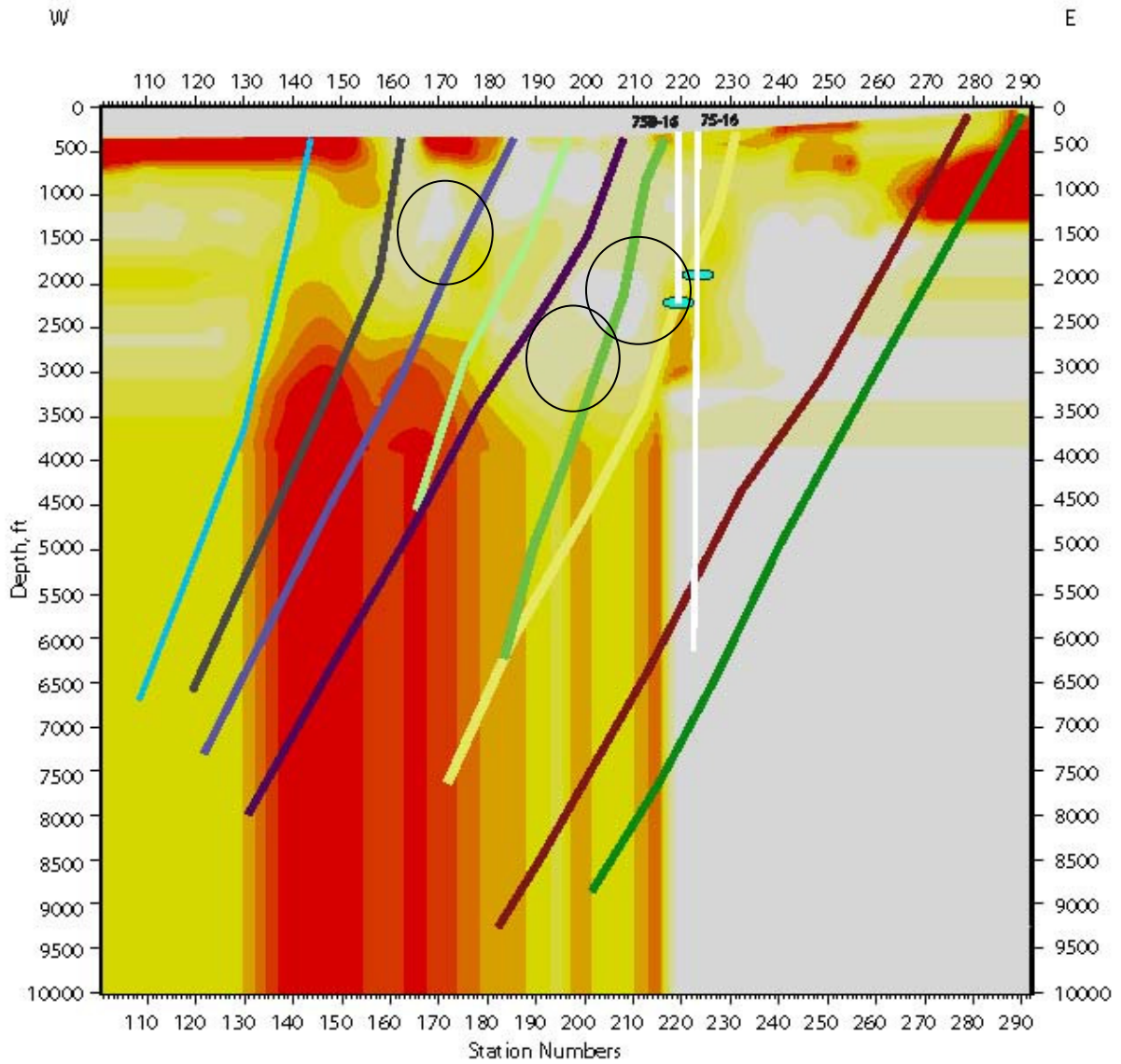


Figure 12j:  $V_p/V_s$  ratio calculated from P-wave and S-wave velocity models along Line 7 (700). The relatively lower  $V_p/V_s$  zones (circles) are potential fractured fluid filled zones.

We also calculate a  $V_p/V_s$  model from the P-wave and S-wave velocities and it is shown in Figure 12j. The low  $V_p/V_s$  zones that lie close to fault intersections and traces are marked as areas of potential fractured or fluid filled fracture zones. The lost circulation encountered along 75-16 and 75B-16 well lies along the low  $V_p/V_s$  zone. The fault SEF1-S seems to act as a conduit for the fluids to migrate up. The lost circulation occurs at the intersection of these faults with the well. These zones also match very well with the strong lateral velocity variation seen in the velocity model (both P-wave and S-wave) around station 220.

#### 4.9 4.9 Line 8 (800)

Line 8, also called 800, is the in the southern part of the project area, south of line 7 and just north of well 76-16. It runs east-west from station number 101 in the west to 293 in the east (Figure 13a). All of the figures represent true seismic depth sections with no vertical exaggeration.

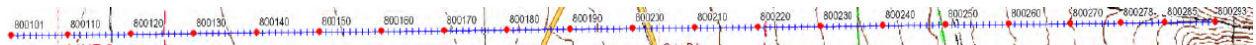


Figure 13a: Line 8 (800) runs east-west from station number 101 in the west to station number 293 in the east.

Figures 13b and 13c show a typical shot gather acquired along Line 8 using P-wave and SH-wave source, respectively. The first arrivals (shown in red) were picked and used to obtain the velocity models shown in Figures 13d and 13e, respectively.

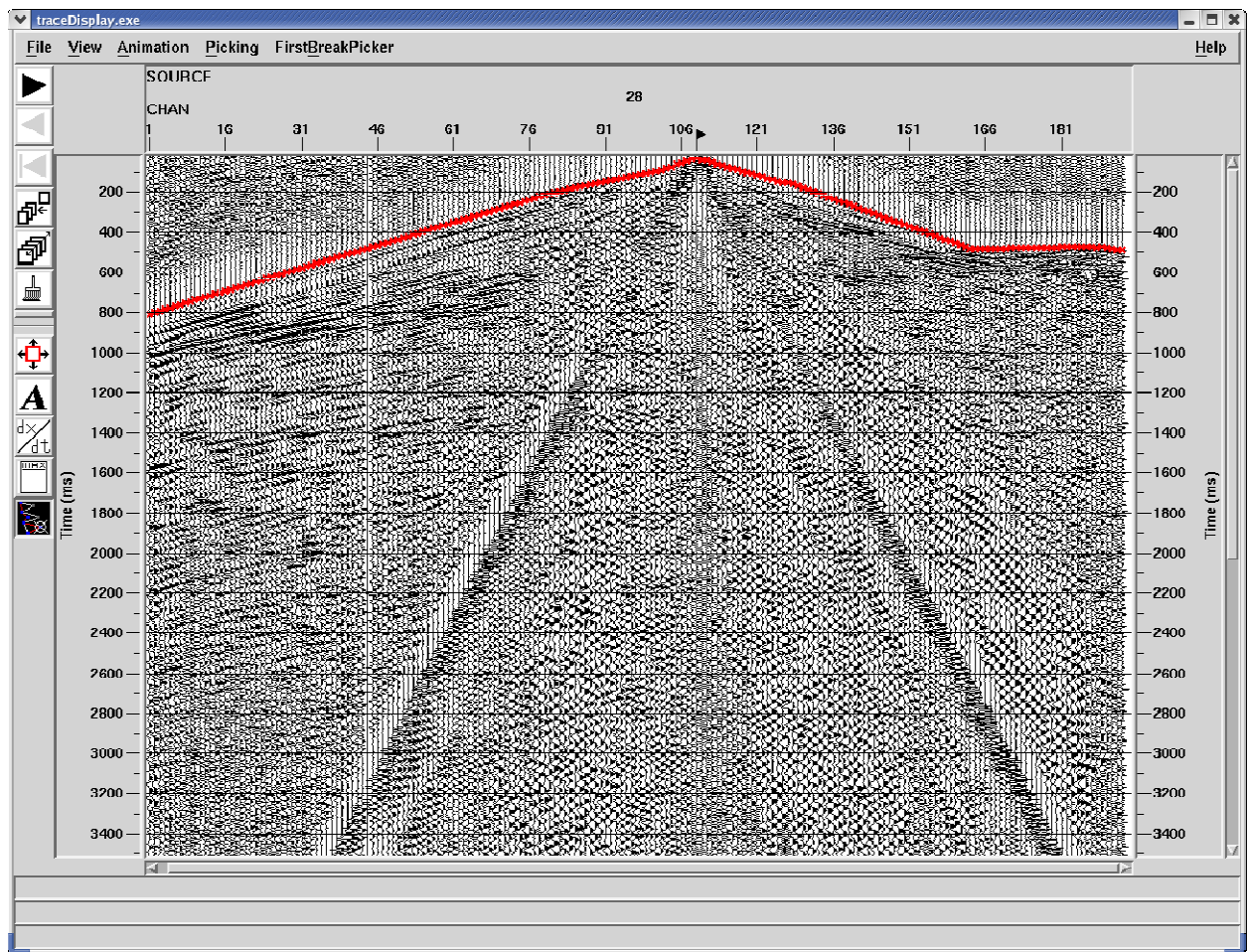


Figure 13b: Typical shot gathers from P-wave data collected along Line 8 (800). The first arrival picks, shown in red, was used to obtain the P-wave velocity model shown in Figure 13d.

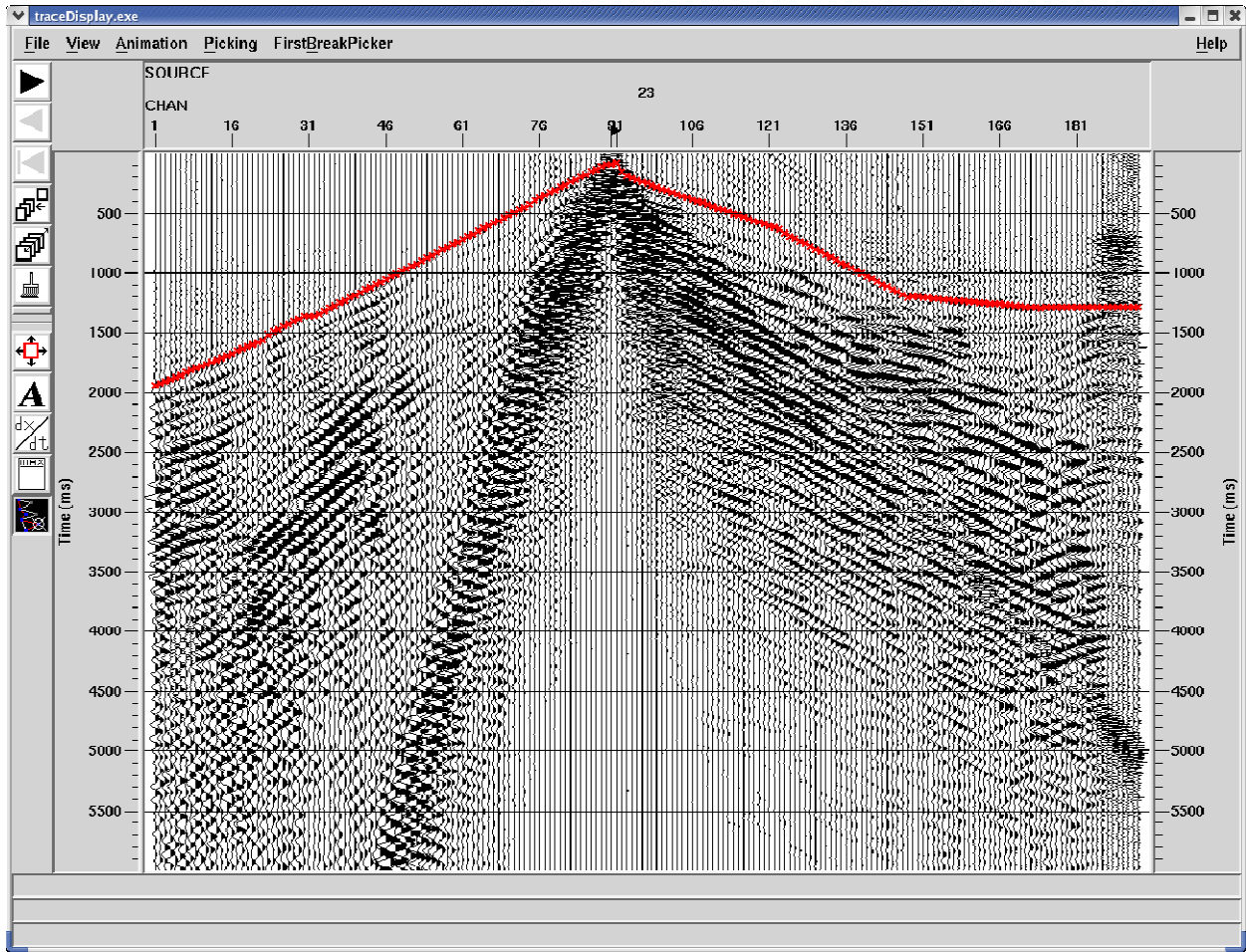


Figure 13c: Typical shot gathers from SH-wave data collected along Line 8 (800). The first arrival picks, shown in red, was used to obtain the S-wave velocity model shown in Figure 13e.

Figures 13d and 13e show the velocity model obtained from optimization of P-wave and SH-wave first arrival data, respectively. P-wave velocities range from 1,500 ft/s to 20,000 ft/s. High velocities in the range of 15,000 ft/s shallow towards the range front in the east. Since the seismic line goes well into the ranges, the higher velocities appear shallower in the east compared to the northern lines. The S-wave velocities range from 500 ft/s to 10,000 ft/s. As with the P-wave velocities, the higher velocities shallow towards the east. There is a distinct lateral change in velocities around station 180.

This model is then extended in depth by interactive velocity modeling. It involved selecting an appropriate gradient that was consistent with the velocities observed along the other lines. Figure 13f shows results of a P-wave depth migration obtained using the P-wave velocity model shown in Figure 13d. Interpretations of the velocity and reflection images are shown in Figures

13g, 13h, and 13i. During the interpretation both the reflection images and the velocity model was used to identify faults and structures. Faults were inferred by direct reflections of them or by truncations of sub-horizontal reflections. The naming convention was developed by Greg Rhodes.

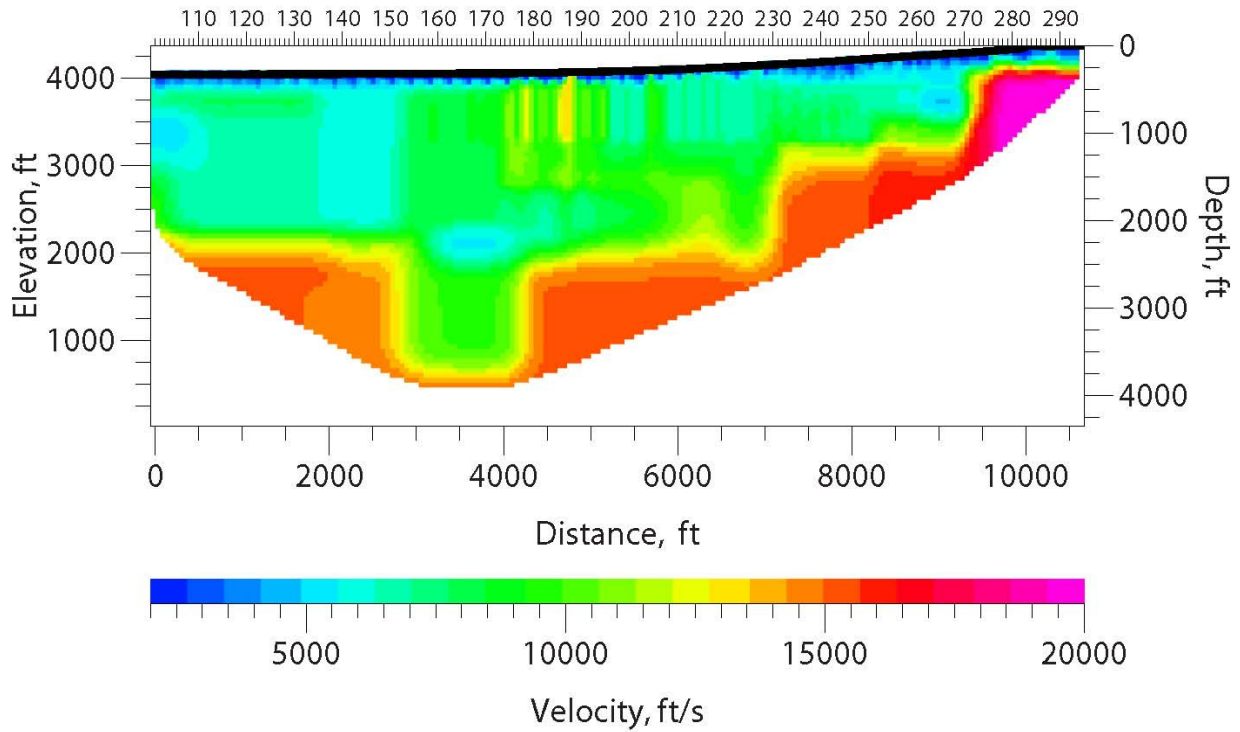


Figure 13d: P-wave velocity model along Line 8 (800) obtained from optimization of P-wave first-arrival travel times.

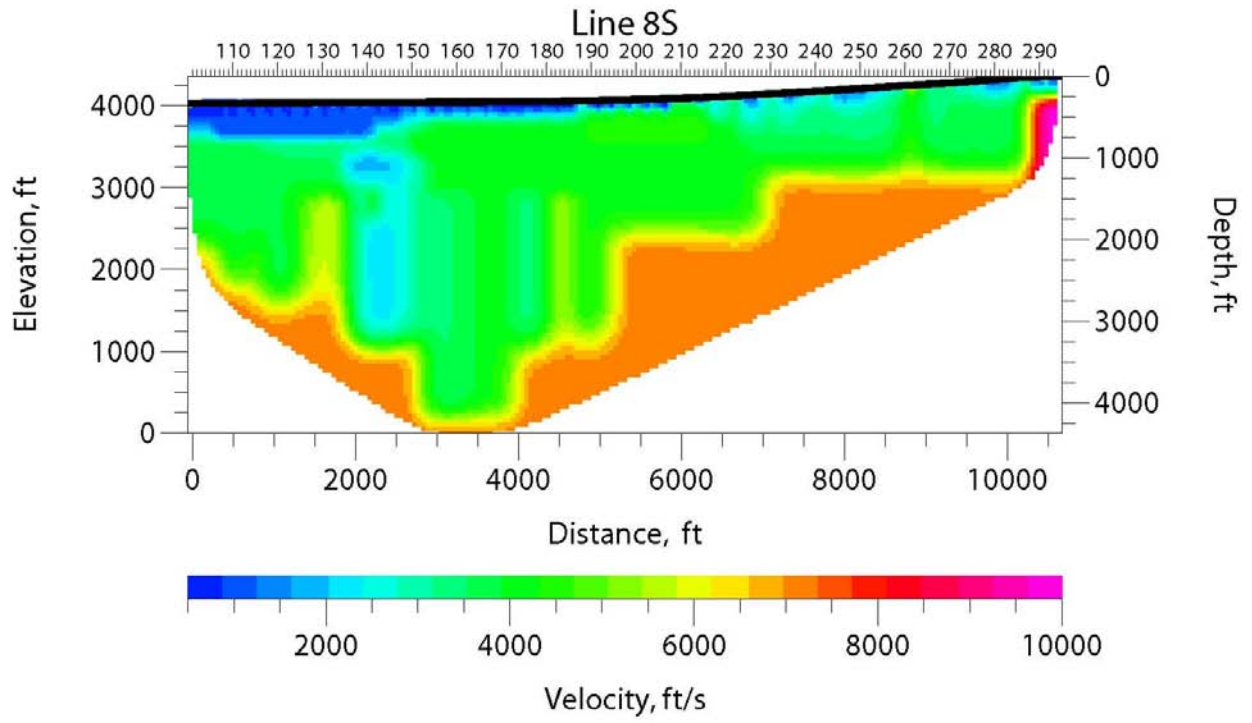


Figure 13e: S-wave velocity model along Line 8 (800) obtained from optimization of SH-wave first-arrival travel times.

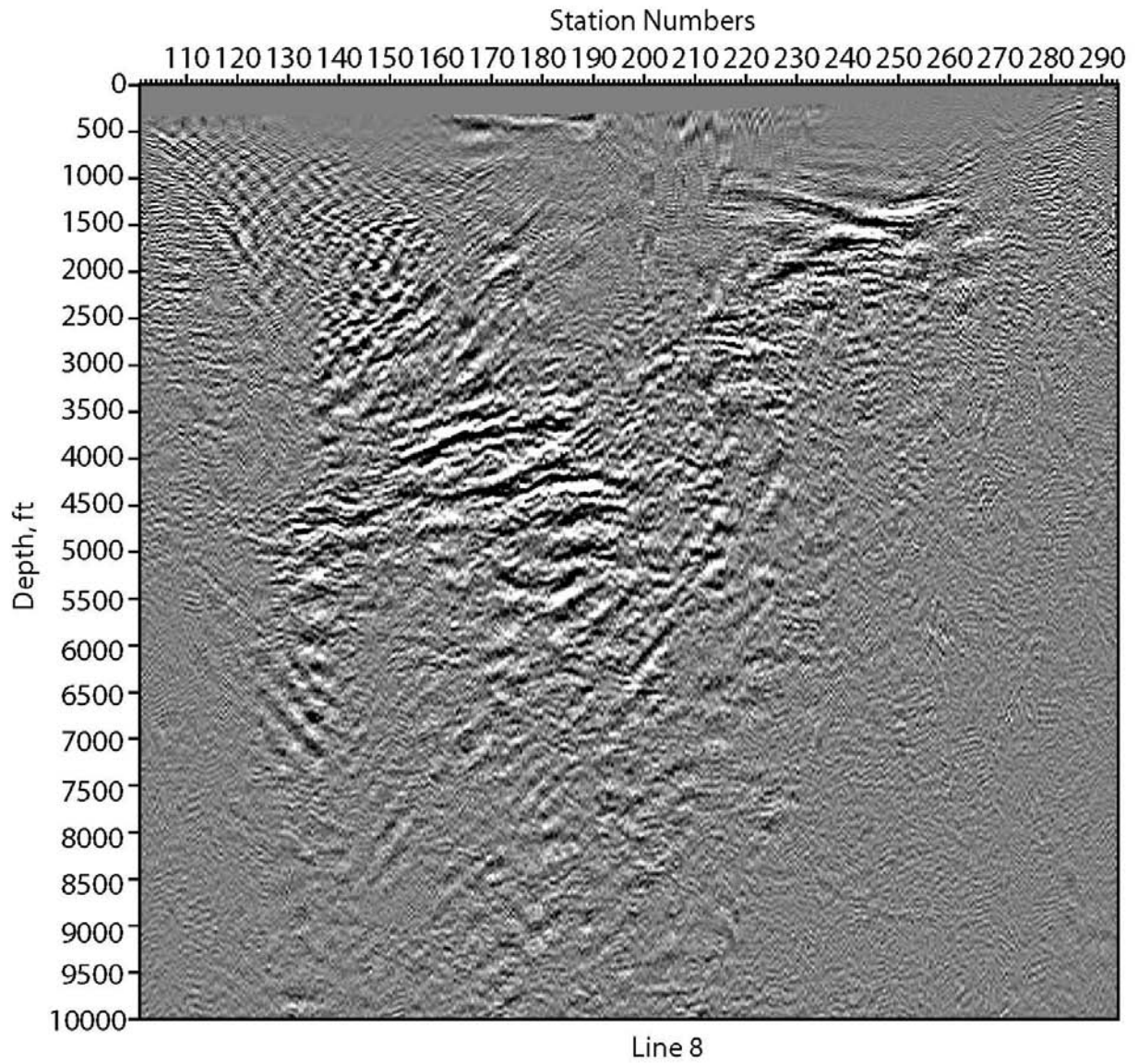


Figure 13f: Depth-migrated image along Line 8 (800) using the velocity model shown in Figure 13g.

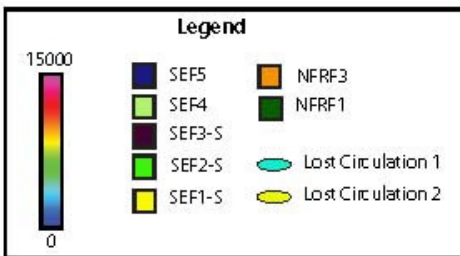
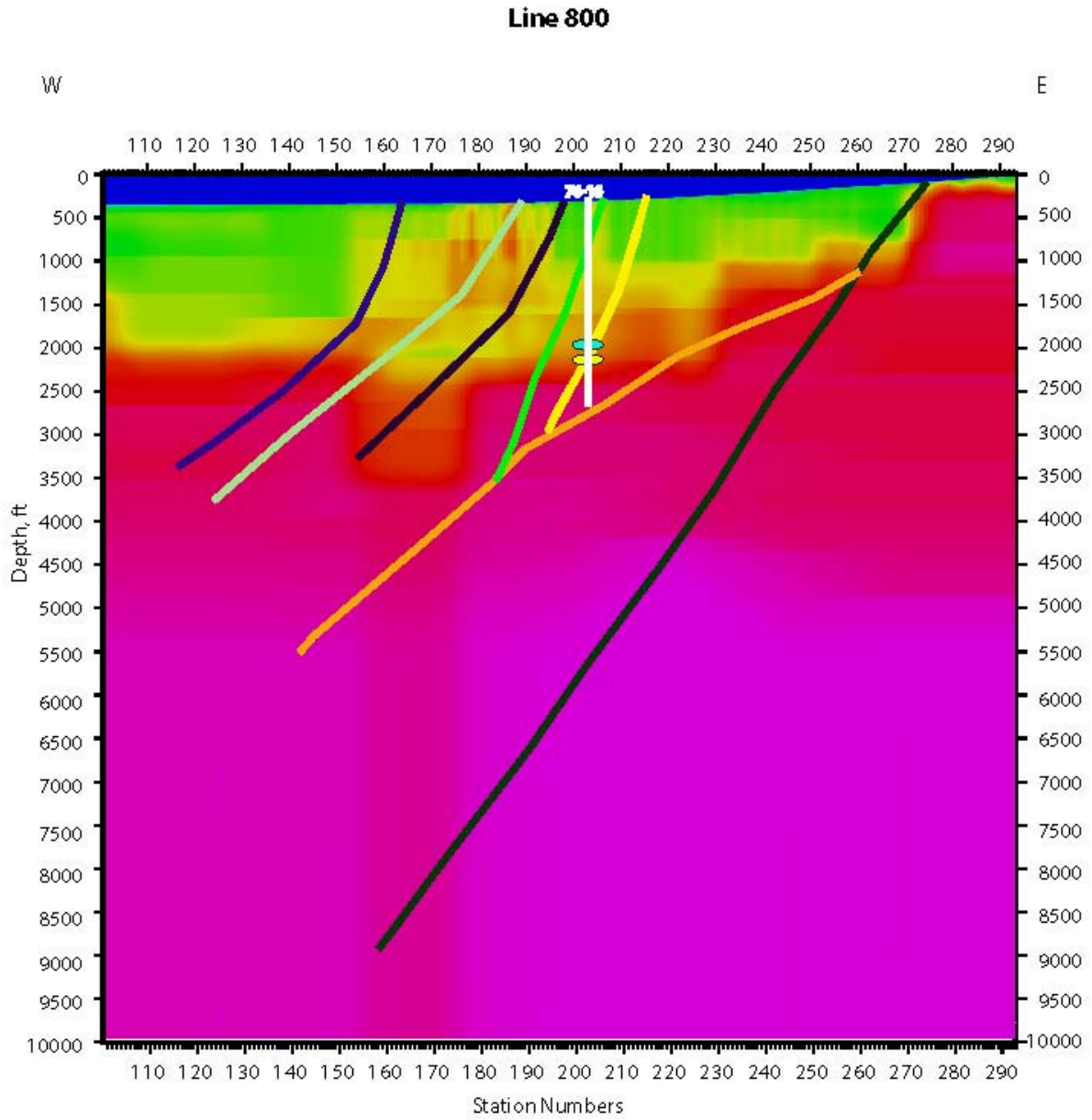


Figure 13g: P-wave velocity model along Line 8 (800) extended in depth. The interpretations were made in conjunction with the shear-wave velocity model (Figure 13h) and the P-wave reflection image (Figure 13i). Velocities go from 0 ft/s (blue) to 15,000 ft/s (purple).

# Line 800

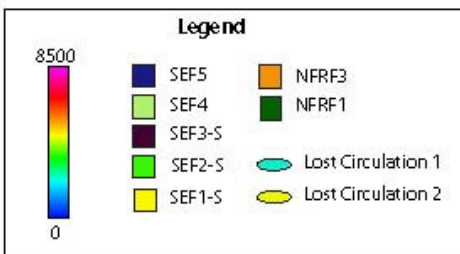
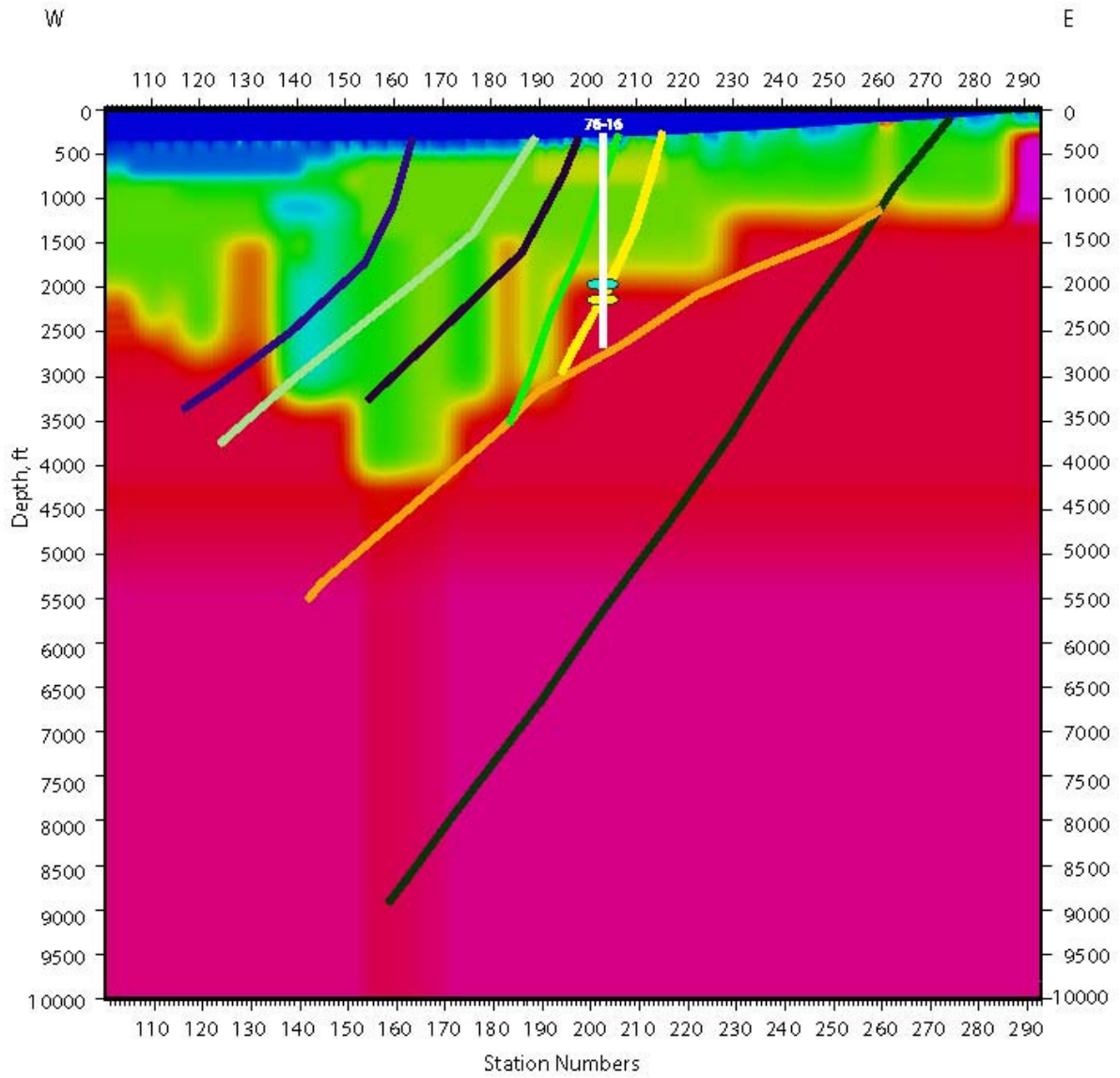


Figure 13h: S-wave velocity model along Line 8 (800) extended in depth showing the faults and discontinuities inferred by the structural team. The interpretations were made in conjunction with the P-wave velocity model (Figure 13g) and the reflection image (Figure 13i). Velocities go from 0 ft/s (blue) to 8,500 ft/s (purple).

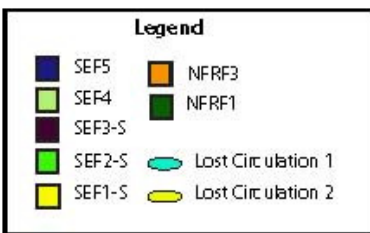
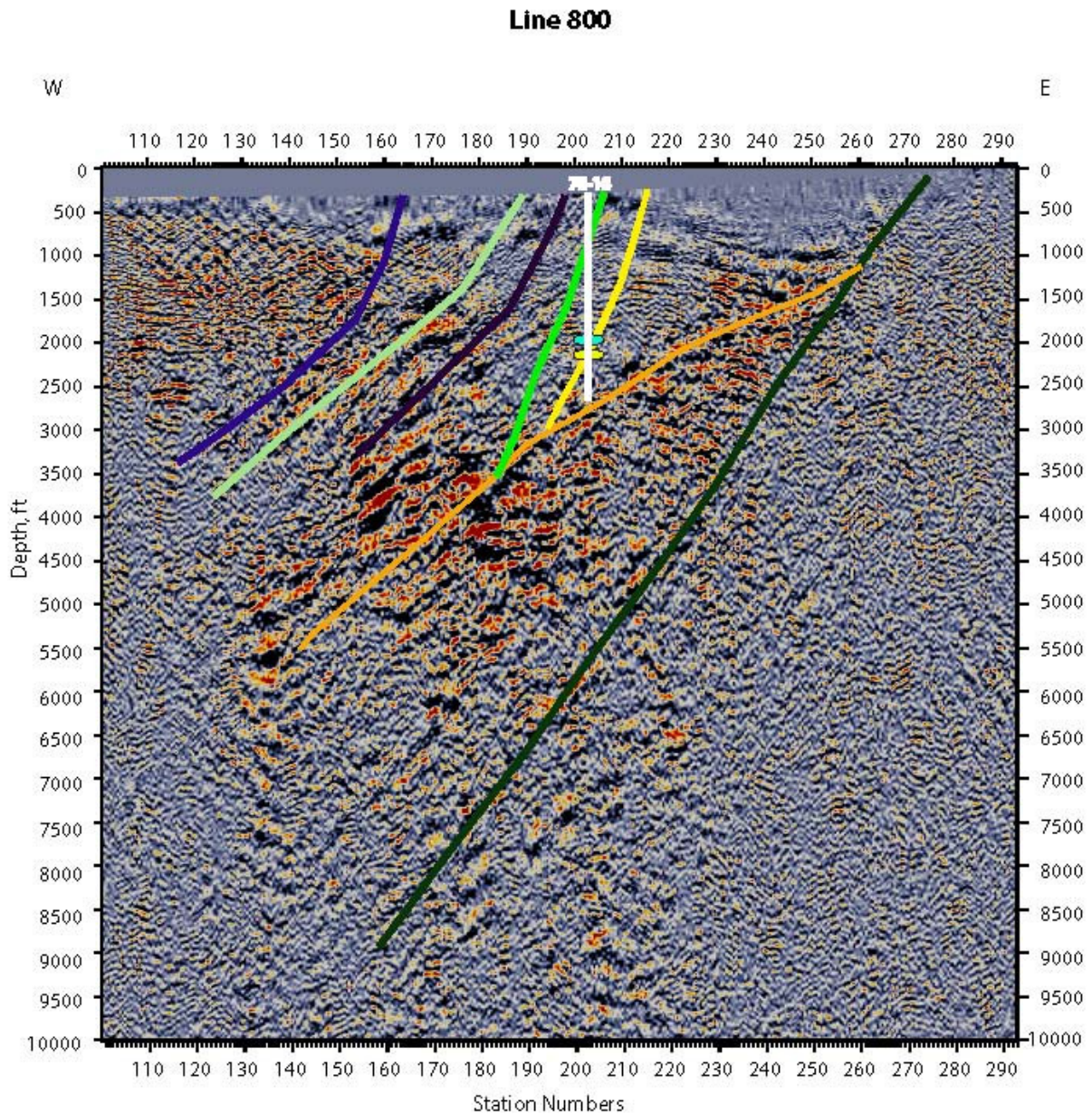


Figure 13i: P-wave depth migrated reflection image along Line 8 (800) showing the faults and discontinuities inferred by the structural team. The interpretations were made in conjunction with the P-wave velocity model (Figure 13g) and the shear-wave image (Figure 13h).

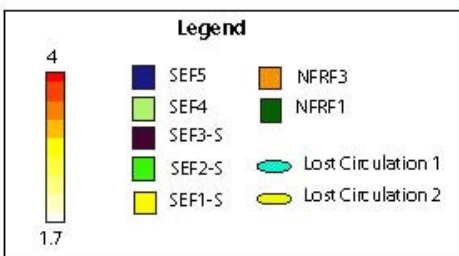
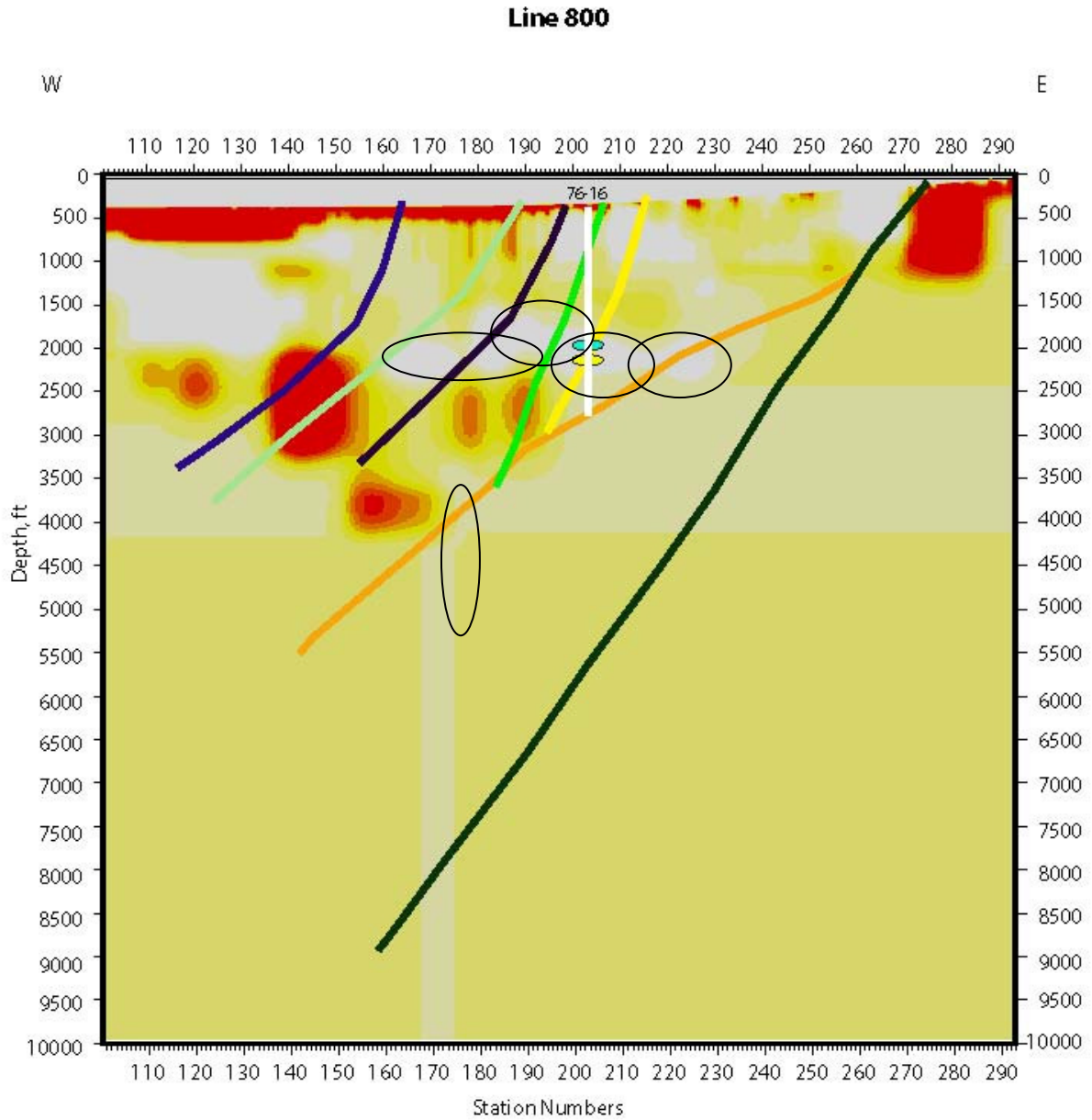


Figure 13j:  $V_p/V_s$  ratio calculated from P-wave and S-wave velocity models along Line 8 (800). The relatively lower  $V_p/V_s$  zones (circles) are potential fractured fluid filled zones.

The low  $V_p/V_s$  zones (Figure 13j) that lie close to fault intersections and traces are marked as areas of potential fractured or fluid filled fracture zones. The lost circulation encountered along 76-16 along the low  $V_p/V_s$  zone and its intersection with fault SEF1-S. Other zones could be intersected along SEF2-S and SEF3-S (Figure 13j). As with other lines, these zones also match very well with the strong lateral velocity variation seen in the velocity model (both P-wave and S-wave) around station 180.

#### 4.10 4.10 Line 9 (900)

Line 9, also called 900, is the in the southern part of the project area and southern most line in this project. It runs east-west from station number 101 in the west to 293 in the east (Figure 14a). All of the figures represent true seismic depth sections with no vertical exaggeration.

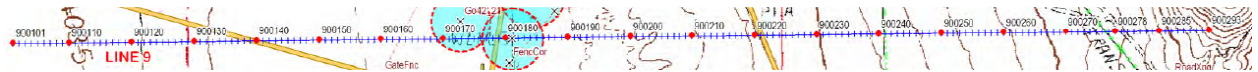


Figure 14a: Line 9 (900) runs east-west from station number 101 in the west to station number 293 in the east.

Figures 14b and 14c show a typical shot gather acquired along Line 9 using P-wave and SH-wave source, respectively. The first arrivals (shown in red) were picked and used to obtain the velocity models shown in Figures 14d and 14e, respectively.

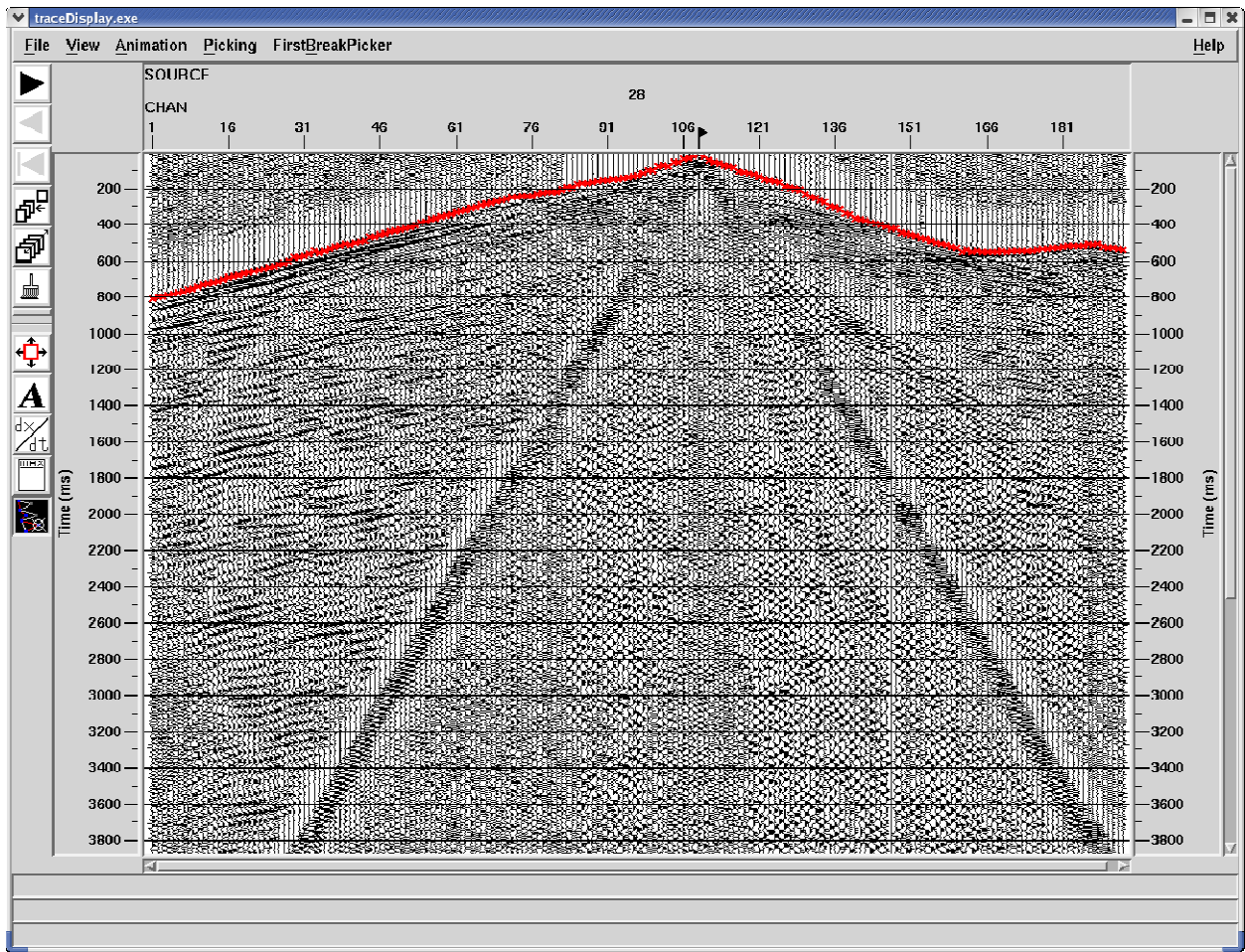


Figure 14b: Typical shot gathers from P-wave data collected along Line 9 (900). The first arrival picks, shown in red, was used to obtain the P-wave velocity model shown in Figure 14d.

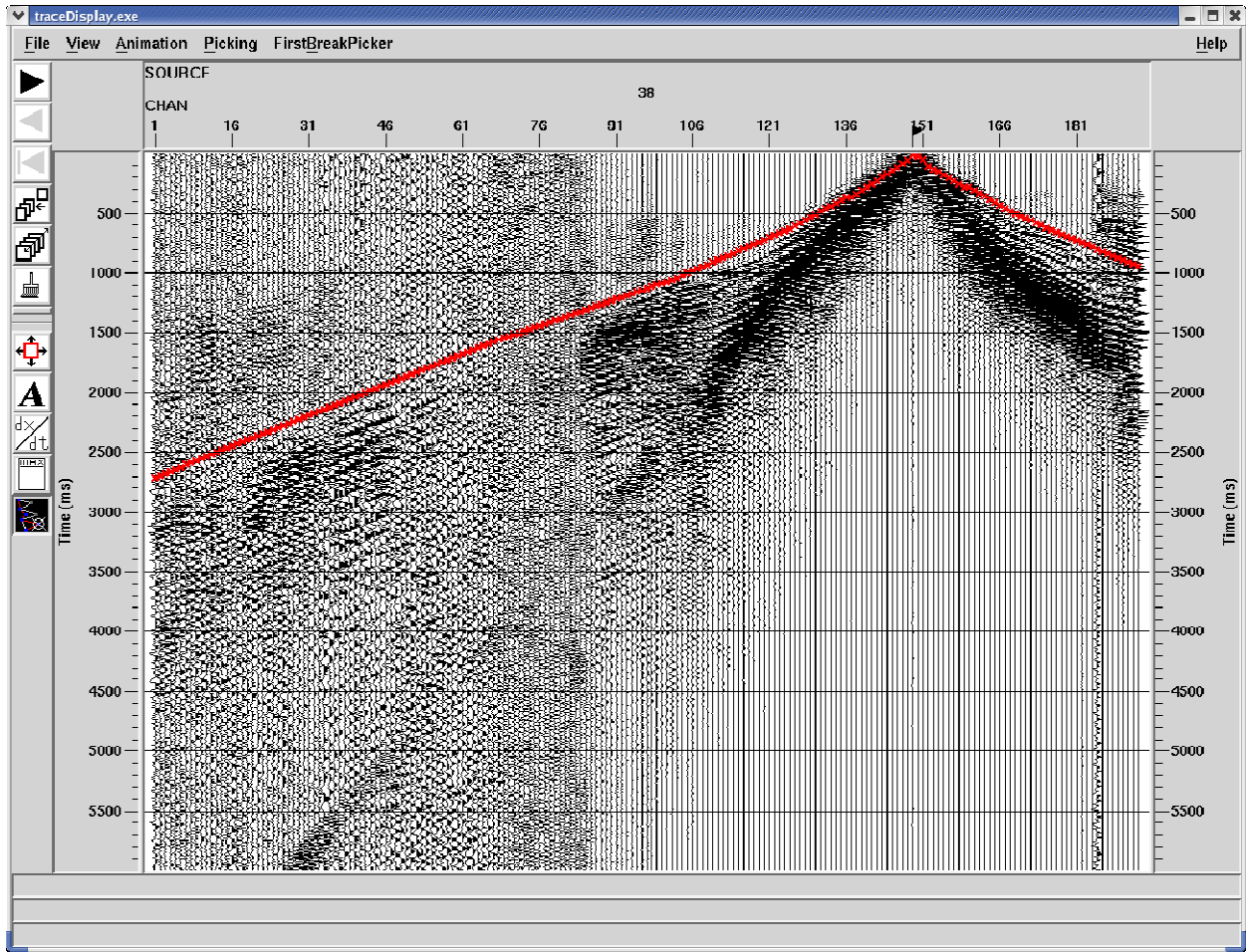


Figure 14c: Typical shot gathers from SH-wave data collected along Line 9 (900). The first arrival picks, shown in red, was used to obtain the S-wave velocity model shown in Figure 14e.

Figures 14d and 14e show the velocity model obtained from optimization of P-wave and SH-wave first arrival data, respectively. P-wave velocities range from 1,500 ft/s to 15,000 ft/s. High velocities in the range of 15,000 ft/s shallow towards the range front in the east. Since the seismic line goes well into the ranges, the higher velocities appear shallower in the east compared to the northern lines. The S-wave velocities range from 500 ft/s to 10,000 ft/s. As with the P-wave velocities, the higher velocities shallow towards the east. There is a lateral change in velocities around station 170.

This model is then extended in depth by interactive velocity modeling. It involved selecting an appropriate gradient that was consistent with the velocities observed along the other lines. Figure 14f shows results of a P-wave depth migration obtained using the P-wave velocity model shown in Figure 14d. Interpretations of the velocity and reflection images are shown in Figures

14g, 14h, and 14i. During the interpretation both the reflection images and the velocity model was used to identify faults and structures. Faults were inferred by direct reflections of them or by truncations of sub-horizontal reflections.

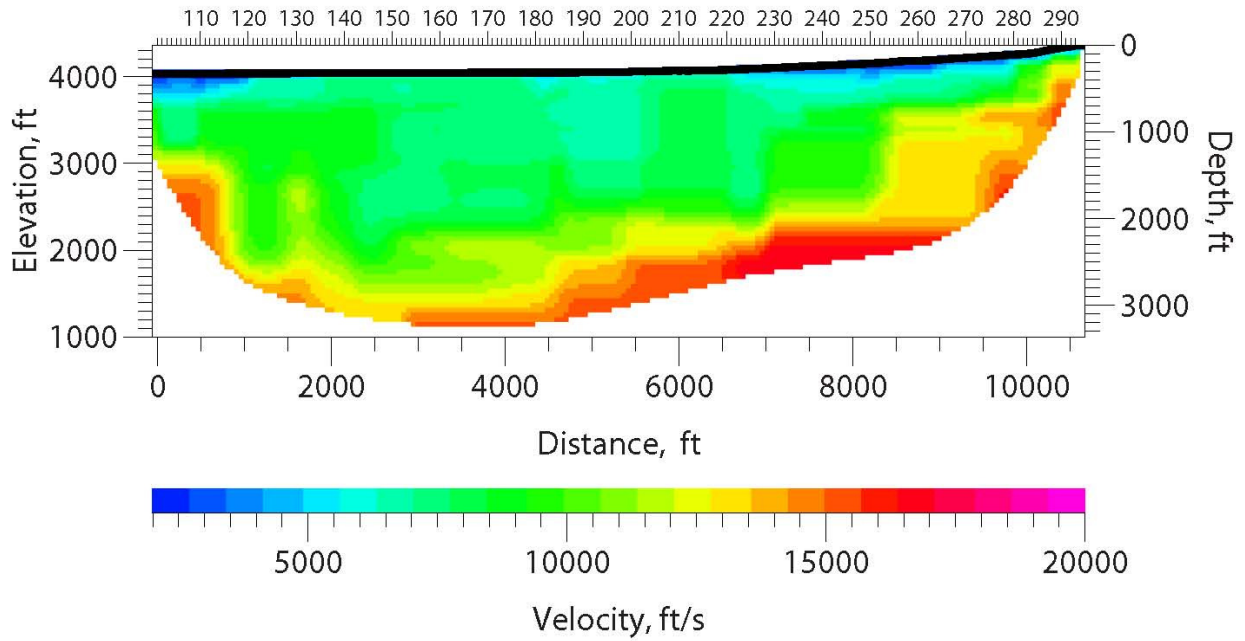


Figure 14d: P-wave velocity model along Line 9 (900) obtained from optimization of P-wave first-arrival travel times.

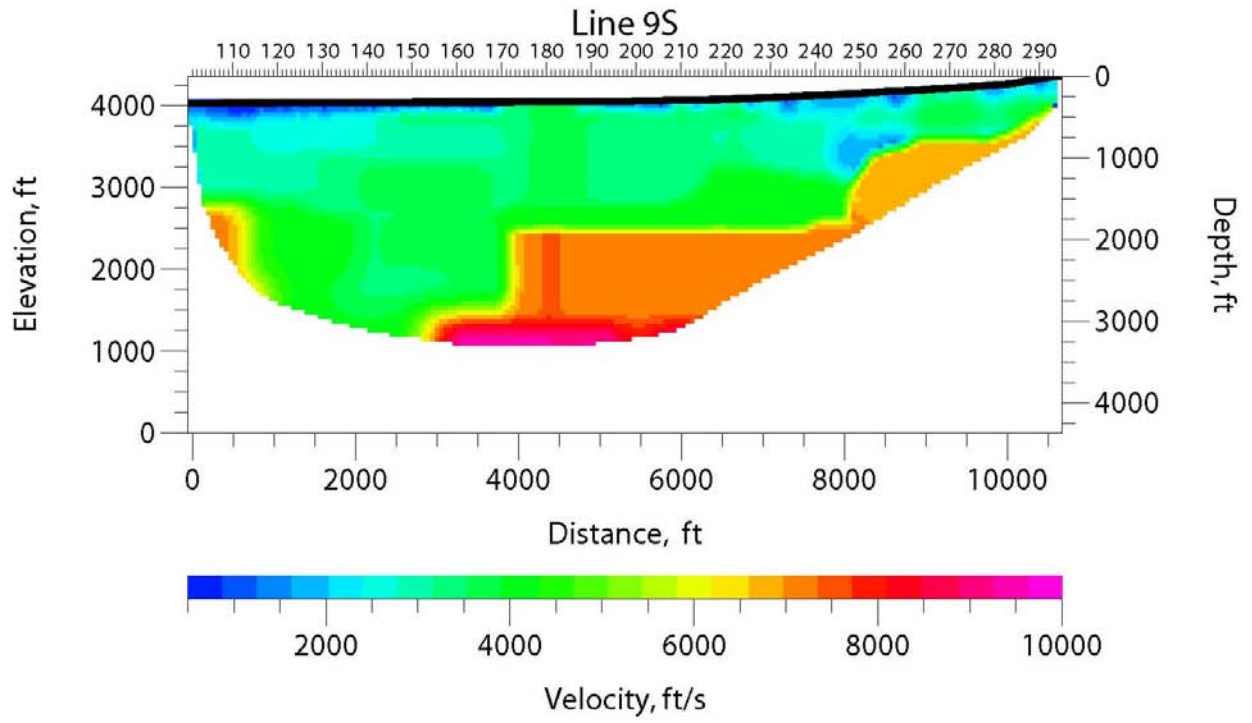


Figure 14e: S-wave velocity model along Line 9 (900) obtained from optimization of SH-wave first-arrival travel times.

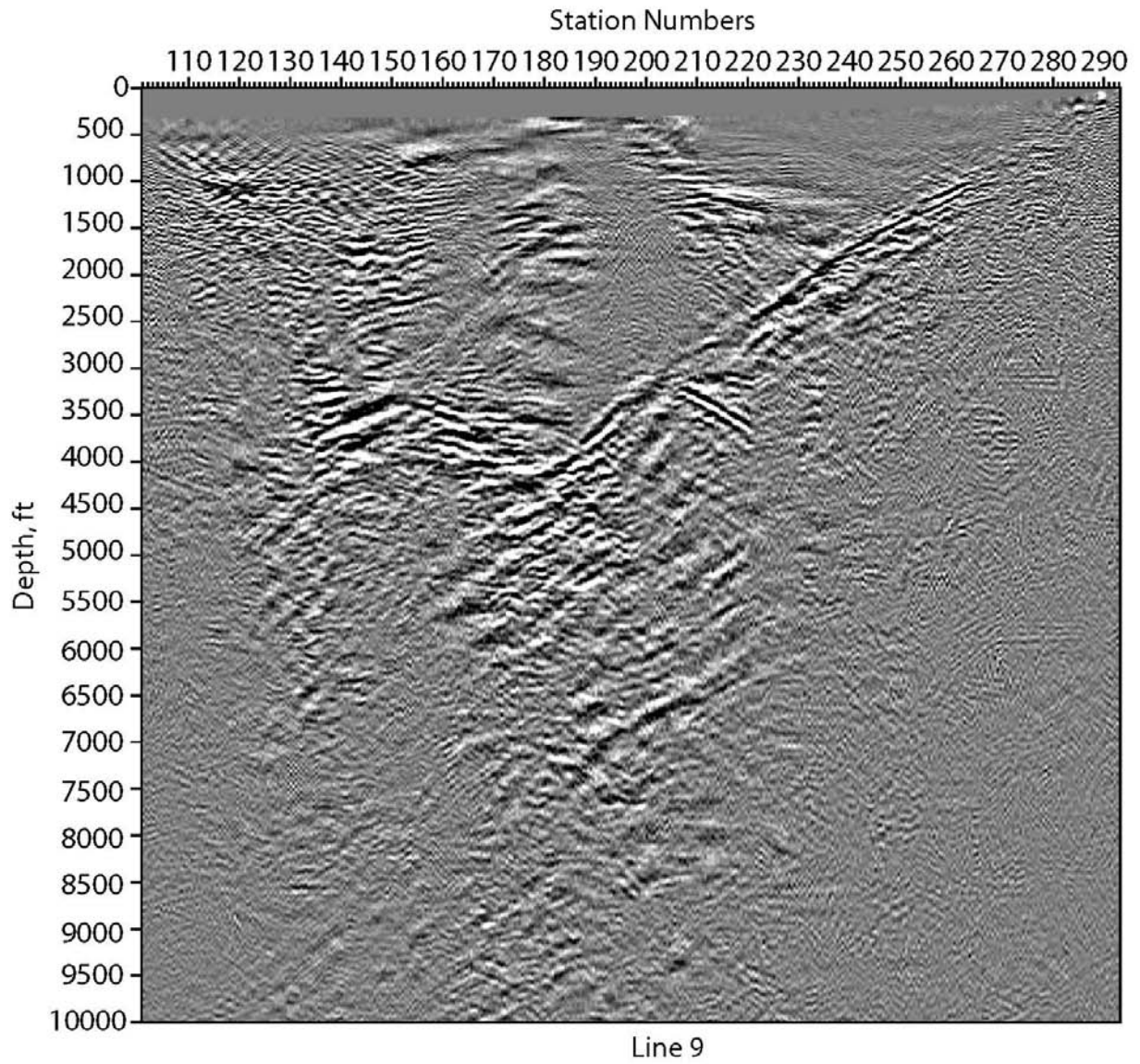


Figure 14f: Depth-migrated image along Line 9 (900) using the velocity model shown in Figure 14g.

### Line 900

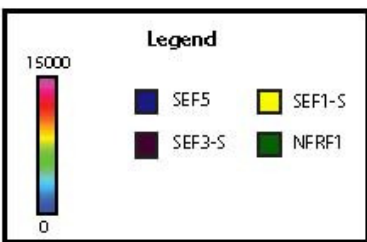
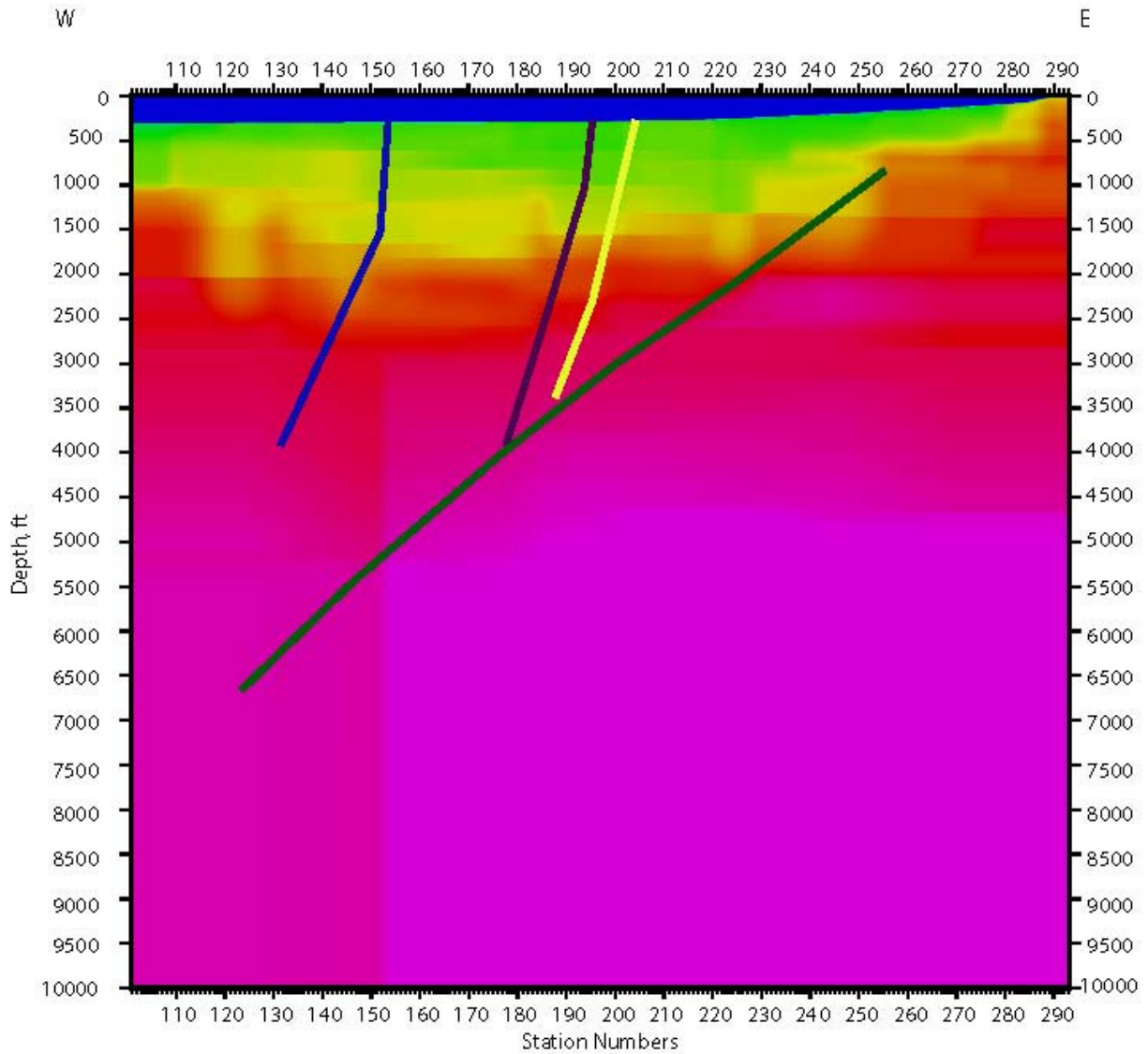


Figure 14g: P-wave velocity model along Line 9 (900) extended in depth. The interpretations were made in conjunction with the shear-wave velocity model (Figure 14h) and the P-wave reflection image (Figure 14i). Velocities go from 0 ft/s (blue) to 15,000 ft/s (purple).

# Line 900

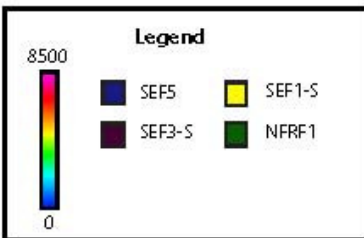
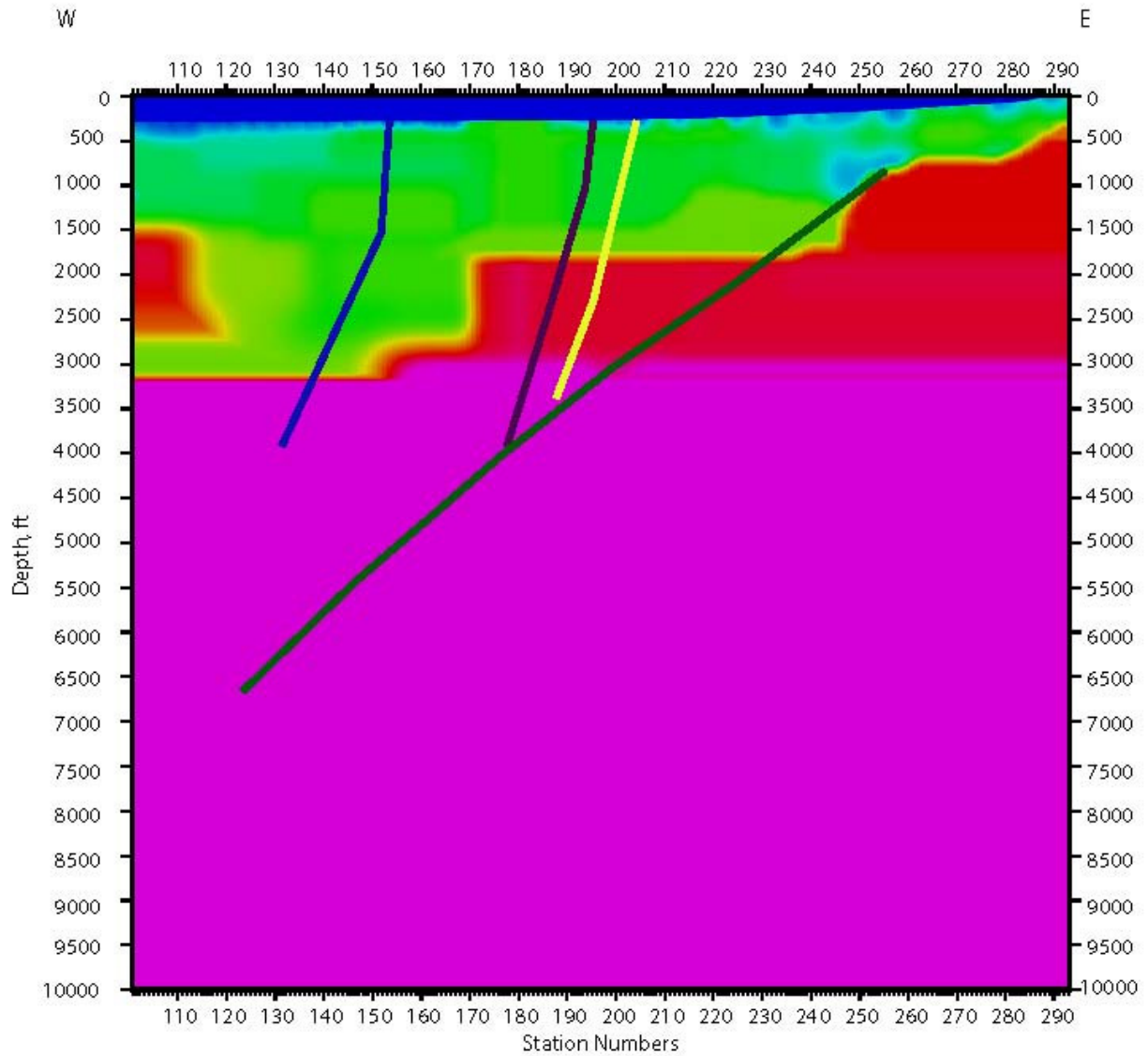


Figure 14h: S-wave velocity model along Line 9 (900) extended in depth showing the faults and discontinuities inferred by the structural team. The interpretations were made in conjunction with the P-wave velocity model (Figure 14g) and the reflection image (Figure 14i). Velocities go from 0 ft/s (blue) to 8,500 ft/s (purple).

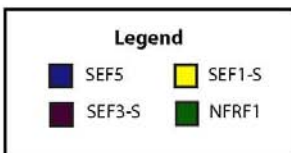
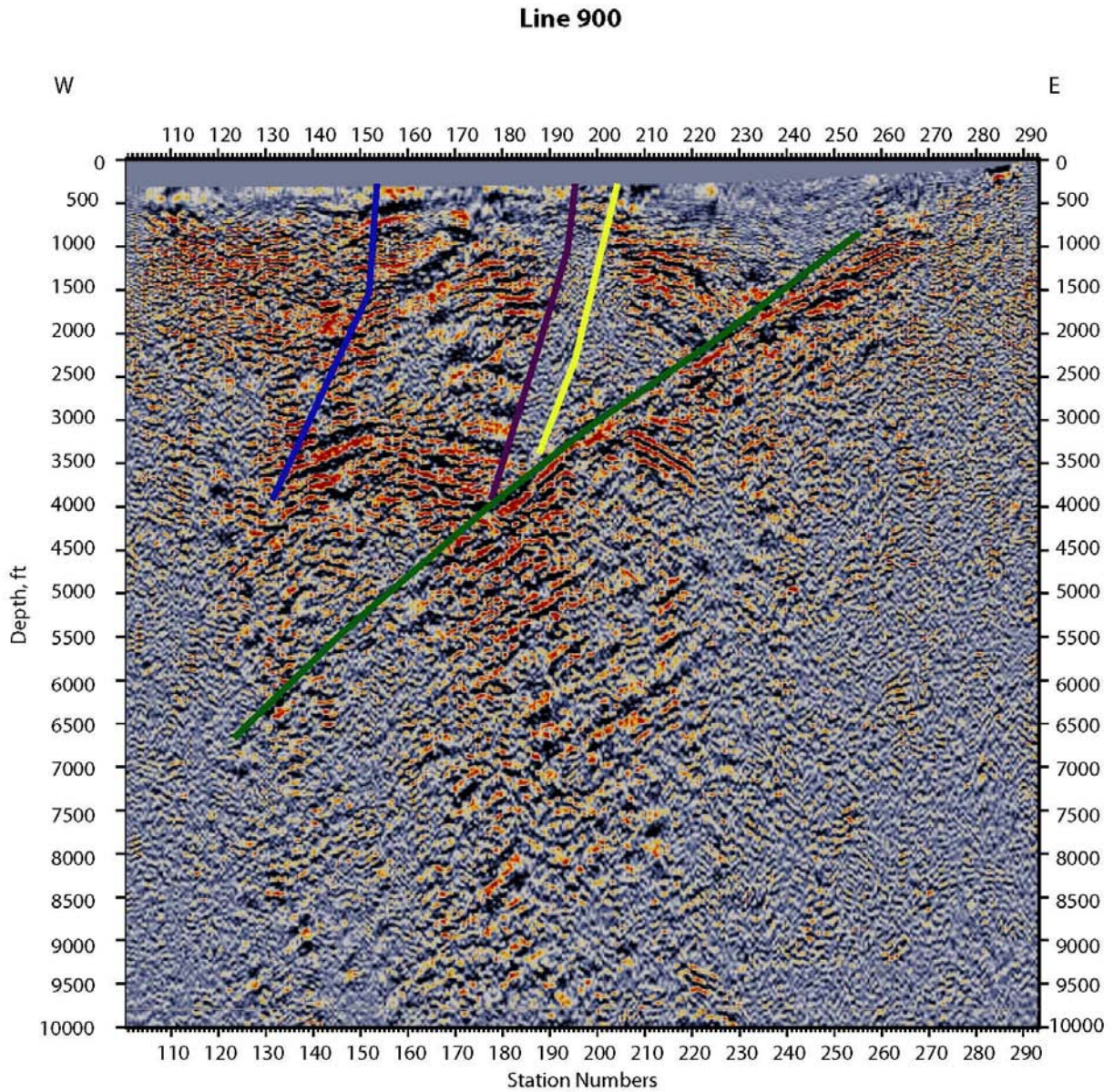


Figure 14i: P-wave depth migrated reflection image along Line 9 (900) showing the faults and discontinuities inferred by the structural team. The interpretations were made in conjunction with the P-wave velocity model (Figure 14g) and the shear-wave image (Figure 14h).

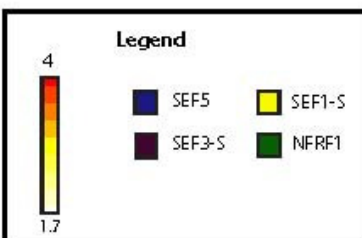
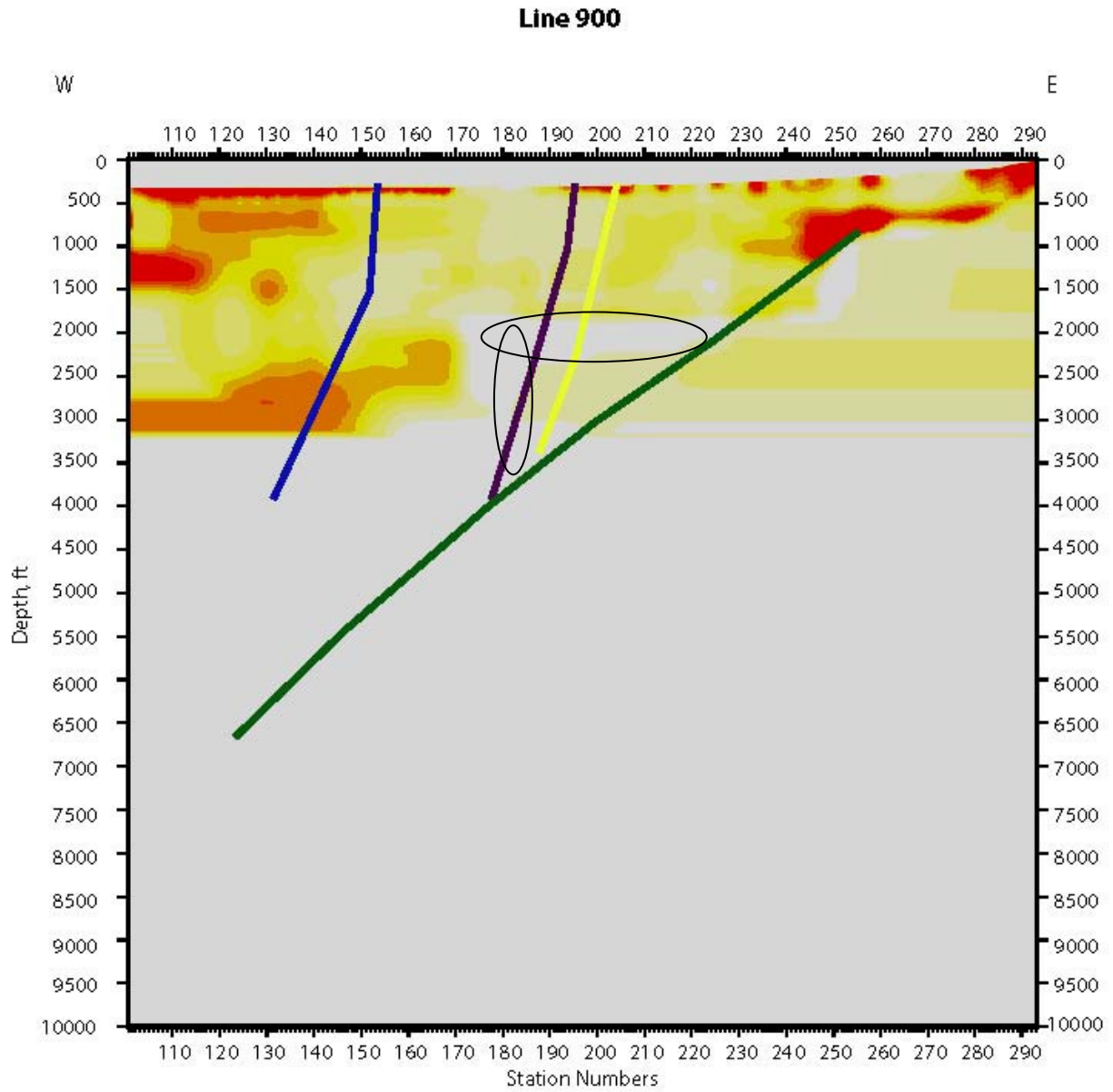


Figure 14j:  $V_p/V_s$  ratio calculated from P-wave and S-wave velocity models along Line 9 (900). The relatively lower  $V_p/V_s$  zones (circles) are potential fractured fluid filled zones.

The low  $V_p/V_s$  zones (Figure 14j) that lie close to fault intersections and traces are marked as areas of potential fractured or fluid filled fracture zones. Low  $V_p/V_s$  zones are found down dip of SEF1-S and SEF3-S (Figure 14j). As with other lines, these zones also match very well with the strong lateral velocity variation seen in the velocity model (both P-wave and S-wave) around station 170.

## 5 5.0 Preliminary Interpretations and Conclusions

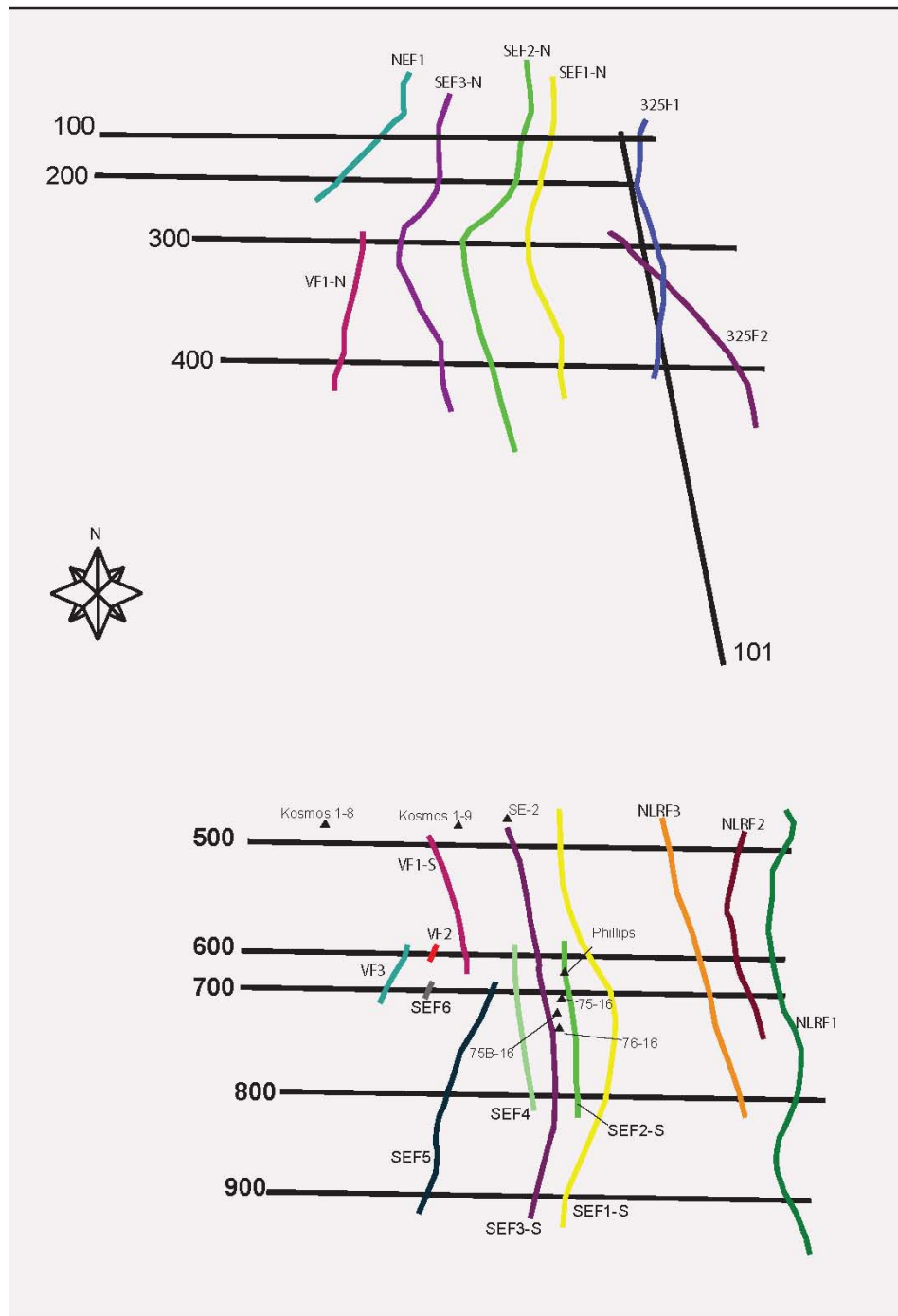


Figure 15: Map showing surface trace of faults imaged and inferred from the seismic profiles and their relationship to the existing wells.

Figure 15 shows surface trace of faults mapped from the seismic data and their relationship to existing wells. Figure 16 shows the same map superimposed on a Google Earth image.

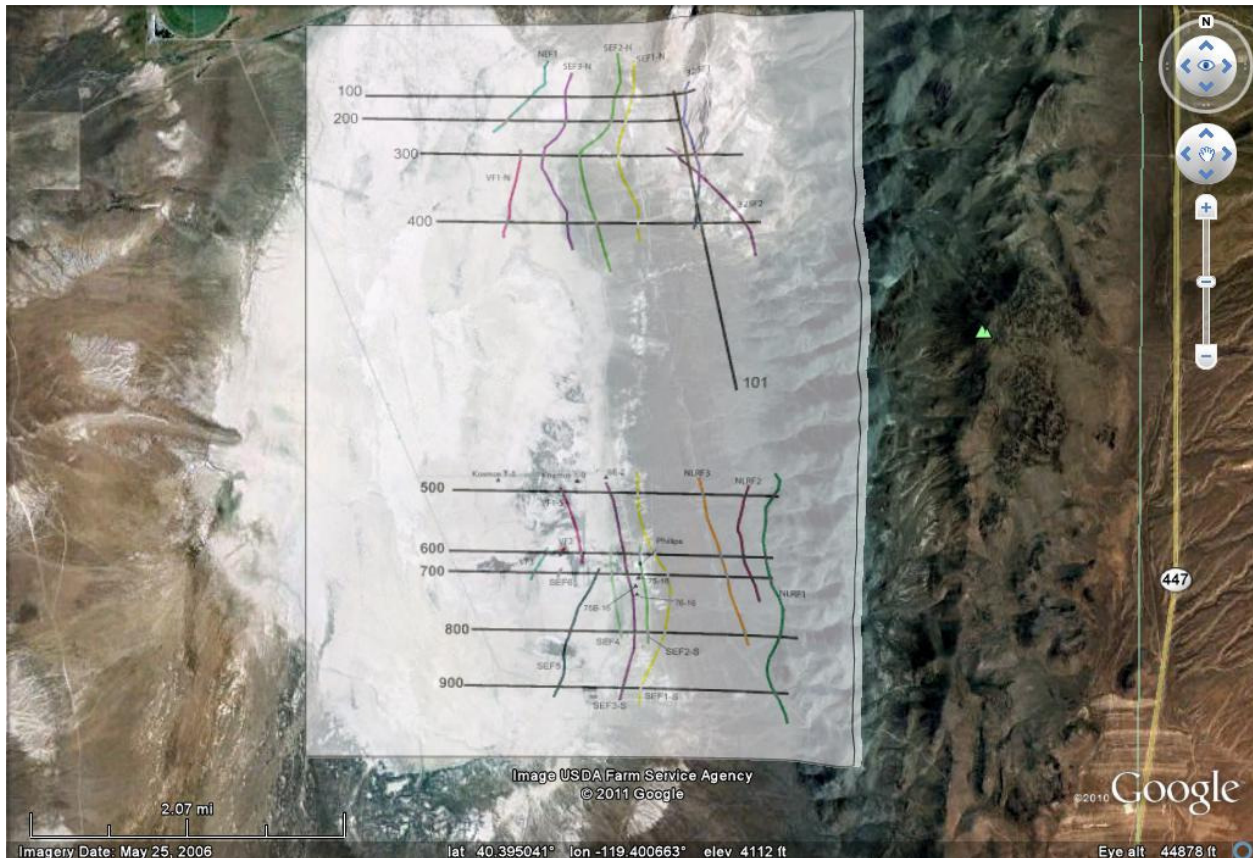


Figure 16: Surface fault trace superimposed on a Google Earth image. The Range Front faults and several west dipping faults are imaged.

Several common features are inferred from analyzing the seismic profiles, both in the northern and southern sections.

- The range front fault is imaged both as a reflector and as a P-wave and S-wave velocity contrast.
- Several west dipping faults are imaged across the entire geothermal prospect.
- Faults are either imaged directly or inferred from lateral velocity variations and truncations of flat lying layers.
- Lost circulation zones encountered in existing production and injection wells in the southern part of the geothermal prospect match very well with regions where there is a lateral velocity change within the high velocity basement (2,000 – 3,000 feet depth), both in the P-wave and S-wave velocity model.
- Low  $V_p/V_s$  ratio also seem to be an indicator of fractured and lost circulation zones. It is expected that there will be a decrease in  $V_p/V_s$  ratios within the fluid filled fracture zones (Bonner et al., 2006). The P-wave velocities will decrease with the opening of cracks and presence of fluids, while the S-waves being insensitive to presence of fluids may not show any decrease resulting in an overall decrease in the  $V_p/V_s$  ratios.

- Lost circulation zones are also associated with faults. In particular, the interaction between a fault, low Vp/Vs zones, and zones of sharp lateral velocity changes within high velocity basement seem to be a good indicator of possible fluid filled permeable zones. In the southern section of the prospect, faults labeled SEF2-S and SEF3-S seem to be conduits for fluids (Figures 15 and 16). It is imported to note the well SE-2 which did not encounter any permeable zones projects on footwall side of the SEF2-S fault.
- Observations made above could be used to locate additional wells in the southern region and also in the unexplored northern region of the San Emidio geothermal prospect.

## 6 6.0 References

Bonner, B., Hutchnigs, L., Kasameyer, P., 2006, A Strategy for Interpretation of Microearthquake Tomography Results in the Salton Sea Geothermal Field Based upon Rock Physics Interpretation of State 2-14 Borehole Logs, presented at the Geothermal Research Council Annual Meeting, San Diego, September 2006.

Louie, J.N., and Qin, J., 1991, Subsurface imaging of the Garlock fault, Cantil Valley, California: *Journal of Geophysical Research*, B., Solid Earth and Planets, v. 96, p. 14,461-14,479.

Pullammanappallil, S.K., and Louie, J.N., 1994, A generalized simulated-annealing optimization for inversion of first arrival times: *Bulletin of the Seismological Society of America*, v. 84, p. 1397-1409.

Pullammanappallil, S. K., and J. N. Louie, 1997, A combined first-arrival travel time and reflection coherency optimization approach to velocity estimation: *Geophys. Res. Lett.*, 24, 511-514.

Pullammanappallil, Satish, William Honjas, Jeffrey Unruh, and Francis Monastero, 2001, Use of advanced data processing techniques in the imaging of the Coso geothermal field: *Proceedings, Twenty-Sixth Workshop on Geothermal Reservoir Engineering*, Stanford University, Stanford, California, January 29-31, SGP-TR-168, 8 pp.

Unruh, J. R., Pullammanappallil, S. K., and Honjas W., 2001, New seismic imaging of the Coso geothermal field, eastern California: *Proceedings of the 26<sup>th</sup> workshop on Geothermal Reservoir Engineering*, Stanford University, CA, January 29-31.